Cathode Materials Produced by Spray Flame Synthesis for Lithium Ion Batteries

Von Der Fakultät für Ingenieurwissenschaften, Abteilung Maschinenbau und Verfahrenstechnik der
Universität Duisburg-Essen
zur Erlangung des akademischen Grades

DOKTOR-INGENIEUR

genehmigte Dissertation

von

NoorAshrina Binti A. Hamid
aus
Kedah, Malaysia

1. Gutachter: Prof. Dr. rer. nat. Christof Schulz
2. Gutachter: Prof. Dr. rer. nat. Angelika Heinzel

Tag der mündlichen Prüfung: 03.07.2013

Dedicated to Mohd Fadzly, Aminabee and Nur Aleesya Sofea,

for their true inspiration and endless pray

Acknowledgement

My journey in Germany would not have been possible without strong support from Dr. Hartmut Wiggers and Prof. Christof Schulz since the first time I arrived here for so called interview in three weeks during March 2009. Both deserve the huge gratitude from the bottom of my heart for allowing me to be as part of IVG member specifically to pursue my doctoral study. Warmest gratitude to Prof. Dr, Christof Schulz for believing in me and really help me with a lot of documentation before and after I came to Deutschland. Thank you very much especially to Dr. Hartmut Wiggers for teaching me a lot of things that I didn't really understand and for his guidance and countless discussions. Hartmut, I will try to be as calm as you especially during presentation and try to talk slowly and precisely.

Thank you very much to Sebastian Wennig for performing electrochemical measurement for numerous samples and being such a very nice partner to me. To Sebastian Hardt who developed the flame reactor and allowing me to use it freely. You had helped me much with the reactor and also continuously taught me German language by talking only Deutsch with me. Beate Endres, whom like my sister always, is there for me whenever I run the reactor especially when I'm still new and I treasured the time we had together while waiting to change the syringe during synthesizing the particles. You had helped me not only with technical things but also with informal things. Next person who did lend a hand especially for setting up my furnace is Hans Orthner, thank you very much for your kindness. My deepest appreciation goes to admin person, Barbara Nota and Barbara Graf for helping with admin things during those past years. Also to Iris Steiner for her great help during my visa application as well as huge effort during the first three months by lending hand buying things for my new flat.

I would highly appreciate the countless characterization works done by Helge Grimm for TEM, Felix Becker and Ulrich Hagemann for XPS measurements, Günther Prinz for Raman spectroscopy, Dr. Aslam Siddiqi for TG measurement, Adrian Münzer for SEM, Joachim Landers for Mossbauer Spectroscopy measurement and last but not least Markus Engenhorst for electrical conductivity measurement. Also, for Dr. Udo Doeffler whom taught me how to run the XRD and always change the monochromator for me. To all of you, again thank you so much for your great help and kindness.

My friends who always made me feel at ‘home’ especially Sonja Hartner, you are the most generous person I ever met since the first time I met her at Duisburg Hauptbahnhof in March 2009, had ‘urged’ her father to do some ‘shopping’ with me for my new flat, for that I truly indebt with you Sonja. I am also indebt with Nils Petermann, Ingo Plümel, Sebastian Hardt for helping me when I bought the sofa and cupboard from Immobilien. Thank you very much you guys. Nils Petermann, my 'neighbor' whom really hardworking and I am pleased to stay next to you because indirectly I became hardworking. Helge Grimm, a friend who always made me smile and helped me with the computer stuffs while donating a lots of choclate, particularly. I would like to express my warm gratitude for all my friends, Malin, Anoop, Robert, Sebastian Kluge, Jasmina, Natascha, Ali, Khadijeh, Ingo, Aldi, Ludger and Oliver for the nice time we had during past years. And the rest of IVG team member, thank you for being such a wonderful team to be with.

My doctoral study wouldn’t have been realized without strong persuade from my beloved mother. She is my inspiration. I present my doctoral degree for you, mak. Not to forget my beloved father, brothers and sisters for their love and passionate encouragement throughout the days. I am grateful to my parent and brothers in law for allowing their son/brother to accompany me for 3 and half years here in Germany.

The backbone of my decision and the person who never stop trust in me and always provide with countless advises either professionally or casually, my beloved husband, Mohd Fadzly Samsudin, you are my hero, to you I present my success and thank you for all your sacrifice and patience for all these passing years. My adorable daughter, Nur Aleesya Sofea for being such a wonderful treasure in my life and for relish my time whenever I was sick of my work.

Huge gratitude goes for the University Science of Malaysia and Ministry of Higher Education Malaysia for granted me full scholarship for my Ph.D study here.

NoorAshrina A Hamid

Duisburg

1 Jan 2013

List of Abbreviations and Symbols

Abbreviations

AC	Alternating current
BET	Brunauer-Emmet-Teller
CV	Cyclic voltammogram
EV	Electric vehicle
FWHM	Full-width at half maximum
HEV	Hybrid electrical vehicle
SEM	Scanning electron microscopy
SSA	Spesific surface area
TEM	Transmission electron microscopy
TGA	Thermal gravimettry analysis
Wh	Watt hour
Wh kg^{-1}	Watt hour per kilogram
W kg^{-1}	Watt per kilogram
XRD	X-Ray diffraction
XPS	X-Ray photoelectron spectroscopy

Symbols

d_{BET}	Particle size calculated from BET
d_{XRD}	Crystal size calculated from XRD
ρ	Density
λ	X-Ray wavelength
K	Dimensionless shape factor (with typical value of 0.9)
β	Full width at half maximum (FWHM) in radian(in 2θ)
θ	Bragg angle
E_K	Kinetic energy
E_B	Binding energy
h	Planck constant
ν	Frequency
Φ	Energy required for the electrons to escaped from the atom's surface
σ_b	Bulk conductivity
t	Distance between two inner electrodes
R_b	Bulk resistance
A	Area of the sample
R	Resistance
V	Voltage
I	Current

Table of contents

1 Motivation

Every living thing, including humans, needs energy to live. We need energy mainly for heating and cooling homes, powering appliances and home electronics, moving vehicles, and production of food and other goods. The common energy source, which has taken billions of years to form, is oil and coal. It is consumed worldwide and causes serious environmental damage such as rising greenhouse gas concentrations that lead to global climate change. Better understanding coupled with research and development of creating more environmentally benign energy sources are needed in order to develop a sustainable energy system for the next generations.

Thus, energy produced by renewable sources for instance solar, wind and others will be favored in future. Because it is not continuously available it must be combined with efficient storage systems in such a way that it can be transferred to or used for the end consumer's products at the time needed. It is mandatory to have efficient energy storage systems that can be conveniently charged and discharged with electrical energy such as pumped storage hydro power stations, compressed air energy storage, and hydrogen storage. Electrochemical energy storage systems such as batteries, capacitors and supercapacitors are widely used in electronic based appliances and most recently in electric vehicles [1, 2]. Each of these storage systems has its own advantages and disadvantages and they differ in capacity, storage density and peak power. Batteries and fuel cells are similar in the sense that both convert electrical and chemical energy and consist of two electrodes, an electrolyte and a separator, whereas capacitors store electrical energy as surface charges[1]. Analogous to battery and fuel cell systems, supercapacitors are composed of two electrodes, separator and electrolyte, and are able to produce higher power density as compared to the previous systems. Supercapacitors are known to withstand charge and discharge at high current within minutes of time whilst it takes several minutes to half an hour for batteries (especially Li-ion batteries) to charge. Though supercapacitors are able to provide high power density (~10,000 W kg^{-1}) in comparison to batteries (1,000–3,000 W kg^{-1}), batteries and in particular Lithium-ion batteries have claimed most of the electronic consumer market as they are able to provide a high energy density and higher working voltage compared to supercapacitors. Further development must be taken into account for batteries to meet the criteria of both, high

power and high energy density. Fabricating electrode materials with better performance is crucial for both, anode and cathode.

In this thesis, work on fabrication of cathode material is conducted with the aim to improve the readily available materials used in commercial Li-ion batteries. Among conventional cathode materials, $LiFePO_4$ has won researchers' attention due to its advantages of high intrinsic safety, low costs and being environmentally friendly. So far, however, $LiFePO_4$ suffers from low intrinsic electronic and ionic conductivity that lead to poor performance rates. A known method to overcome these problems is to apply nanosized $LiFePO_4$ that is coated with conductive carbon. Additionally, doping with metal ions helps to increase the conductivity of $LiFePO_4$. Moreover, doping/substitution of iron with elements of higher redox potential such as manganese or vanadium may increase the energy density. Thus, the motivation of this study is to produce high performance cathode materials for Li-ion batteries based on nanosized and highly conductive materials using that are generated in a combination of spray-flame synthesis of nanoparticles and subsequent solid-state reactions. Spray-flame synthesis of nanoparticles is used to produce $FePO_4$ and also $FePO_4$ doped with manganese ($Fe_{(1-x)}Mn_xPO_4$). It offers advantages compared to other methods such as wet-phase synthesis including the capability to produce nanosized $FePO_4$ and $Fe_{(1-x)}Mn_xPO_4$, which will be further processed with a Lithium source and glucose to yield nanocomposite $LiFePO_4$/C and $LiFe_{(1-x)}Mn_xPO_4$/C. Using the gas phase technique, nanosized $FePO_4$ is expected to be simply available in large amounts and can be further processed via solid-state reactions to produce $LiFePO_4$/C nanocomposites. Doping with metal ion is also known to enhance the electrochemical properties of $LiFePO_4$.

This thesis is divided into the following sections:

- Background and basic principles of lithium ion batteries and common cathode materials are briefly explained in the first part (Chapter 2). More particular detail into why $LiFePO_4$ is a good choice of lithium-ion battery electrode material is provided via clarification of its structure and electrochemical properties. Various synthesis routes for producing $LiFePO_4$ are presented.
- General aspects of the gas-phase synthesis of nanoparticles along with solid-state reactions are given in Chapter 3. Also, important analytical methods that are

needed for understanding of the materials synthesized are presented in this chapter.

- The focal point of this study is reported and explained in detail within Chapter 4. A comprehensive study on synthesis and physical, chemical and electrochemical characterization of the bare and doped $LiFePO_4$ are presented and discussed. The electrochemical performance of bare and doped $LiFePO_4$ is compared and discussed.
- Some general conclusions and suggested future recommendation for studies concerning $LiFePO_4$ are presented in Chapter 5.

2 Introduction

Batteries are attractive systems for storing electrical energy. They are located almost everywhere, have no maintenance cost and are readily scalable. Since the first invention of batteries by Alessandro Volta in 1800, the self-contained system which converts chemical energy into electrical energy via a redox reaction, has gone through various enhancements and developments until today. Being classified according to their principle of operation and usage, batteries are mainly categorized as primary (non-rechargeable) and secondary (rechargeable) batteries. Primary batteries normally discharge once and are discarded afterwards due to limitations of their chemical composition. Secondary batteries are able to discharge and recharge back to their original condition by applying a current through the cell [3]. Despite the fact that primary batteries can only be used once, this type is light in weight and easy to dispose of, as it contains no or insignificant amounts of toxic substances [3]. Their high internal resistance, however, makes these batteries unsuitable for use in high power appliances such as notebooks, digital cameras, etc. Thus, secondary batteries are more appealing to be used widely in portable and electronic devices as well as in new era of electric car. In addition to that, high availability and sustainability of the materials used to fabricate secondary batteries will consequently lower their costs as compared to the primary battery. Amongst secondary batteries, Li-ion batteries had tremendously gone through various improvements in order to provide high capacity with lower cost. Nonetheless, a deeper understanding of safer and more reliable materials for the electrode of Li-ion batteries is required. Therefore, in order to fabricate high capacity and reduce cost of Li-ion batteries, it is important to enhance the performance of readily available rechargeable batteries for high power applications by applying the knowledge of nanotechnology during synthesizing the cathode material particularly.

2.1 What is a lithium-ion battery

Important features that determine the range of rechargeable batteries include specific energy (measured in Wh), which is defined as the total amount of energy that a battery can store, the specific and volumetric energy density (Wh kg^{-1} and Wh l^{-1} respectively), which depict how much energy a battery can hold in proportion to its mass and volume, as well as the power density (W kg^{-1}), which describes how much energy the battery is able to supply to a device. Manufacturing this kind of batteries using $LiCoO_2$ cathodes and carbon anodes grew spectacularly since its first commercialization by Sony in the early 1990s [4]. Figure 1 demonstrates that Li-ion batteries possess the highest specific energy density and volumetric energy density compared to other available rechargeable batteries in instance Ni-MH, Ni-Cd and lead acid. Credited to these advantageous properties, Li-ion batteries are used in a wide range of application from mobile phones to power tools. In addition, the substantially lighter weight (approximately 35% less than Ni-MH) and smaller size of Li-ion rechargeable batteries granted them to replace Ni-MH for use in portable applications.

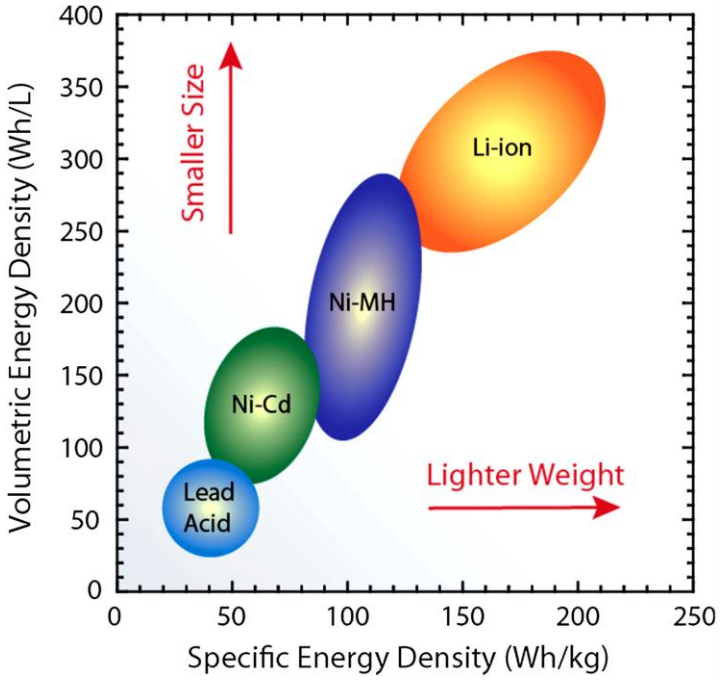

Figure 1: Comparison of different battery systems in terms of volumetric and gravimetric energy density [5]

Typically, a Li-ion battery consists of a number of cells connected either in series or in parallel to provide the desired voltage and power for certain appliances. Each cell is basically composed of an electropositive electrode (anode), an electronegative electrode (cathode), an electrolyte and a separator.

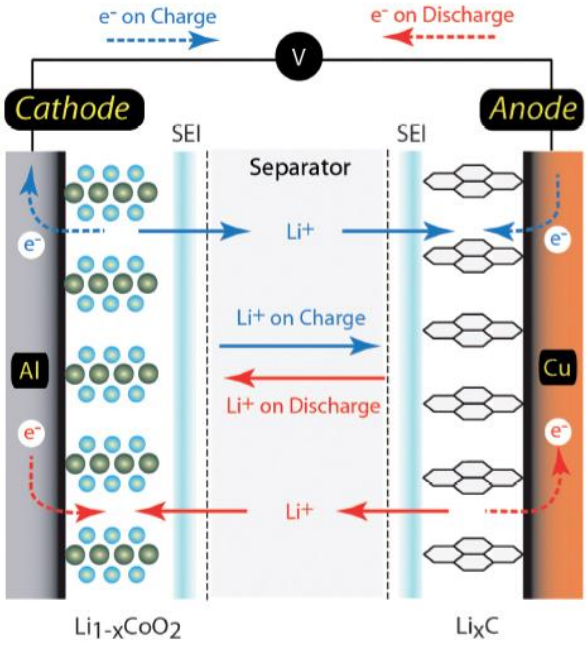

Figure 2: Schematic diagram of a typical commercial lithium ion battery mechanism during charge and discharge [5]

Figure 2 illustrates a schematic diagram of a standard Li-ion cell with a graphite anode, lithium metal oxide as the cathode, an electrolyte and separator. Cathode (transition metal oxides) and anode (graphite) materials commonly exhibit a readily unchangeable host for intercalation of Li^+ ions in. Generally, lithium ions operate based on a redox reaction at positive and negative electrodes. Upon charging, Li^+ ions deintercalate from the positive electrode, travel through the electrolyte and intercalate in the negative electrode and remain there. During this time, the battery will store the chemical energy. As lithium ion batteries discharge, Li^+ ions deintercalate from the anode and move back to the positive electrode across the electrolyte. During discharging, electrons flow in the same direction as the ions around the outer circuit producing the energy for the loaded devices. Since Li^+ ions migrate back and forth between the anode (negative electrode) and cathode (positive electrode) upon charging and discharging, this type of batteries are sometimes referred to as 'rocking chair' batteries. Particularly, Li-ion batteries are assembled in

'discharged' state where the Li^+ ions are available in cathode sites. Therefore, as the source of Li^+ ions relies heavily on the positive electrode, their performance is habitually related to the nature of the positive electrode used. For this reason, altering the properties of readily known cathode materials would consequently enhance the specific capacity of Li-ion batteries.

2.2 Cathode materials

The cathode electrode is where the reduction process occurs during the discharging process. During this process, Li^+ ions will be intercalated into the cathode material along with reduction in valence state of redox-active species such as cobalt or iron from 3^+ to 2^+ while the current flows in different direction powering the load applied. Li^+ ions intercalating into $FePO_4$ during discharge process yield $LiFePO_4$ as shown in Eq 1.

$$Fe^{III}PO_4 + x\,Li + x\,e^- \rightarrow x\,LiFe^{II}PO_4 + (1-x)\,Fe^{III}PO_4 \qquad \text{Eq 1}$$

It is shown from this reaction that the material used as cathode electrode should consist of a transition metal for allowing reduction and oxidation processes. According to that, discharging involved with the insertion of Li^+ ions into the metal oxide structure should alter its crystal structure insignificantly. If the crystal structure changes significantly, instabilities of the material could occur that are capable to cause hazard conditions especially when the batteries are exposed to extreme condition. As a prerequisite it is of importance for the material to be used as cathode material to withstand structure changes during intercalation/deintercalation of Li^+ ions. Based on this criteria, Whittingham [6] suggested that any materials must possess the following requirements in order to be eligible as intercalation/deintercalation host for Li-ion batteries:

- comprise a readily reducible/oxidizable ion, for instance a transition metal
- allow to intercalate/deintercalate with lithium while maintaining its structure
- be capable to provide high voltage by reacting with lithium with a high free energy (referring to Gibbs free energy which is the higher the free energy will consequently rose the cell voltage) according to the equation as, $LiMe^{3+} \rightarrow Me^{2+} + Li + e^-$
- provide high reaction rates with lithium during insertion and removal to provide high power
- good electrical conductivity
- must be low-cost and environmentally benign and be available in abundance

Whittingham [7] was one of the first introducing rechargeable Li-ion batteries. In his first attempt, TiS_2 was used as the cathode material followed by a layer of oxides. This was the $LiCoO_2$ in the first range of commercial lithium ion batteries by Sony Energytech Inc. Since

then, various numbers of cathodes were found which are classified according to their structure. Figure 3 depicts various materials that may be potentially used for cathodes in Li-ion batteries. The most widely used cathode materials in current Li-ion batteries are the layered lithium transition-metal oxides (Figure 3), especially $LiCoO_2$ and $LiNiO_2$. While $LiNiO_2$ produces a slightly higher capacity compared to $LiCoO_2$, it is chemically and electrochemically unsteady, which causes greater problems during synthesis and commissioning. Capacity resembles how much electric charge a material can store and it is known to be strongly related to the material open circuit voltage and applied current.

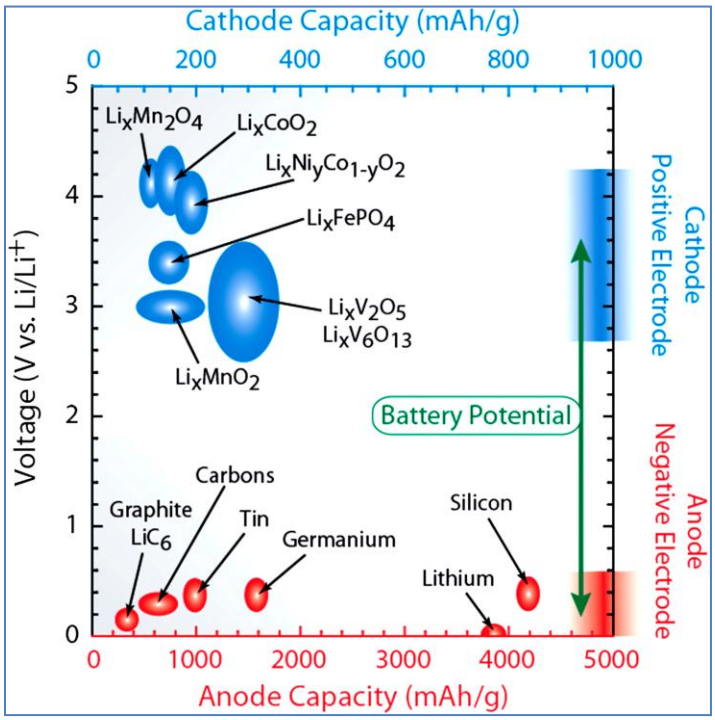

Figure 3: Comparison of the performance of various anode and cathode materials in terms of voltage and capacity [5]

Li_xCoO_2 is superior to $LiNiO_2$ in terms of its chemical and electrochemical characteristics and ability to provide a capacity of 140 mAh g^{-1} for x = 0.5. Nonetheless, its usage has been limited due to reasons such as its reversible capacity normally being restricted to x = 0.5. The reversible delithiation beyond this value is related to its safety issue which in turn is related to its structure. When the batteries are overcharged, oxygen will lose its bond to Co and is released. This exothermic reaction inside the cell can escalate in fast temperature rises leading to possible explosions [8]. Its high cost due to its low availability suppressed its usage for large-capacity

batteries, such as for automotive applications. Furthermore, Co is a toxic material and thus batteries using Co as a cathode material would be unsafe for nature. Even though, cathode materials fabricated using layered oxides ($LiCoO_2$) have proven to offer high energy and cycling stability up to a thousand times, several other $LiMO_2$-type cathodes (where M = Co, Ni, Mn, or V) have been investigated due to safety and cost issue of layered oxide $LiCoO_2$. Instead of using a layered oxide, works have been dedicated to produce different combinations of transition metals including $LiNi_{0.8}Co_{0.15}Al_{0.05}O_2$ and $LiNi_{0.8}Co_{0.15}Al_{0.05}O_2$. Both of these possess good cycle characteristics, but the latter has better safety characteristics [9].

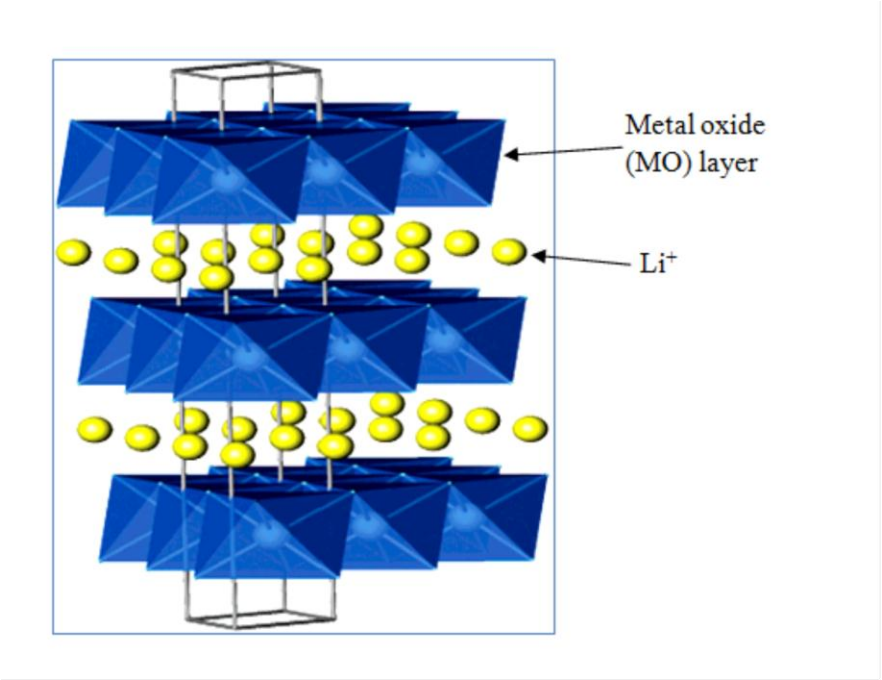

Figure 4: Layered structure of LiMO ($LiNiO_2$, $LiTiS_2$, $LiCoO_2$) type material with lithium ions between the transition metal oxides [10]

Another type of cathode being investigated is the spinel structure of $LiMn_2O_4$ which has 117 mAh g^{-1}, that is about 10% less than that of $LiCoO_2$. This material is much cheaper and relatively less toxic. Yet, $LiMn_2O_4$ is particularly unsuitable for high power and high energy Li-ion batteries applications since it offers moderate capacities and currents only at high temperatures [11].

The olivine structure of $LiFePO_4$ which was first reported by Goodenough in 1997 [12] has gained attention as a candidate for cathode material. Hundreds of publications concern the

development and enhancement of this material as its appealing advantages including high theoretical capacities of 170 mAh g^{-1}, safety, costs, and its effect on the environment is insignificant. However, low electronic and ionic conductivity of $LiFePO_4$ that significantly caused bad rate retention has hindered its usage as cathode material for Li-ion batteries. In order to overcome this problem, three main solutions are known to aid the poor electronic and ionic conductivity of $LiFePO_4$ which is by reducing the particle size from micrometer to nanometer, coating with conductive carbon, and/or doping with metal ions (i.e., Mn, Cu, Ti, Zn, etc.).

Therefore, this thesis focuses on developing $LiFePO_4$/C and $LiFe_{(1-x)}Mn_xPO_4$/C by applying all three main solutions aforementioned to create even improved electrochemical properties that could meet the demand of Li-ion batteries for high power and energy applications. Further explanation about $LiFePO_4$ is supplied in the following section.

2.3 $LiFePO_4$

$LiFePO_4$ has been used in Li-ion batteries as cathode electrodes since its first introduction as cathode material by Padhi et al. in 1997 [12]. Olivine (magnesium iron silicate) type $LiFePO_4$ with triphylite structure encompasses a high theoretical capacity of 170 mAh g^{-1}, a 33% lower price than commercial $LiCoO_2$ and high intrinsic safety. The two phases of electrochemical processes which are oxidation and reduction evolve with a flat 3.4 V vs. Li voltage. Abundance of Fe component in $LiFePO_4$ creates huge advantages towards material availability and sustainability. $LiFePO_4$ has a triphylite system during lithiation and a heterosite system during delithiation. This implies that $LiFePO_4$ is chemically and thermally stable during charging as it exists in triphylite system where the strong covalent bonding between oxygen and phosphorus atom rule out any explosion/fire possibilities in case of short-circuiting [13]. In the meantime, heterosite $FePO_4$ is also thermally stable in delithiation state. Driven by these two important merits of chemical and thermal stability, $LiFePO_4$ has gained huge attention as it can promisingly be used as cathode material in various field including electric vehicles.

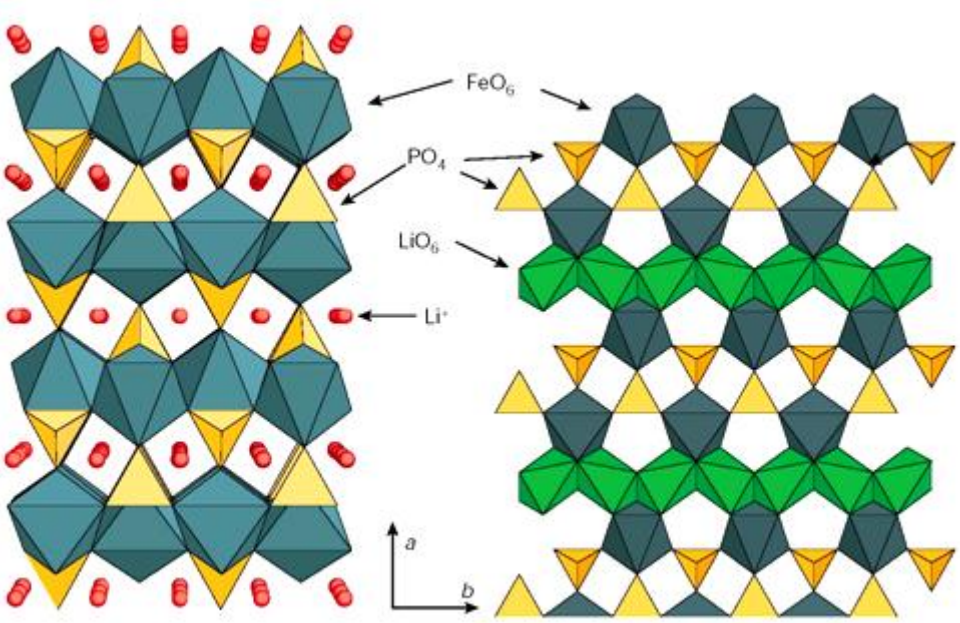

Figure 5: Schematic representation of the triphylite and heterosite structures of $LiFePO_4$ (a) and $FePO_4$ (b), respectively [11]

Table 1: Lattice parameters and unit cell volume for triphylite and heterosite phases [14]

Material	$LiFePO_4$	$FePO_4$
Space group	Pnma	Pnma
a (Å)	10.33	9.81
b (Å)	6.01	5.79
c (Å)	4.69	4.78
Volume ($Å^3$)	291	272

During delithiation, Li^+ ions are extracted from $LiFePO_4$ yielding $FePO_4$. As shown in Table 1, a small increase in the *c*-lattice constant (by 1.9%) is observed along with decreases of the *a* and *b* parameter (by 5 and 3.9%, respectively) during delithiation. Accordingly it is observed that the volume is also reduced by about 6.8% after delithiation. The transition from

triphylite system of $LiFePO_4$ to heterosite $FePO_4$ did not change the olivine structure indicating stable structural framework of $LiFePO_4$ upon charging and discharging process. Accompanied with this advantage, this material is known to have superior thermal stability which is required for high power density applications. Figure 2.5 shows a unit cell from both structures. They share the same olivine family with a different Pnma space group due to existence of lithium chains in the triphylite system. The triphylite structure consists of edge-shared PO_4 tetrahedra which are thermally very stable. Strong covalent bonds between P^{5+} and oxygen form $(PO_4)^{3-}$ units and rule out any risk of oxygen release compared to layered oxides in high states of charge [15, 16]. Padhi et al. [12] reported that the open circuit voltage of any material is normally determined by the Fermi level since a higher working voltage is related to stronger covalent bonding of polyanions. The iron phosphate inside $LiFePO_4$ ideally provides a lower Fe^{3+}/Fe^{2+} redox energy level indicating higher open circuit voltage *vs.* Li. Further works done later by Jiang and Dahn [17] proved that the strong covalency of the P-O bond also stabilizes the anti-bonding Fe^{3+}/Fe^{2+} state and thus boosts up the redox potential of Fe^{3+}/Fe^{2+}. LiO_6 octahedra are positioned in the interstitial spaces of the $LiFePO_4$ framework leading to endless chains along the *c*-axis, thus providing a 1D highway for lithium transport upon delithation and lithation. However, corner-shared FeO_6 octahedra which are intermittently connected to each other cause a bad electronic conductivity of $LiFePO_4$. The low electronic conductivity of this material ($<10^{-9}$ S cm^{-1}) in combination with slow lithium ion diffusion leads to bad rate capability [18], which indirectly harnesses its potential to be commercially used for Li-ion batteries. However, various attempts were identified and exercised in order to solve this problem as outlined below:

- Reducing the particle size of $LiFePO_4$ [19, 20]
- Coating the particles' surface with conductive carbon [21-23]
- Lattice engineering by doping with supervalent cations [24-27]

2.3.1 Reducing the particle size

$LiFePO_4$ is known to be a mixed ionic-electronic conductor whereas the transport phenomena are facilitated by lithium ions and electrons. Thus, diminution of the transport passages for both electrons and ions could be a great potential in enhancing the electrochemical performance of this material. Essentially, electronic conductivity of $LiFePO_4$ would be dramatically improved by downsizing the particle size to nanometer region during synthesizing step. Modern

technology allows for utilization of nanoengineering towards fabricating nanomaterials with better physical and chemical properties. Below is a list of some advantages of reducing the size of $LiFePO_4$ to less than 100 nm:

- Particularly, at higher current enables an increased in energy storage capacity beyond what the microparticles would be able to provide as nanoparticle has higher surface ratio and lower mechanical stress
- fast charge-discharge kinetics owing to a short transport distances in the solid
- better cyclic stability especially at higher currents due to the huge specific surface area that is available for Faradaic reactions
- greater contact area between electrode/electrolyte leading to increase in charge/discharge capacity at high current rate
- reduce charge/discharge time due to short path length

There are also disadvantages in using nanosized $LiFePO_4$ that could harm the electrochemical properties. These are identified as follows:

- low tap density that consequently leads to low volumetric energy density
- requirement of supporting materials such conductive carbon, binder, current collector
- high specific surface area and less coordinated surface atoms may result in surface reactions and particle dissolution in electrolyte which consequently leads to reduction in cyclic and calendar life [28]

Hence, it is a great challenge for the researcher to bring the size to nanometer range while maintaining stable cyclic performance especially at high current rate. In this work, nanotechnology will be applied to fabricate nanosized $LiFePO_4$/C and $LiFe_{(1-x)}Mn_xPO_4$/C that could sustain high capacity at elevated current applied (i.e., more than 1 C rate).

2.3.2 Carbon coating

Besides lowering the particle size, carbon coating is known to be effective in providing drastically improved electronic conductivity in $LiFePO_4$ from 10^{-9} to 10^{-4} S cm^{-1} [23, 29-31]. Additionally, coating with carbon enables suppression of the grain growth during the formation of $LiFePO_4$ by heat treatment at elevated temperatures (500–800°C) while it also acts as a reducing agent for iron species (Fe^{3+} to Fe^{2+}) [32, 33]. The most important advantage is that the active

material is expected to be totally utilized at higher current rates increasing specific properties with respect to the desired electrochemical behavior for automobile applications. On the other hand, carbon coating creates several problems such as decreasing the tap density that leads to low volumetric energy density of composite $LiFePO_4$ as well as the energy density of the battery's cell, increasing the processing cost and restraining the crystallinity of $LiFePO_4$ [34].

Meanwhile, the effectiveness of carbon coating depends solely on the structure of the coated carbon, the homogeneity, thickness and also amount and type of precursor used as the coating source [29, 35-37]. The structure and electronic conductivity of composite $LiFePO_4$/C typically depends on how high and long the temperature is applied for pyrolyzing the sample and the sort of precursor used [29]. Typically, performing an in situ carbon coating provides better conductivity and morphology compared to the addition of pre-existing carbons into $LiFePO_4$ [38]. Doeff et al. previously mentioned that conductivity of carbon coated $LiFePO_4$ increased when applying higher temperatures exceeding 700 compared to 600°C [39]. The reason is because carbon consists of disordered (sp^3-coordinated) and graphite (sp^2-coordinated)-like structures that would both change according to the heat used. Greater temperatures (> 700°C) provide more graphite-like structure than lower temperatures (< 600°C), thus resulting in better electronic conductivity of $LiFePO_4$ [31]. The thickness as well as the volumetric amount of the carbon coating must be tailored to obtain an optimum performance of the active materials. High loading of carbon increases the electronic conductivity whereas too thick of a coating will jeopardize the electrochemical performance of composite $LiFePO_4$ as the path for lithium movement is blocked by excess carbon. On the other hand, too thin carbon coating is insufficient with respect to electronic conductivity and leads to poor cyclic and rate performances. Cho et al. [40] employed solid state reactions to produce $LiFePO_4$/C that delivered 151 mAh g^{-1} at 0.2 C and found that the amount of residual carbon coating was directly proportional to the carbon thickness as 2.28 wt% of carbon resulted in 4–8 nm carbon thickness. Instead of that, they showed that a lower amount of carbon (1.25 wt%) led to a carbon thickness of 2-6 nm which was capable to provide a discharge capacity of only 137 mAh g^{-1}. Zhang et al. [41] described that the amount of carbon content increases significantly with increasing amount of the carbon source glucose applied to the $LiFePO_4$ precursor. They reported that 25 wt% of glucose decomposed during heating at 700°C produced 6.8 wt% of carbon with a nonuniform thickness of 2.5–5.5 nm capable to provide sufficient electrochemical properties with 154 mAh g^{-1} at 0.2 C. Moreover, $LiFePO_4$/C with particle

size ranges from 100–500 nm coated with 2.6 nm carbon thickness were capable to withstand high current with a discharge capacity of 110 mAh g^{-1} at 10 C [42]. Moskon et al [43] reported that minimum amount of carbon content (1 wt%) is theoretically sufficient but experimentally insufficient as a minimum of 1.5–2 wt% of carbon content is required to create a continuous coating layer. Based on current studies, the required amount of carbon coating should be 1–4 wt% whereas the thickness should be dense and uniform around 2–3 nm [44, 45]. By using the optimal quantity of carbon, the total amount of conductive carbons used in the electrode formulation should be reduced in order to maintain a high tap density of composite $LiFePO_4$. In this work, the amount of carbon will be varied in order to find an optimum amount with respect to electrical conductivity and superior electrochemical properties at higher current rate.

2.3.3 Doping with various cations

Another promising method to improve the electrical conductivity of $LiFePO_4$ is doping with metal ions such as Nb^{5+}, W^{6+}, Zr^{4+}, Ti^{4+}, Al^{3+}, Co^{2+}, Mg^{2+}, Ni^{2+} and others [25-27, 46, 47]. Doping the supervalent ions is possible at either the M1 or M2 sites, which resemble the Li and Fe sites, respectively (see Figure 6). Soon after, much work was devoted to doping the supervalent cations on the Fe-site in order to increase the electronic conductivity and lithium-ion diffusion efficiency while doping at Li-site leads to shorten the diffusion path along the one-dimensional Li channels [48-52]. This method increases the conductivity by order of two to eight.

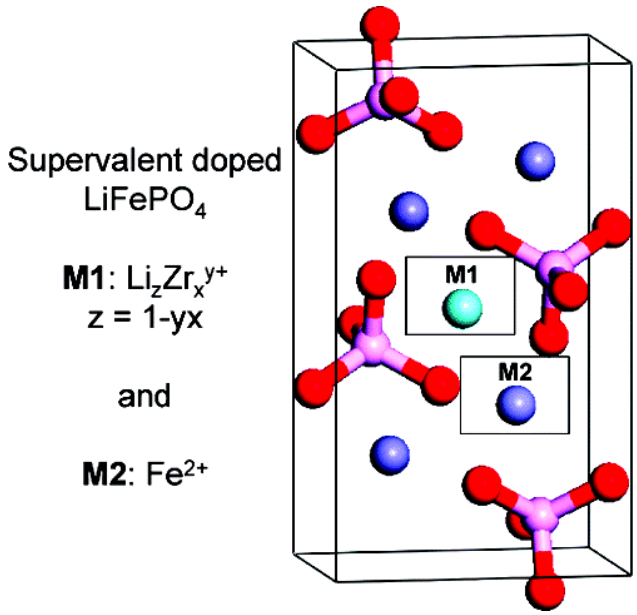

Figure 6: Atomic structure of olivine $LiFePO_4$ illustrating the M1 and M2 sites for doping atoms [53]

The question is still raised to whether other conducting phases such as carbon or ferromagnetic iron phosphide (Fe_2P) or iron phosphocarbide ($Fe_{75}P_{15}C_{10}$) will coexist during synthesis step [25, 47, 48, 50]. Fisher et al. [54] previously conducted modeling studies of doping on either the Li or Fe site and the results showed that electronic conductivity seemed to be similar to undoped $LiFePO_4$. The effect of doping is extremely minimal on the electrochemical properties of doped and undoped materials as described in earlier literature [55]. As dopant atoms such as Zr, Nb and Cr in $LiFePO_4$ are occupied primarily on the M1 sites, Li diffusion is suppressed by jamming of Li-diffusion channels [53]. Recently, extensive studies on doping $LiFePO_4$ with Mn^{2+} have been recognized to be able to augment the electrochemical performance of $LiFePO_4$ [56-59]. Additional details concerning doping with Mn are elaborated on in the following section.

2.4 Manganese-doped $LiFePO_4$

Similar to iron, manganese has advantages such as high availability, very low cost and nontoxic nature. As the redox couple of Mn^{3+}/Mn^{2+} is located at 4.1 V versus Li^+/Li, doping with a certain amount of Mn is potentially suitable to enhance the energy density of $LiFePO_4$ due to its higher voltage compared to Fe^{3+}/Fe^{2+}. The first work of this sort, conducted by Padhi et al. in 1997 [12], constituted doping different amounts of iron into olivine $LiMnPO_4$ instead of valence

substitution of Fe with Mn and showed promising electrochemical behavior. Anon, a number of research groups concentrated on altering the $LiFePO_4$ with various contents of manganese using different routes of preparation including solid-state reaction [56, 58, 60-66], sol-gel [61, 67, 68], hydrothermal [69], mechanical activation [59, 70-72], spray pyrolysis [57] and glass ceramic route [66]. These works were all conducted with a similar aim, that is seeking the best electrochemical performances suitable for high power and energy applications i.e., EV and HEV. Formerly, Yamada et al. [62] stated that the Mn-rich phase of $Li(Mn_yFe_{1-y})PO_4$ where $y > 0.8$ is inappropriate for battery applications. This was in parallel with the work done by Goodenough's group [12] who also gave a similar statement. Later, a group from Sony Corp. [73] found that the highest energy density (590 Wh kg^{-1}) with elevated tolerance towards intense heat was attainable by utilizing a high manganese content ($x = 0.75$) in $Li(Mn_xFe_{1-x})PO_4$. Incongruently, the redox potential of $Fe^{2+/3+}$ gradually decreases with increasing Mn content from 0.25 to 0.75 mol% and the least performances are obtained by doping 0.75 mol% of Mn into $LiFePO_4$ [69]. A low manganese content of 5 mol% was found to improve the electronic and ionic conductivity of $LiFePO_4$ leading to a discharge capacity of 140 mAh g^{-1} at 0.1 C rate [31]. Lee et al. [70] and Xu et al. [74] applied 10 mol% of Mn in $LiFePO_4$ and stated that significant improvement in the electrochemical performances was obtained with 120 mAh g^{-1} and 94 mAh g^{-1} at 1C and 10C, respectively. The latter possessed a mean particle size between 100–200 nm while 1–3 μm with 4 wt% carbon content for the former $LiFe_{0.9}Mn_{0.1}PO_4/C$. Martha et al. [65] described that substitution of Mn^{2+} ions for Fe^{2+} using solid-state reaction was capable to provide superior capacity of $LiFe_{0.8}Mn_{0.2}PO_4/C$ at 1 C (150 mAh g^{-1}) at high surface area (65 m^2 g^{-1}) and a carbon content of 10 wt%. Year after, Zhang et al. [75] produced $LiFe_{0.8}Mn_{0.2}PO_4/C$ with 100–300 nm particle size with 18 wt% carbon content using solid-solution method that capable to deliver 80 mAh g^{-1} at 2 C. The same composition of $LiFe_{0.8}Mn_{0.2}PO_4/C$ reported by Lin et al. [64] delivered 131 mAh g^{-1} at 1 C rate at a stable cycle performances of up to 40 cycles. Recently, Li et al. [76] introduced acetylene black into $LiFe_{0.8}Mn_{0.2}PO_4/C$ via sol-gel method to improve the electronic and ionic conductivity of $LiFePO_4$. The addition of acetylene black into $LiFe_{0.8}Mn_{0.2}PO_4/C$ remarkably suppresses the grain growth and increases the electronic and ionic conductivity leading to good electrochemical behavior with a discharge capacity of 128 mAh g^{-1} at 1 C.

Previous work described earlier demonstrated that doping with Mn would effectively improve the electrochemical properties of $LiFePO_4$ especially at current rate of higher than 1 C.

Still, the remaining question concerning the amount of Mn into $LiFe_{(1-x)}Mn_xPO_4/C$ composition that can burst the electrochemical performances remain unanswered. Doping with larger amount of Mn will end up to the existence of a (unwanted) two-step voltage plateau that possibly causes problems in battery applications, whereas smaller amounts of less than 10 mol% will provide insignificant change in the electrochemical properties of the $LiFeMnPO_4$ system [70]. Therefore, a study that looks into the effect of Mn doping on the electrochemical performance of $LiFePO_4/C$ is reported in this thesis. Manganese content of 1, 2, 20 and 30 mol% will be used in this work and the electrochemical performance of $LiFe_{(1-x)}Mn_xPO_4/C$ will be discussed in details.

2.5 Literature review of routes for producing $LiFePO_4$

Various methods for synthesizing $LiFePO_4$ exist, mostly based on solid state and solution methods. While solid state methods typically deal with high temperature treatment of a solid precursor, wet synthesis normally involves a soluble precursor. Detailed explanation and review of both, and other new emerging routes, is provided in the following sections.

2.5.1 Solution method

Solution methods have been developed that are able to fabricate small particle sizes (down to nanometers) with controllable homogeneity to synthesize high purity $LiFePO_4$. The product is able to sustain a high discharge capacity under immense current rates. Hydrothermal, sol-gel synthesis and co-precipitation were nominated under this group for producing $LiFePO_4$.

2.5.1.1 Hydrothermal synthesis

Hydrothermal synthesis is normally conducted in aqueous solutions containing the precursor and heating above the boiling point of water is used. Synthesis of pure $LiFePO_4$ is possible from the heated precursor solution unless coating with conductive carbon is required. In this case calcination at higher temperatures is necessary. The diffusion of ions and growth of crystals is accelerated by the heated water and is relatively fast. Generally, hydrothermal reactions are performed in an autoclave at a fixed temperature that is less than 150°C. As a result, this method is fast, easy, clean and cheap to produce high purity and homogeneous $LiFePO_4$ with particle sizes ranging from 50 nm to 10 μm [77-87]. Initial work concerning the production of $LiFePO_4$ was reported by Yang et al. [77] and found that temperatures as low as 120°C resulted in disordered lithium/iron with about 7% of the iron located in lithium sites. This situation is vulnerable for lithium insertion and removal as the lithium tunnel is one-dimensional. Furthermore, the presence of iron in between would hamper the movement of lithium. Soon after, Whittingham's group found that firing with carbonaceous substances at 700°C promisingly cured this anti-site problem [78]. Optional candidates suitable as a carbon source include sugar, L-ascorbic acid, carbon, multi-walled carbon nanotubes (MWCNTs) The organic surfactant cetyl trimethyl ammonium bromide (CTAB) has proved to greatly enhance the electronic conductivity while suppressing grain growth and oxidation of iron species [77, 79-83]. Meligrana et al. [82] described that the existence of CTAB surfactant not only increased the electronic conductivity but improved the dispersion of precursor to produce evenly distributed particles with a size of 50 nm.

This surfactant also enhanced the cycling performance of $LiFePO_4$. The reaction rate, degree of ionization, particle size and crystallization of $LiFePO_4$ all closely depend on the water temperature [79, 81]. Besides water temperature, two other important criteria should be taken into account during hydrothermal synthesis. These are the water flow rate and precursor concentration as both play an important role in determining the uniformity of $LiFePO_4$ [88]. However, this route is time consuming and expensive with regards to the precursors (Fe source) and unable to produced $LiFePO_4$/C in large amount. This concerns leads to the idea of adapting modified readily available route to produce less expensive and large amount of $LiFePO_4$/C.

2.5.1.2 Sol-gel synthesis

The sol-gel technique is a common method for the fabrication of $LiFePO_4$ with high purity and homogeneity at much lower temperatures than in the solid-state method. A sol is essentially a dispersion of colloidal particles in a liquid (solvent) while gel is an interconnecting rigid skeleton made of colloidal particles with pores of submicrometer dimensions. The particle size and cross-linking ratio strongly influences the properties of the gel [89]. In order to obtain solid-$LiFePO_4$, the gel must be dried and calcined at elevated temperatures to remove the remaining solvent. Some reaction parameters including temperature, pH, time, precursor, solvent, concentration and viscosity will determine the morphology, shape and size of the resultant $LiFePO_4$. The main advantage of sol-gel method is its ability to control the structure of $LiFePO_4$ on a nanometer scale starting from the beginning of the processing stage.

Dominko et al. [90] and Kim et al. [91] produced porous $LiFePO_4$ with a particle size around 100 nm and 12 wt% of carbon after drying the wet precursor (gel) in vacuum or argon atmosphere at 80°C followed by a calcination step between 500–900°C. Additional works related to this study show that slow heating rates (5 K min^{-1}) produce rough structures with low porosity compared to high heating rates (100 K min^{-1}), thus affecting the electrochemical properties of $LiFePO_4$. The occurrence of a porous structure provides more space for the electron-conducting carbonaceous layer and also fastens the transport of Li ions to the $LiFePO_4$ [92-94]. Besides the heating parameter, the nature of solvent is also a key factor in determining the $LiFePO_4$ structure. Commonly used solvents during sol-gel processing are organic solvents i.e., ethanol [95], ethylene glycol [94], N.N-dimethylformamide [96-98] or water with ascorbic acid [98-100] or citric acid [90, 91, 101, 102] as a chelating agent. The sol-gel technique enables production of porous

$LiFePO_4$ with particle sizes around 100 nm with excellent electrochemical performance. The porous structure enhances the specific surface area that leads to a shorter Li^+ ions passage inside the material [90, 94, 95, 102, 103]. Moreover, very thin carbon layers between 1–2 nm can be obtained using citric acid and sucrose as carbon sources in this technique [45, 91]. This is also a promising technique for fabrication of high performance $LiFePO_4$ with spherical and uniform coating in the nanometer scale. However, this method is relatively meticulous and involved a lot of parameter to control such as pH, type of solvent used, concentration, viscosity and others in order to get the desired particle. Therefore, sol-gel is not favor to be used within this work.

2.5.1.3 Co-precipitation technique

Another promising method that produces high purity and small size $LiFePO_4$ currently being used by some researchers is co-precipitation. Practically, all the precursors are mixed in a solvent and let to co-precipitate by controlling the pH value of the solution. The resultant slurry consists of an amorphous $LiFePO_4$ that is filtered, washed and dried before calcination at higher temperatures (500–800°C) for several hours under inert atmosphere [104-112]. Depending on the type of precursor used and the calcination temperature, nanometer sized (<40 nm) $LiFePO_4$ [105, 109] with promising electrochemical behavior is obtainable with this method. Composite $LiFePO_4$/C having size of 200-300 nm with carbon coating of 2–3 nm shows a palpable discharge capacity of 125 mAh g^{-1} at 0.1 C rate and superior retention was fruitfully fabricated using this method in combination with sonochemical reactions [113]. Despite the promising result descried earlier, this route is unlikeable to be applied within this work since it is complicated to produce large amount of high purity $LiFePO_4$/C as its sensitivity towards pH and precursor strongly affected its purity.

2.5.2 Solid-state method

Instead of solution method, several common techniques associated with solid state chemistry are commonly used to fabricate $LiFePO_4$ powders. These include solid-state reaction, carbothermal reduction, mechanochemical activation and microwave heating. All of these methods generally deal with elevated temperatures to yield an ordered crystal structure of $LiFePO_4$.

2.5.2.1 Solid-state reaction

Solid-state reaction is a conventional method commonly used to produce solid state materials and is widely utilized by most researchers worldwide to synthesize $LiFePO_4$. For economic

and performance reasons, manufacturer (i.e., Süd Chemie) employ this method to produce $LiFePO_4$ commercially. This method produces polycrystalline solids from mixtures of solid precursor which are then subjected to high temperature heating around several hundred degree Celsius according to the crystallization temperature of the desired material. Introduced by Yamada et al. to synthesize $LiFePO_4$ [114, 115], this method involves mixing of the precursor without any solvents. It then goes through pelletization, pre-calcination, grinding, calcination again at high temperature and regrinding to yield the desired $LiFePO_4$. Mostly but not limited to, Li_2CO_3 or LiOH have been used as the Li source, $Fe(OAc)_2$ or $Fe(C_2O_4)_2$ for Fe and $NH_4H_2PO_4$ for P, respectively [116]. All the precursors are intimately mixed either by being ball-milled or simply by using a mortar. They are then calcined at low temperatures (300-400°C) to expel the excess gases and decompose the organic parts. To improve the electrical conductivity and to avoid the oxidation of iron species as well as to reduce the oxidation state of Fe^{3+} to Fe^{2+}, carbon coating based on an organic precursor such as glucose [117], sucrose [118, 119], sugar [34], malonic acid [120], cellulose [121] and polymer [122-125] is applied before further heat-treatment at higher temperatures. Excellent electrochemical performance of nano-$LiFePO_4$/C (100–200 nm) having a carbon coating around 2 nm was produced using modified solid-state reaction with addition of lauric acid and citric acid [126].

Upon synthesizing, parameters such as dwelling time and heating temperature play an important role in determining size and purity of $LiFePO_4$ [116, 125, 127, 128]. Yamada et al. [115] mentioned previously that by calcining above 800°C both, trivalent Fe_2O_3 and $Li_3Fe_2(PO_4)_3$ were formed in large enough amounts that made them detectable by X-ray diffraction. A possible reason contributing to this phenomenon is the presence of small amounts of oxygen within the inert gas flow or oxygen gas that has been trapped between the particles. Furthermore, Kang et al. reported the existence of impurity phase Fe_2P that fortuitously contributes to the increase of capacity after the first cycle neglecting the small specific surface area of the particle [116]. Instead of its simplicity, the high energy utilization (high temperature, high energy and long processing time) and repeated grinding results in a relatively high cost for this solid-state synthesis method as compared to other synthesis route described earlier. Moreover, uncontrollable grain growth as a consequence from prolonged heat treatment at high temperatures causes the particles to possess a small specific surface area which is undesirable for high performance Li-ion batteries. Nevertheless, adapting this route together with the new emerging gas-

phase is predicted to overcome the small specific surface area leading to promising way to synthesized nanocomposite $LiFePO_4$/C and $LiFe_{(1-x)}Mn_xPO_4$/C.

2.5.2.2 Carbothermal reduction method

Being different only by choice of precursor and a less preparative stage, Barker et al. introduced a carbothermal reduction method to synthesize high purity olivine $LiFePO_4$ [129]. Carbothermal synthesis is particularly used to reduce metal oxides. In case of $LiFePO_4$, it involves an iron precursor, namely cheap and readily available Fe_2O_3 or $FePO_4$, while mostly but not only glucose is used as the carbon source which simultaneously acts as a reducing agent [130-135]. This method is highly endothermic, thus temperatures of more than 600°C are required to drive this reduction reaction as lower temperature leads to exothermic CO_2 formation. Two main reactions related to Boudouard's equilibrium normally occur during reduction of Fe^{3+} to Fe^{2+} inside the furnace caused by decomposition of glucose at high temperature can be described as follows:

$$C + O_2 \rightarrow CO_2 \ (T < 650°C) \qquad \text{Eq 2}$$

$$2C + O_2 \rightarrow 2CO \ (T > 650°C) \qquad \text{Eq 3}$$

During thermal treatment inside the tube furnace, glucose will decompose according to the following reactions:-

$$C_6H_{12}O_6 \rightarrow 6C + 7H_2O \qquad \text{Eq 4}$$

In the meantime, by taking into account that $FePO_4$ used as Fe and P source, Li_2CO_3 as Li source, the complete reaction of $LiFePO_4$/C can be simplified as following [134],

$$2FePO_4 + Li_2CO_3 + \tfrac{1}{2}C \rightarrow 2LiFePO_4 + \tfrac{3}{2}CO_2 \qquad \text{Eq 5}$$

or

$$2FePO_4 + Li_2CO_3 + 2C \rightarrow 2LiFePO_4 + 3CO \qquad \text{Eq 6}$$

Adapting this two equation (Eq 4 and Eq 5), required minimum amount of glucose of 16 wt% of total weight ($FePO_4.xH_2O$ and Li_2CO_3) needed to reduce and coated $LiFePO_4$/C. At temperatures higher than 150°C which is the melting temperature for glucose, glucose will decompose into carbon and water. Besides the reduction process, the carbon from this reaction is used to coat the $LiFePO_4$ to yield composite $LiFePO_4$/C. The calcination temperature and amount of

carbon source used while synthesizing can significantly impact the morphological and electrochemical properties of the $LiFePO_4$ [130, 133, 134]. Liu et al. [130] claimed that electrochemical properties of $LiFePO_4$/C are highly influenced by the carbon content whereas higher carbon content (10 wt%) results in sharp increase of specific capacity (160 mAh g^{-1} at 0.1 C) while low amount of carbon content (3 wt%) leads to bad electronic conductivity and incomplete utilization of $LiFePO_4$. The authors also state that glucose used as carbon source is capable to profoundly increase the electrical and electrochemical properties of $LiFePO_4$/C compared to carbon black. Glucose/carbon also reacts as particle growth inhibitor where the particle size of $LiFePO_4$/C was reported to be 100–300 nm for 10 wt% glucose and 300–1000 nm for 2 wt% of glucose after firing at 700°C. Wang et al. [134] described that the particle size of $LiFePO_4$/C is greatly affected by the calcination temperature used during material synthesis. However, the presence of carbon generated from decomposition of glucose has effectively suppressed further growth of the particle at higher temperature. It was shown that calcination temperatures of 650°C produced pure $LiFePO_4$/C with size of around 250 nm and delivered 144 mAh g^{-1} at 1 C. The carbothermal reduction method has been shown to be able to control particle morphology, successfully reducing and stabilizing Fe^{2+} and consequently enhancing the electrical conductivity of $LiFePO_4$ by the presence of conductive carbon around it. Therefore, this method will also be applied within this work to produce nanocomposite $LiFePO_4$/C and $LiFe_{(1-x)}Mn_xPO_4$/C.

2.5.2.3 Mechanochemical activation

Mechanochemical activation is similar to solid-state reaction with the difference of introducing an increased chemical reactivity via application of high-energy ball milling [28, 91, 116, 136-141]. Frequently, both Fe^{3+} and Fe^{2+} are applied as iron precursors, while sucrose and acetylene black are used as the carbon source [28, 85, 91, 142-144]. Since the precursor is blended thoroughly via ball milling before calcination, the resultant $LiFePO_4$/C powder normally consists of a homogeneous particle size distribution (200–300 nm) and high specific surface with good electrical conductivity [85]. Dwelling time (8–24 hours) during calcination varies accordingly to milling time (5–24 hours). Longer milling times result in a shorter time for dwelling [21, 85] and thus less time is required for thermal treatment [117, 143, 145]. This method is favored by many researchers as it is able to yield pure phase $LiFePO_4$ with a reduced thermal treatment time of 15 min and reduced temperature down to 432°C in comparison to the solid-state reaction or carbothermal reduction methods. This is due to the fact that high energy ball milling lowers the cal-

cination temperature for fully crystallization without any impurities detected by X-ray diffraction [85]. However, it is limited by the choice of precursor used and required high-energy ball milling which unappealing to be used within this work.

2.5.2.4 Microwave technology

The main interesting feature of microwave technology with respect to materials synthesis is the short processing time. $LiFePO_4$ can be synthesized within a few minutes via direct heat that is generated inside the $LiFePO_4$ precursor namely lithium carbonate/lithium acetate for Li source, iron acetate/iron oxalate for Fe source and ammonium dihydric phosphate for P source [146-148]. Since the heating rate is adjusted by the applied power, this technique is able to reduce energy consumption and gradually lowers the cost. Song et al. and others have found that activated carbon is the best microwave absorber available, as carbon is cheap, rapidly produces heat and capable of sustaining Fe^{2+} while hinders the formation of Fe^{3+} associated impurities [22, 147, 148]. The particle size and electrochemical properties of $LiFePO_4$ are closely related to the heating time applied during microwave heating. The bigger particles around 1μm that are yielded through longer heating times unfortunately damage the electrochemical performance of $LiFePO_4$ [147]. Also, prolonged heating leads to formation of a conducting phase such as Fe_2P with its amount continuously rising with increasing heating time. This subsequently changes to insulating phase of $Li_4P_2O_7$ after reaching a critical point [149]. Insufficient heating times cause incomplete crystallization of $LiFePO_4$ that can degrade the electrochemical performance [150]. Unfortunately, non-uniformity was observed in the $LiFePO_4$ precursor after the addition of carbon. Thus, this method is unsuitable to be used within this work to synthesize nanocomposite $LiFePO_4$/C and $LiFe_{(1-x)}Mn_xPO_4$/C.

2.5.3 Spray-flame synthesis

Amongst other gas-phase methods, spray-flame synthesis has been employed as a practical way to produce $LiFePO_4$/C powders with appropriate size (ranging from few microns down to 58 nm) and homogeneous morphology for constant rate retention [137, 151-155]. Precursor solutions are ultrasonically [151, 156] or peristaltically [157] sprayed with the aid of carrier gas into a high temperature reactor, either a tube furnace (450–650°C) or a flame reactor. Generally, the $LiFePO_4$ produced using this technique has low crystallinity and requires a thermal post-treatment in inert atmosphere.

Spray-flame synthesis works by burning a combustible solution in a spray flame typically ignited by methane and oxygen to produce nanocrystalline particles. Since the oxidation state of Fe species inside $LiFePO_4$ is mandatory to be Fe^{2+} [158], this technique is unsuitable to directly produce $LiFePO_4$ as the abundance of oxygen inside the reactor will mainly result in Fe^{3+} species. However, by using an enclosed system, Pratsinis' group [159] reported fabrication of core shell nanocomposite $LiFePO_4$/C, with excellent electrochemical properties. They described the formation of $LiFePO_4$ consisting of three steps beginning with particle formation, coating with acetylene black in a second step, and ending with quenching by nitrogen in the last step. The $LiFePO_4$ produce using flame spray pyrolysis was coated downstream before subjected to thermal treatment at 800°C. Nanocomposite $LiFePO_4$/C with a particle size around 70 nm after annealing at 800°C for four hours delivered stable electrochemical cycling at 2 C rate with a capacity of 165 mAh g^{-1}. Conversely, the very high amount of carbon used in the electrode preparation (8.5 wt%) as well as high carbon loading in the nanocomposite itself (10 wt%) lowered the overall capacity gradually.

2.5.4 Other synthesis methods

Other synthesis routes for producing $LiFePO_4$ include rheological phase method [160-166], freeze drying [167-171], electrodeposition [172], glass powder crystallization [173], polyol process [174, 175], template synthesis [100, 176], in-situ polymerization restriction method [177], sonochemical synthesis [113] and ceramic granulation [178]. All of these processing routes provide promising electrochemical properties and only differ by their level of simplicity and potential for large scale production. Reviews show that electrochemical properties are strongly influenced by the mode of preparation as this affects the morphology and homogeneity of the resulting $LiFePO_4$.

Today, solid-state reaction is employed for large scale production of $LiFePO_4$ which basically entails pure precursors and elevated temperatures. Due to the often unknown and/or broad particle size and size distribution of the raw materials such as iron oxide or iron phosphate, less control of morphological properties of the final product is given. From the literature overview it is clear that high performance $LiFePO_4$ cathode materials require a particle size around 100 nm in combination with a functional carbon coating supporting electrical conductivity. Thus, highly scalable spray-flame synthesis was applied in this research. It enables a precisely controlled par-

ticle synthesis with mean particle diameters from a few to a few ten nanometers. In combination with a solid-state reaction and carbothermal route, very good control of final particle size and morphology should be given. This would allow for production of nanocomposite $LiFePO_4$/C with good homogeneity and purity as well as excellent electrochemical properties that are suited for high energy and power applications.

3 Methodology

3.1 $FePO_4$ and $Fe_{(1-x)}Mn_xPO_4$ by spray-flame synthesis

The production of particles from gas phase has been reported over the past few decades. Commonly, titania and silica were produced via this method either in pilot scale or industrially. Gas phase offers high purity, unagglomerated or soft/hard agglomerated products, controllable particle size distribution and varied structures, either porous or nonporous. This attracted the research community and industry to produce ZnO, carbon black, Al_2O_3, SnO_2 as well as many ceramics powders. Gas-to-particle conversion methods are frequently carried out, mostly using hot wall, plasma or flame reactors as briefly described in Table 2.

Table 2: Brief description of typical gas phase aerosol reactors

Type of reactor	Description
Hot-wall reactor	Electrically-heated tubular reactor. Convective heating of the precursor-laden gas flow initiates precursor decomposition and formation of particles. Advantages: Simple arrangement, able to produce a wide range of oxides, non-oxides, semiconductors and metal particles. Disadvantages include high cost of gas-phase precursors and high energy requirement. Low cooling rates often lead to hard agglomerated particles.
Plasma reactor	Formation of particles through physical and chemical processes initiated in a high-temperature plasma. Advantages of the plasma reactor include the ability to work with materials that have a high melting point, and production of unique phases of particles as a result of rapid cooling rates. Disadvantages include high cost of gas-phase precursors and high energy requirement.
Flame reactor	Particles produced by chemical interaction of reactants and the high temperature and the gas-phase products generated by a flame. Further description of this reactor will be given in the next section

Flame synthesis is generally divided into two types depending on the flame being premixed or nonpremixed in terms of the supply of fuel and oxidizer. In spray-flame synthesis, reactants mix within the flame whereas for a premixed flame, the fuel, gaseous precursor and oxygen are perfectly mixed before entering the burner. Flame synthesis offers certain advantages over other methods such as short residence time of the reacting gases in the high-temperature zone

and the possibility to generate high-purity oxide particles in a comparably cheap way. The reactor can handle a variety of precursors which can be volatile or nonvolatile [179]. On the other hand, this technique does have several disadvantages. For instance, it mostly produces hard agglomerates under certain conditions, leading to a wide particle size distribution. It is also difficult to produce a primary particle size of more than 1 µm.

The basic principle of spray-flame synthesis is to use a flame by burning a fuel gas (i.e., methane) and oxygen as pilot and/or synthesis flame and to introduce a spray which typically consists of a dissolved precursor that contains the desired elements. As illustrated in Figure 7, liquid precursors evaporate and decompose once exposed to the high flame temperatures inside the reactor leading to formation of monomers [179]. The monomers then undergo nucleation and surface growth to form clusters which then collide and coalesce resulting in formation of the aggregate particles. These particles are physically held together by weak van der Waals bonds resulting in soft agglomerates, or hard chemical bonds leading to aggregates. The process of particle formation (nucleation, coalescene and agglomeration) is strongly influenced by system conditions such as precursor concentration, dispersion flow rate, precursor flow rate, temperature, pressure, etc. [179, 180].

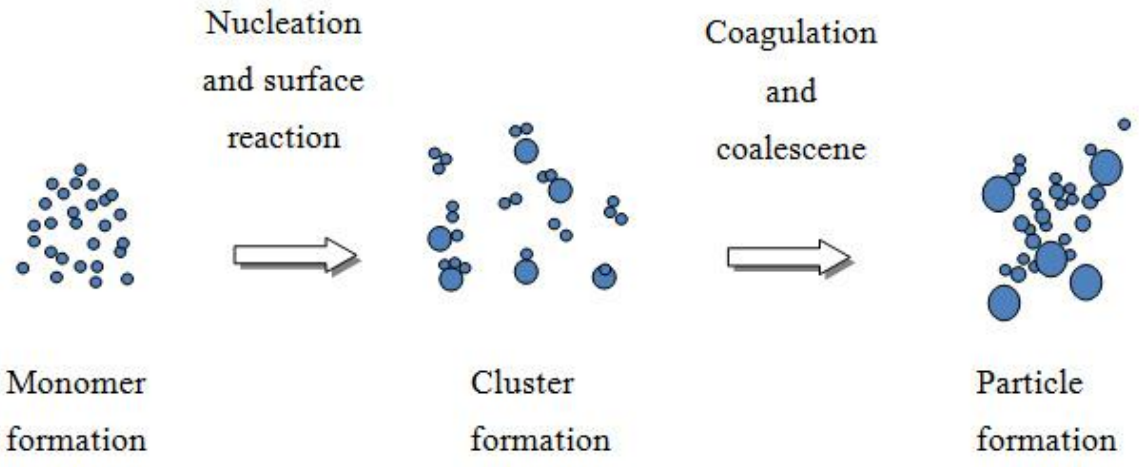

Figure 7: Schematic description of particle formation using gas phase methods

In this work, spray-flame synthesis was employed to produce a large quantity of bare and doped iron phosphates. In spray flames, a combustible liquid containing the respective precursor(s) is ignited by a pilot flame, see Figure 8. The abundance of oxygen in the spray-flame syn-

thesis reactor makes it impossible to synthesize $LiFePO_4$/C directly as the iron species will primarily end up in oxidation state 3^+. Waser et al. [159] described the formation of $LiFePO_4$ using flame spray pyrolysis which were then coated downstream with acetylene in order to yield $LiFePO_4$/C proving that $LiFePO_4$/C could not directly synthesized in one step using this type of reactor. However, it is mandatory to have iron as Fe^{2+} in $LiFePO_4$/C [158]. As an alternative with respect to classical solid state reaction, a combination of nanoparticle-producing spray-flame synthesis and solid state was chosen as the best route to synthesize nanosized $LiFePO_4$/C. It is based on the production of nanosized $FePO_4$ instead in a spray-flame synthesis reactor, which subsequently is transferred into $LiFePO_4$/C with a Li source (Li_2CO_3) and glucose (acts as reductive and carbon source) via solid-state reaction. Thus, the basic raw material, $FePO_4 \cdot xH_2O$ needed to produce the nanocomposite was prepared in the gas phase using spray-flame synthesis. Spray-flame synthesis is a good choice to produce nanosized iron phosphate and doped iron phosphate due to several advantages as:

- its capability to easily adjust the particle size by varying the precursor concentration and flow rate [181]
- its possibilities to offer a wide choice for the metal precursors and solvents
- its scalability for large production of nanoceramic materials used in battery application, thus lowering the production cost of battery itself [182]
- its high production rate at lab scale (up to 5 g h^{-1} depending on concentration used)

Figure 8 shows a sketch of the spray-flame synthesis reactor used in this work. Various liquid precursor solutions consisting of iron (III) acetylacetonate and tri-butylphopshate (reagent grade, Merck) in toluene (reagent grade, Merck) were prepared with iron and phosphate concentrations of 0.0125, 0.05, 0.2 and 0.35 mol l^{-1}, respectively. The maximum concentration was chosen with respect to the limited solubility of iron (III) acetylacetonate in toluene. The precursor solutions were injected into a flame spray reactor via a water-cooled air-blast nozzle at a constant flow rate of 3 ml min^{-1} using two syringe pumps for continuous operation. A coaxial dispersion gas flow of 5 l m^{-1} O_2 (Air Liquide, purity 99.95%) was used for atomization of the liquid precursor solution. The resulting spray was ignited and stabilized by a premixed methane/oxygen pilot flame at a flow rate of 2.4 l min^{-1} O_2 and 1.13 l min^{-1} CH_4 (Air Liquide, purity 99.95%). An

additional sheath gas flow of 5 l min^{-1} O_2 was fed through a sinter metal ring with an inner diameter of 18 mm and an outer diameter of 34 mm surrounding the supporting flame to ensure complete conversion of the reactants and to stabilize the fluid flow. The gas flows were adjusted by mass flow controllers (Bronkhorst). The flame was located in a 330 mm diameter stainless-steel housing and the product was collected from the exhaust gas on a filter located downstream the spray-flame synthesis reactor. Likewise for $FePO_4 \cdot xH_2O$ doped with Mn, iron (III) acetylacetonate was partly replaced by manganese (III) acetylacetonate while the other parameters were kept constant.

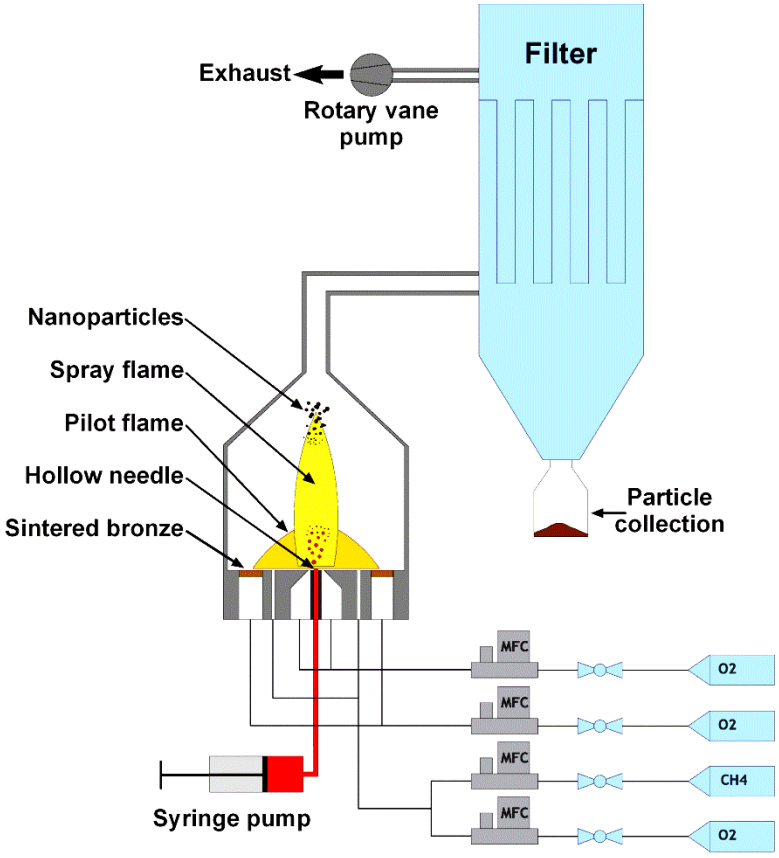

Figure 8: Schematic diagram of the spray-flame synthesis reactor [183]

3.2 Undoped and doped $LiFePO_4/C$ composite from solid-state reaction

Solid-state reaction was employed in this work subsequently after production of amorphous nanosized iron phosphate and doped iron phosphate in order to yield undoped and doped nanocomposite lithium iron phosphate. Generally, solid-state reaction involves mixing of solid reactants and heating at higher temperature to support the required ion diffusion process for the formation of the intended product. Depending on melting temperature of the compounds used, calcination normally takes place between 500–900°C in case of $LiFePO_4/C$ [42, 106, 138, 184, 185]. During calcination, the precursors which are $FePO_4 \cdot xH_2O$ or $Fe_{(1-x)}Mn_xPO_4 \cdot xH_2O$, Li_2CO_3 and glucose will decompose and form $LiFePO_4/C$ and $LiFe_{(1-x)}Mn_xPO_4/C$, respectively. Figure 9 illustrates the sequence of solid-state method applied within this work.

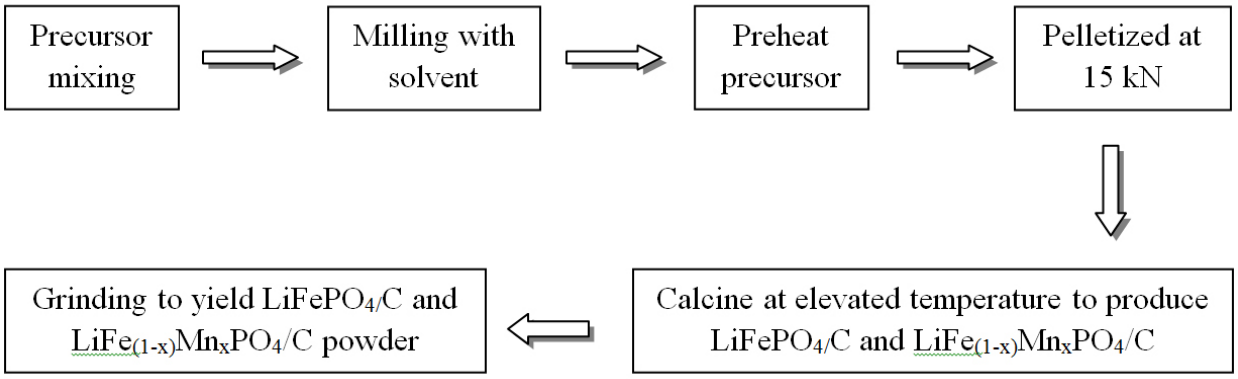

Figure 9: Sequence of steps used for production of undoped and doped nanocomposite lithium iron phosphate

Work conducted within this thesis can be divided into four sections as following:

All powders were mixed using mortar and pestle with addition of analytical grade ethanol, the thoroughly mixed powder was pelletized and calcined for three hours at 150°C and further calcined for 16 hours at 600°C under nitrogen flow. A black-colored product was obtained after cooling down to room temperature.

After the preliminary attempt of mixing the reactants with pestle and mortar, milling was applied in order to provide more homogenously mixed precursors at the initial step. In a standard experiment, the $LiFePO_4/C$ composite material was synthesized via a solid-state reaction from a mixture of the as-prepared $FePO_4 \cdot xH_2O$, Li_2CO_3 (reagent grade, Merck), and 16 wt% of glucose

as the reducing agent and a carbon source. Amount of glucose chose according to the calculation based on Eq 5 and Eq 6 indicates the minimum amount of glucose to reduce and coated the $LiFePO_4$. All the precursors were weighed accordingly and mixed inside a mill (Netzsch, MicroCer) with analytical grade ethanol as the solvent media. Milling was conducted for 12 hours using 0.5 mm zirconia beads and zirconia vial. After drying and pre-heating at 80°C for 24 hours, the dried precursor was pelletized at 15 kN prior to calcination at various temperatures (600–800°C). Pelletization was used to proficiently enhance the interaction between particles to provide a pure and homogeneously distributed final product [185]. In addition to that, glucose content was also varied in the range of 10 to 30 wt% in order to investigate the influence of carbon content towards electrochemical properties of $LiFePO_4$/C.

The $LiFe_{(1-x)}Mn_xPO_4$/C was fabricated accordingly with Mn contents of 1, 2, 20 and 30 mol%. Black colored powders of $LiFe_{(1-x)}Mn_xPO_4$/C were obtained likewise.

3.3 Characterization of synthesized materials

The products made by gas phase synthesis as well as those prepared afterwards by solid-state reaction were characterized by physical and chemical analysis tools. As prepared and calcined samples of $FePO_4$ and $Fe_{(1-x)}Mn_xPO_4$ as well as $LiFePO_4$/C and $LiFe_{(1-x)}MnxPO_4$/C were characterized using BET to determine the specific surface area which consequently provides information about the size of the particles. Because of the amorphous nature of the pristine materials made by spray-flame synthesis, as prepared $FePO_4{\cdot}xH_2O$ and $Fe_{(1-x)}Mn_xPO_4{\cdot}xH_2O$ were calcined at 600°C prior to XRD measurements. This is explained in more detail later in this subsection. Thermogravimetric (TG) measurements were conducted using as-prepared $FePO_4{\cdot}xH_2O$ and $Fe_{(1-x)}Mn_xPO_4{\cdot}xH_2O$ while TEM was carried out using both, as-prepared and calcinated nanoparticles. All the $LiFePO_4$/C and $LiFe_{(1-x)}MnxPO_4$/C samples were characterized using X-ray diffraction (XRD), transmission electron microscopy (TEM), scanning electron microscopy (SEM), X-ray photoelectron spectroscopy (XPS), Mößbauer spectroscopy, electrical conductivity measurements, cyclic voltammetry and galvanostatic cycling measurements. A brief description of the above mentioned techniques is available in the following subchapters.

3.3.1 Brunauer-Emmet-Teller (BET) method

Named after the inventors Stephen Brunauer, P. H. Emmet and Edward Teller, the BET technique is widely applied for measuring the surface area and porosity of particulate materials. This method is based on the adsorption of gas on a surface whereby the amount of gas adsorbed at a given pressure allows for determination of the surface area. BET theory describes that multilayer adsorption occurs at constant, low temperature and elevated pressure. In such conditions, the thermal energy of gaseous molecules is lowered thus providing many gaseous molecules per unit surface area which leads to formation of multilayer adsorption [186]. Nitrogen is used as an adsorbate in this work since it is highly available, pure and contacts well with most of the solids. Samples were degassed under vacuum at 150°C overnight to remove unwanted adsorbents covering the particles before the adsorption measurement is conducted. The phenomenon of gas adsorption over dry particles at increasing partial pressures provides adsorption isotherms which relate the amount of gas adsorbed to the relative pressure. Based on this isotherm, the surface area of the respective materials can be measured. Taking into account the bulk density, the specific surface area as well as a mean particle size is calculated assuming spherical, monodisperse

particles. Following this, the mean primary particle size (d_{BET}) is determined using the following equation, where SSA is specific surface area and ρ is the bulk density of powder:

$$d_{BET} = \frac{6}{SSA.\rho} \quad \text{Eq 7}$$

3.3.2 X-ray diffraction (XRD)

XRD is widely used for identification of chemical compounds based on their crystalline structure. Crystal is the three dimensional repetition of some unit of atoms. When an X-ray beam interacts with the atom's surface, the beam can be scattered either in the same wavelength (unmodified) or longer wavelength (Compton modified scattering) [187]. Unmodified scattering will cause Bragg's reflection (Figure 10). Two in-phase (where *n* is an integer) incident beams with wavelength λ hitting the crystalline material with lattice spacing *d* at an angle θ generate an array of diffracted beams. Since the polycrystalline solid is arranged randomly with certain lattice spacings *d*, Bragg's law is then useful for determination of orientation and spacing of the planes.

$$2d \sin\theta = n\lambda \quad \text{Eq 8}$$

Moreover, the crystallite size of a sub-micrometer particle or crystallite can be calculated using the Scherrer equation shown below:

$$L = \frac{K \cdot \lambda}{\beta \cdot \cos\theta} \quad \text{Eq 9}$$

where L is the mean crystallite of the sub-micrometer particle or crystallite, *K* is the dimensionless shape factor (with a typical value of 0.9), λ is the X-ray wavelength, β is the full width at half maximum (FWHM) in radians (in 2θ) and θ is the Bragg angle. X-Ray diffraction (XRD) was performed in this study using a PANalytical X-ray diffractometer (X'Pert PRO) with Cu K_α-radiation (1.5406 Å) operated at 40 kV and 40 mA.

The diffraction pattern of $FePO_4$, $Fe_{(1-x)}Mn_xPO_4$, $LiFePO_4$/C and $LiFe_{(1-x)}Mn_xPO_4$/C were refined using the MAUD program [188]. MAUD program applies the Rietveld method where the structural intensity profile of XRD is refined by least square fitting calculating the intensity profiles using a model (I^{calc}) until the model profiles matches best with the measured profile (I^{exp}). A

weighted profile known as *R*-factor (R_{wp}) (see Eq. 10) is defined in order to evaluate the difference between the model and measued data,

$$R_{wp} = \sqrt{\frac{\sum_{i=1}^{N}\left[wi\left(I_i^{\exp} - I_i^{calc}\right)\right]^2}{\sum_{i=1}^{N}\left[wiI_i^{\exp}\right]^2}} \qquad \text{Eq 10}$$

where w_i is equal to $1/\sqrt{I_i^{\exp}}$. The value of R_{wp} often used as indicator for the quality of the fit where a small value (<15%) indicates good fitting of the model to the measured data. The trigonal structure with space group of P131 and orthorhombic structure with space group Pnma is applied for fitting the XRD pattern for $FePO_4$ and $Fe_{(1-x)}Mn_xPO_4$, $LiFePO_4$/C and $LiFe_{(1-x)}Mn_xPO_4$/C, correspondingly.

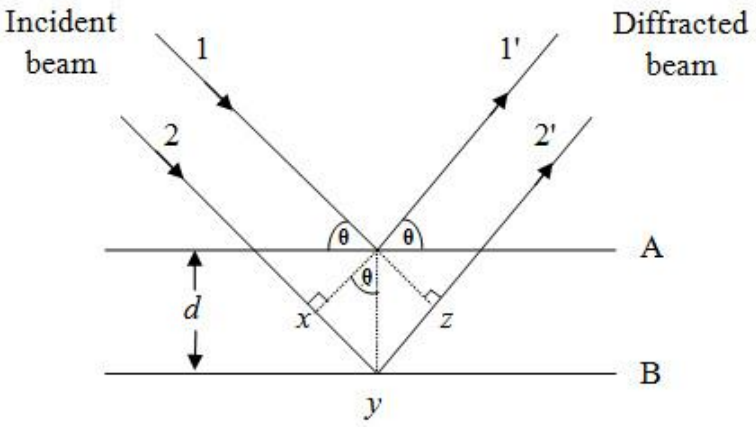

Figure 10: Illustration of Bragg's law for derivation of the diffracted crystal [187]

3.3.3 Transmission electron microscopy (TEM)

Transmission electron microscopy provides information about the morphology and composition of the sample. This information is collected after the accelerated electron beam produced by an electron gun, which is transmitted through an ultra-thin sample inside a vacuum chamber to produce an image. Better images are normally recorded when using high accelerating voltages [189]. In this work, a very small amount of sample was dissolved with ethanol and spread onto a carbon coated copper grid. Morphology of the samples was investigated by transmission electron microscopy (TEM) Philips CM12 with an accelerating voltage of 120 kV.

3.3.4 Scanning electron microscopy (SEM)

Scanning electron microscopy (SEM) is a non-destructive technique commonly applied to examine the morphology, composition and crystalline structure of samples by scanning the sample surface with a beam of electrons. The thin beam of high-energy electrons is used to generate signals at the samples' surface. When the beam hits the sample, electron-sample interactions occurs and produces a variety of signals including secondary electrons and backscattered electrons. The signals derived from interaction electron-sample will provide an image. This image mostly resembles the selected area of the sample surface. Secondary electrons are mostly used to visualize the morphology of the samples while backscattered electrons are normally used to illustrate the contrast in composition in multiphase samples. In this study, information regarding the morphology of the samples was collected using secondary electrons. $LiFePO_4$/C and $LiFe_{(1-x)}Mn_xPO_4$/C powder were cold-pressed at 15 kN prior to SEM measurements. The morphology of $LiFePO_4$/C and $LiFe_{(1-x)}Mn_xPO_4$/C surfaces was determined using a LEO Gemini 1530 operated an accelerating voltage of 5 kV.

3.3.5 Thermogravimetric analysis (TGA)

Thermogravimetric analysis is a useful technique for measuring the weight loss as a function of temperature [190]. The purpose of this analysis is to find out the composition and thermal behavior of the sample at elevated temperatures. In particular, this technique is capable of characterizing the materials that demonstrate weight loss or gain due to decomposition, oxidation or evaporation of volatile species. Thermogravimetric analysis was applied in this study to determine the calcination temperature and the amount of water molecules bound within the as-prepared samples. In this study, thermogravimetric analysis was conducted on $FePO_4.xH_2O$ and $Fe_{(1-x)}MnxPO_4.xH_2O$ by heating the samples from room temperature to 800°C at a heating rate of 10°C min^{-1} using a commercial TGA/DTA instrument (Bähr STA 503).

3.3.6 X-ray photoelectron spectroscopy (XPS)

X-ray photoelectron spectroscopy is normally used for identification of the elements and its neighboring environment on the surface layer of materials due to its penetration depth between 1–12 nm. This technique works on the basis of shooting soft X-rays (Mg K_α or Al K_α radiation) at the surface of samples in a vacuum chamber. Figure 11 shows the emission of photoelectrons from an atom when it is excited by an X-ray photon. These X-rays have sufficient ener-

gy, *hv*, to remove the electrons from the outer shells of the atoms' surface *K* and produce kinetic energy E_K. The binding energy (E_B) of the released atom's photoelectron can be calculated using the following equation, where h is Planck's constant, *v* is the frequency and φ represents the energy required for the electrons to escape from the atom's surface:

$$E_B = h\nu - E_K - \varphi \qquad \text{Eq 11}$$

Since E_B possesses a characteristic value for each element, it is easy to recognize the elements through their binding energy. The resulting spectra normally contain multiple peaks that arise from ejection of electrons from different orbitals [191]. X-ray photoelectron spectroscopy (XPS, SPECS Phoibos 100) was performed to determine the oxidation state of iron in $LiFePO_4$/C and $LiFe_{(1-x)}Mn_xPO_4$/C samples.

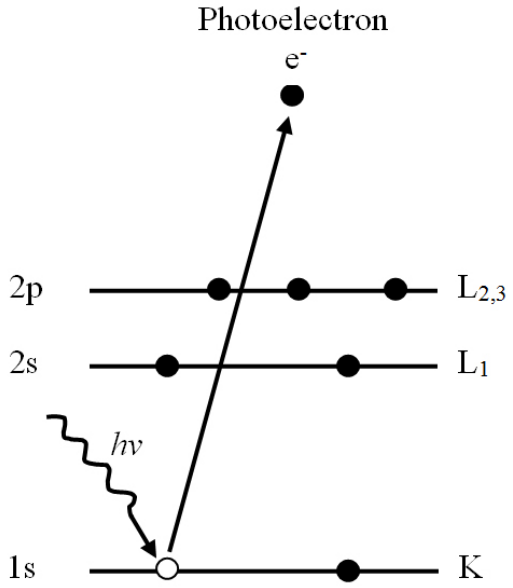

Figure 11: Emission process of characteristic electrons shown for a 1s photoelectron [190]

3.3.7 Mößbauer spectroscopy

Mößbauer spectroscopy is frequently used to examine the valence state of iron which is found in nature mostly as Fe^0 (metallic iron), Fe^{2+}, and Fe^{3+}. This technique is also useful for determining the iron oxide phase via identification of their magnetic properties. It works on the basis of recoilless absorption of gamma rays. The iron nucleus absorbs photons with correct energy which are then measured as transmission of a reduced number of counts at this energy [192]. Normally, ^{57}Co is used as emission source as it decomposes to ^{57}Fe emitting photons with

an energy of 14.41 keV. Mößbauer analysis generally involves three parameters which are as follows:

- Isomer shift – occurs as a result of a difference in *s* (1s, 2s, 3s and etc.) electron density between the source and the absorber
- Quadrupole splitting – splitting of the nucleus energy levels that results from the interaction of the nuclear quadrupole moment with the electric field gradient. Hyperfine splitting – closely related to magnetic materials

In this work, Mößbauer spectroscopy was conducted in transmission geometry using a ^{57}Co source (in Rhodium-matrix) with an activity of about 15 mCi and a Mößbauer drive system operating in constant acceleration mode at room temperature.

3.3.8 Raman spectroscopy

Raman spectroscopy was widely used to identify the vibrational and rotational modes in certain molecules. It works when the sample is illuminated by a monochromatic light (laser beam) thus producing scattering light which is collected by a lens. Inelastic scattering or Raman scattering carries information about the properties of the molecules studied, such as vibrational or rotational. This information can be translated by examining the frequency difference between the incident and inelastically scattered radiation. Raman spectroscopy was carried out in order to determine the chemical bond of the carbon in the nanocomposite post-treated sample [191]. Therefore, in this work, Raman spectroscopy was performed with a micro-Raman system using a wavelength of 532 nm and a liquid-nitrogen cooled CCD for detection. The spot size of the laser beam on the sample surface was focused with a microscope lens to about 1 µm diameter and the spectra were recorded at room temperature in backscattering geometry.

3.4 Electrical measurements

Electrical conductivity measurement of $LiFePO_4$/C and $LiFe_{(1-x)}Mn_xPO_4$/C were conducted using four-point probe measurement. Since $LiFePO_4$/C and $LiFe_{(1-x)}Mn_xPO_4$/C were coated with conductive carbon, it is expected that these samples have high electric conductivity compared to un-coated samples in the range of 0.1–10 S cm^{-1}. Therefore, four point probe measurements were applied to measure the electrical conductivity of $LiFePO_4$/C and $LiFe_{(1-x)}Mn_xPO_4$/C as this method allows for determination of electrical conductivities in the

range of 10^{-4} to 10^{4} S cm^{-1}. The electrical measurements were conducted on the basis of determining the resistance between two electrodes separated by a known distance, t. The measurement setup of the $LiFePO_4$/C and $LiFe_{(1-x)}Mn_xPO_4$/C pellets which can be described as two electrodes that are in line with the current applied. The two electrodes assigned as 1 and 2 is referring to each end of the pellet as illustrated in Figure 12. The other two electrodes designated as 3 and 4 were supplied with a voltage in order to measure the resistance between them. The tips of the probe either touched or slightly penetrated the surface of the sample as shown in Figure 12.

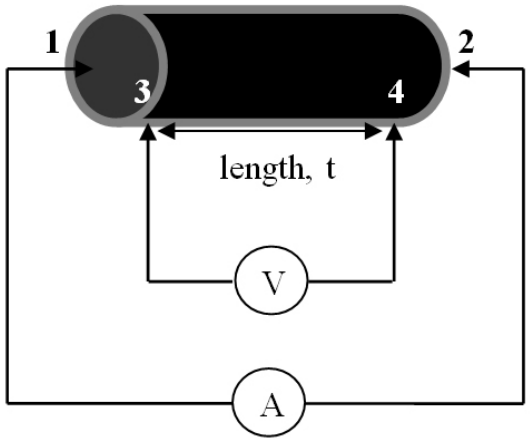

Figure 12: Schematic illustration of four-point probe measurement used in this work

The electrical conductivity was then calculated using the formula below, where σ_b is the bulk conductivity, t is the distance between the two inner electrodes, R_b is the measuring bulk resistance and A is the area of the sample:

$$\sigma_b = \frac{t}{R_b \cdot A} \qquad \text{Eq 12}$$

In this work, $LiFePO_4$/C and $LiFe_{(1-x)}Mn_xPO_4$/C powder were cold pressed with a pressure of 15 kN to produce pellets having 5 mm diameter and 6–9 mm length.

3.5.1 Cyclic voltammetry

Cyclic voltammetry is a common electrochemical technique used to measure the redox reaction, kinetics of electron transfer and phase transition of a voltaic cell [193]. This technique works by measuring the current versus different applied potentials. The differences in energy of working and reference electrodes generate the applied potential. The potential of working elec-

trodes is scanned back and forth linearly with time producing triangular waveforms as can be seen in Figure 13. The scan rate unit is given as V s^{-1} or mV s^{-1}.

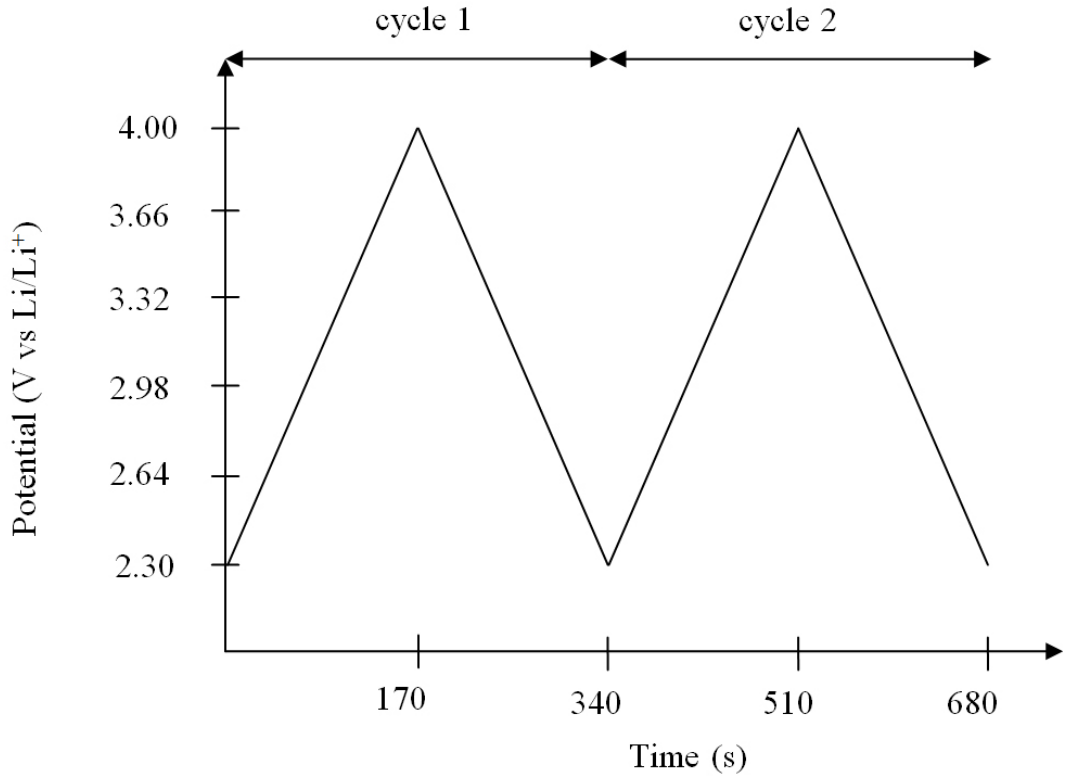

Figure 13: Repetitive triangular potential excitation signal ramped at 0.1 mV s^{-1} between 2.3 to 4.0 V vs Li/Li^+

The current is measured between the counter electrode and working electrode while the potential is measured between the working electrode and reference electrode. The acquired data is plotted as current versus applied potential as illustrated in Figure 14. For the measurement of cathode materials, the scan initially starts with a low voltage and increases to a higher potential before reversing back to the starting potential. An increase in current peak observed indicates the occurrence of an oxidation reaction. The reduction reaction occurs when the current drops. Integral of either anodic or cathodic peak can be simplified as Eq 13.

$$Q = \int_{t1}^{t2} I \, dt \qquad \text{Eq 13}$$

Figure 14 shows the CV of $LiFePO_4$ at a scan rate of 0.01 mV s^{-1} ramped between 2.3 and 4 V vs. Li/Li^+. It is clearly illustrated that the redox reaction occurred whilst Li was extracted and inserted during an electrochemical reaction as stated in the following reversible equation,

$$LiFePO_4 \underset{\text{Discharge(reduction process)}}{\overset{\text{Charge(oxidation process)}}{\rightleftarrows}} FePO_4 + Li + e^- \qquad \text{Eq 14}$$

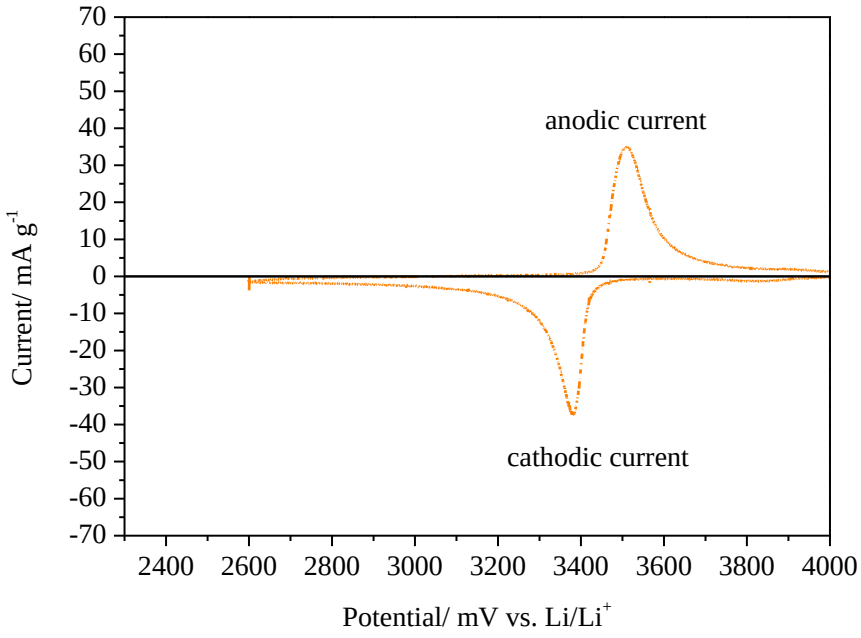

Figure 14: CV diagram of $LiFePO_4$ at a scan rate of 0.01 mV s^{-1} between 2.3 to 4.0 V vs Li/Li^+

In this study, CV measurements were recorded using a Basytec CTS Lab XL battery tester using a voltage between 2.3 and 4.0 V vs. Li/Li^+ with a scan rate of 0.01 mV s^{-1} for $LiFePO_4$/C (first work) and 2.3 and 4.2 V vs. Li/Li^+ with a scan rate of 0.01mV s^{-1} for $LiFePO_4$/C (second work). In the meantime, CV measurements for the Mn doped materials were conducted within a range of 2.6–4.8 V vs. Li/Li^+ with 0.01 mV s^{-1}.

3.5.2 Galvanostatic cycling

Galvanostatic cycling also known as constant current (CC) was done in order to investigate the capability of materials to produce a capacity at a certain current applied. These meas-

urements were conducted at different current rates applied and at each current the measurement was repeated about 3–5 times. From these measurements, information regarding the capacity delivered as a function of current rate can be obtained. In order to measure the capacity, a constant current was applied until it reaches the cut-off voltage. The capacity of the cell was determined by multiplying the discharge current (mA) with the time (h) needed to reach the terminal. The current rate is usually articulated as a C-rate (see Eq 15) which indicates the amount of charge that could be delivered within certain hour with C is the capacity and t is time.

$$C = \frac{1}{t} \qquad \text{Eq 15}$$

For example, $LiFePO_4$ delivering 170 mA (theoretical capacity) within 1 hour is operated at 1 C. Mostly, the cell were tested at very low current rate either C/10 or C/20 initially and this value will be used as experimental capacity during calculation of material's capacity. The specific theoretical capacity of $LiFePO_4$ can be obtained by assuming that 1 mol Li is deintercalated in 1 mol $LiFePO_4$ as shown in Eq 16.

$$LiFePO_4 \underset{\text{Discharge(reduction process)}}{\overset{\text{Charge(oxidation process)}}{\rightleftarrows}} Li^+ + FePO_4 + e^- \qquad \text{Eq 16}$$

Therefore, applying the Faraday equation (see Eq 17), one can calculate the theoretical capacity of $LiFePO_4$. Knowing that the molecular weight of $LiFePO_4$ is M = 158 g mol^{-1}, the Faraday constant is F = 96500 C mol^{-1} and z is number of electron transfer which is 1, theoretical capacity of $LiFePO_4$ is calculated as 170 mAh g^{-1}.

$$\text{Capacity} = \frac{z.F}{M} \qquad \text{Eq 17}$$

Figure 15 shows an example of rate capability of $LiFePO_4$/C at different C-rates. Normally, the capacity of the cell will drop gradually as the discharge current is increased. This is due to diffusion limitations as Li^+ ions movement in one-dimensional channels as well as small electronic conductivity of $LiFePO_4$/C. However, these drawbacks can be reduced by coating with conductive material (i.e., carbon) or by lattice adjustment (i.e., doping with Mn). Therefore, information attained using this measurement is useful to determine the performance of the material as cathode material for Li-ion batteries.

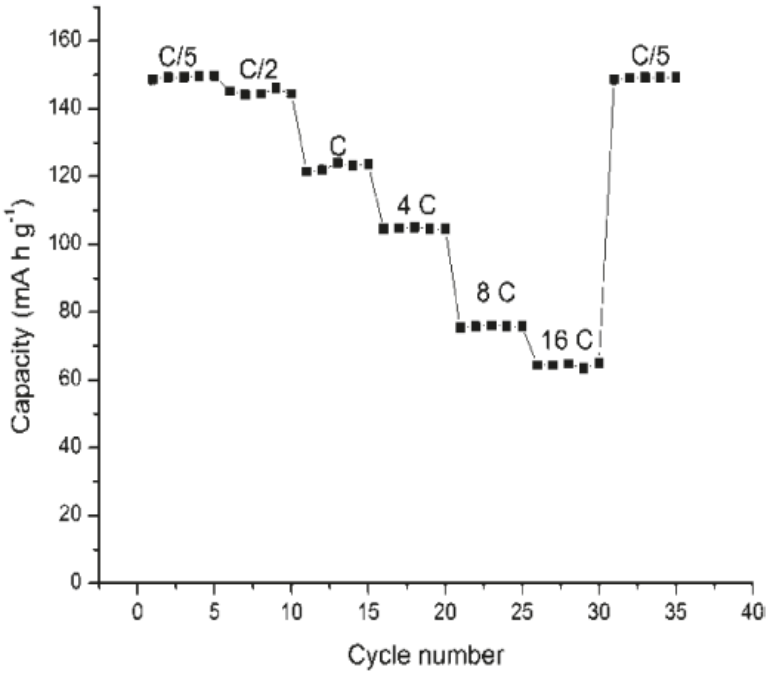

Figure 15: Rate capability of $LiFePO_4$/C at different C-rates [194]

In this work, constant current (CC) tests were performed with a Basytec CTS Lab XL battery tester using a voltage between 2.3 and 4.0 V vs. Li/Li^+ for $LiFePO_4$/C (first work) and 2.3 and 4.2 V vs. Li/Li^+ for $LiFePO_4$/C (second work). Also, CC tests were done with a potential range of 2.6 to 4.7 V vs. Li/Li^+ for Mn-doped $LiFePO_4$/C.

4 Results and discussion

The first part presented in this thesis deals with the production of nanocomposite $LiFePO_4$/C using a combined gas-phase and solid-state reaction. Thus, initial work starts with synthesizing nanosized iron phosphate at 0.0125, 0.05, and 0.2 M using spray-flame synthesis and is further used as iron and phosphate source for post-processing with Li_2CO_3 and glucose to yield nanocomposite $LiFePO_4$/C. The nanosized $FePO_4$ was characterized using BET, XRD and TG. $LiFePO_4$/C produced was characterized using BET, XRD, SEM, TEM, Raman and XPS before electrochemically characterized. The amount of glucose chosen for the first experiments was 16 wt% according to the calculation based on Eq 5 and Eq 6 that signify the amount of glucose need to reduce and coated the $LiFePO_4$. Instead of this calculation, previous work from Liu et. al [195] also showing that 16 wt% of glucose exhibits the best electrochemical properties.

In the second part, examination regarding the effect of the calcination temperature and the carbon content of $LiFePO_4$/C was done knowing that these two parameter have a great influence towards the electrochemical properties of $LiFePO_4$/C [21, 23, 116, 133, 156, 196-199]. The first results also indicated that the spray-flame synthesis of $FePO_4$ from higher concentration (0.35 M) produced using gas-phase were mixed by milling with Li_2CO_3 and glucose and ethanol as solvent to produce nanocomposite $LiFePO_4$/C. The $FePO_4$ with 0.35 M chose to use within this part as these concentration enable higher production rate of 5 g h^{-1} which benefited for further used in large amount during the post-treatment with Li_2CO_3 and glucose in order to investigate the effect of calcination temperature and carbon content towards electrochemical properties of $LiFePO_4$/C. The promising electrochemical properties obtained from the first experiments led to study the effect of different calcination temperatures during solid state reaction using BET, XRD and Raman spectroscopy for characterization. Based on these results, the most promising material was chosen to investigate the influence of varied glucose content, and $LiFePO_4$/C was prepared with different amount of carbon.

The third part of this work deals with the initial idea of doping $FePO_4$ with manganese during gas-phase synthesis. The $Fe_{0.7}Mn_{0.3}PO_4$ was processed with Li_2CO_3 and 16 wt% glucose to yield nanocomposite $LiFe_{0.7}Mn_{0.3}PO_4$/C (similar to the synthesis parameter conducted in the first part but focusing on the doping effect towards the electrochemical properties of $LiFe_{0.7}Mn_{0.3}PO_4$/C).

The fourth part is related to the investigation towards different calcination temperature and amount of Mn doping ranging from 1 to 20 mol%. As obtained as a promising result from the investigations with respect to the carbon content in part 2, $Fe_{(1-x)}Mn_xPO_4$ (x = 0.01, 0.02, and 0.20) were processed with 25 wt% of glucose and calcined at different temperatures

A comparative discussion of nanocomposite $LiFePO_4$/C and $LiFe_{(1-x)}Mn_xPO_4$/C obtained from the second and fourth part is given at the end of this chapter.

4.1 Synthesis of nanocomposite $LiFePO_4/C$

4.1.1 Characterization of $FePO_4$ and nanocomposite $LiFePO_4/C$

Iron phosphate was produced using a spray-flame synthesis reactor with iron (III) acetylacetonate and tributyl phosphate dissolved in toluene as a precursor. The concentration of the precursor was varied from 0.0125 to 0.2 M while the other parameters such as precursor solution flow rate of 3 ml min^{-1} and pilot flame gas flow rate (2.4 l min^{-1} oxygen and 1.14 l min^{-1} CH_4) were kept constant. Table 3 shows the specific surface area measured by BET for both, as-prepared and calcined $FePO_4$ at different concentrations, and the crystallite size calculated from XRD measurement of calcined $FePO_4$ at different concentrations. Also, information concerning the particle size calculated from BET measurements (see Eq. 7) for both as-prepared and calcined is illustrated in Table 3.

Table 3: Specific surface area and particle size of as-prepared and calcined $FePO_4$ synthesized at various iron and phosphate concentrations

	As-prepared		Calcined at 600°C		
Sample	Specific surface area /m^2 g^{-1}	Particle size D_{BET} /nm	Specific surface area/m^2 g^{-1}	Particle size D_{BET} /nm	Crystallite size/nm
FP0.0125	218	12	80	25	30
FP0.05	173	14	57	36	42
FP0.20	126	16	50	40	46

A strong dependence of the specific surface area on precursor concentration can be seen in Table 3. The specific surface area of $FePO_4$ decreased sharply from 218 to 126 m^2 g^{-1} when a more highly concentrated precursor solution was applied. This is due to the higher concentration of nuclei that collide and coalesce resulting in bigger particles with a smaller surface area. After calcination at 600°C the surface area of $FePO_4$ also decreased sharply for all samples, and consequently the particle size increased up to the range of 25 to 40 nm with increasing precursor concentration. In all cases, the crystallite size (XRD) is slightly bigger than the particle size obtained from BET. Since the particle size calculated from BET is based on the assumption that the parti-

cles are spherical and monodisperse, this may lead to the observed slight difference between the BET analysis and XRD results. Further examination concerning the shape of the particles after heat-treatment at 600°C is shown by the TEM images later on.

According to the literature [111, 134, 200, 201], iron phosphate typically contains some water molecules per unit cell. Therefore, thermogravimetry measurements were conducted to determine the amount of water in the as-prepared $FePO_4$ samples and to determine the temperature required for the formation of the anhydrous salt. Figure 16 (a) shows the thermogravimetry measurement data of as-prepared $FePO_4 \cdot xH_2O$, measured from room temperature to 800°C in inert gas atmosphere with a heating rate of 10°C min^{-1}. A weight loss of about 17 wt% was observed which corresponds to the presence of 1.7 moles of water per mole of $FePO_4$. The measurements show that complete release of water requires a minimum temperature of about 600°C. This information is useful to anneal the as-prepared $FePO_4$ in order to crystallize its structure.

The XRD pattern of $FePO_4$ with different precursor concentrations is shown in Figure 16(b). All as-prepared $FePO_4$ samples produced from the spray-flame synthesis reactor are amorphous in structure and require further heat treatment at 600°C as determined from TG measurements. All the samples are well crystallized after annealing for 16 hours at 600°C with no impurities. Trigonal $FePO_4$ is well indexed with a = 5.058 Å and c = 11.254 Å while matching to the P 321 space group (ICDD 29-0715). This is analogous to the work conducted by Scrosati and co-workers [202]. Previously, Wang et al. [203], reported the same result of obtaining $FePO_4$ by annealing of $FePO_4 \cdot xH_2O$ at 600°C using precipitation and polymerization method. Okada et al. [201] describe amorphous iron phosphate synthesized by a modified solution route, that turn to highly crystalline trigonal structure after annealing at 650°C. It is worth mentioning that the diffraction pattern become sharper with increasing precursor concentration indicating bigger crystallites of $FePO_4$, see Table 3. This result is parallel with the particle size measurement data attained using BET measurements.

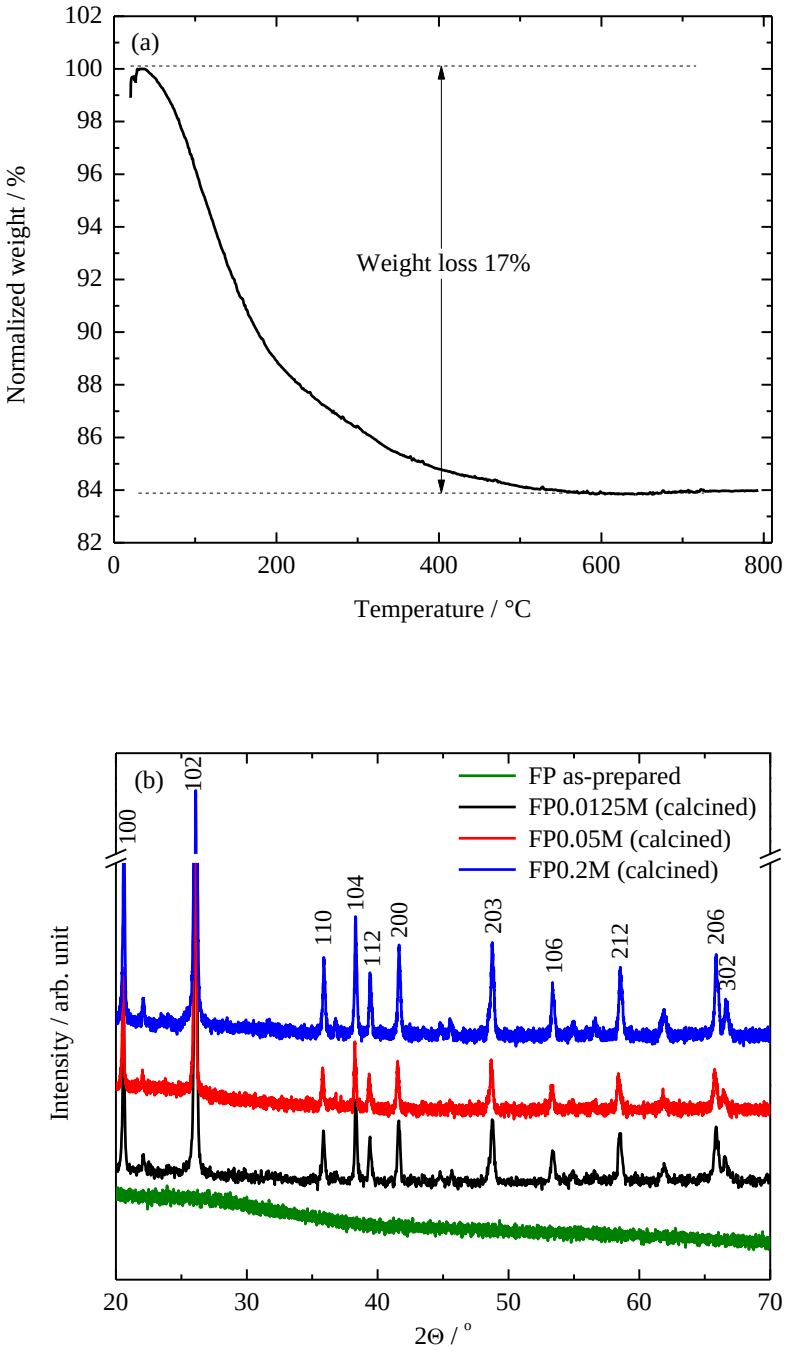

Figure 16: (a) Thermogravimetric measurement of amorphous, pristine $FePO_4 \cdot xH_2O$ and (b) XRD patterns of as-prepared and calcined (600°C) $FePO_4$ samples prepared at different precursor concentrations.

Figure 17 depicts the TEM images of as prepared (a) and annealed (b) $FePO_4$ prepared from a 0.2 M precursor concentration. As-prepared $FePO_4$ is composed of well spherical particles and soft agglomerates with an approximate size that is below 20 nm. Therefore, this result is consistent with the size obtained using BET measurements. Different phenomena are observed with the same sample after annealing at 600°C. The soft agglomerates lose their spherical shape and tend to necking each other which leads to bigger particles sizes as is demonstrated in Table 3. Judging from BET, XRD and TEM, it can be concluded that the precursor concentration has a great impact towards the physical properties (shape and size) of the resultant $FePO_4$. As a result, the desired size of $FePO_4$ can be easily acquired by altering the precursor concentration. This finding will be used later on to synthesize bigger $FePO_4$ particles by using higher precursor concentration.

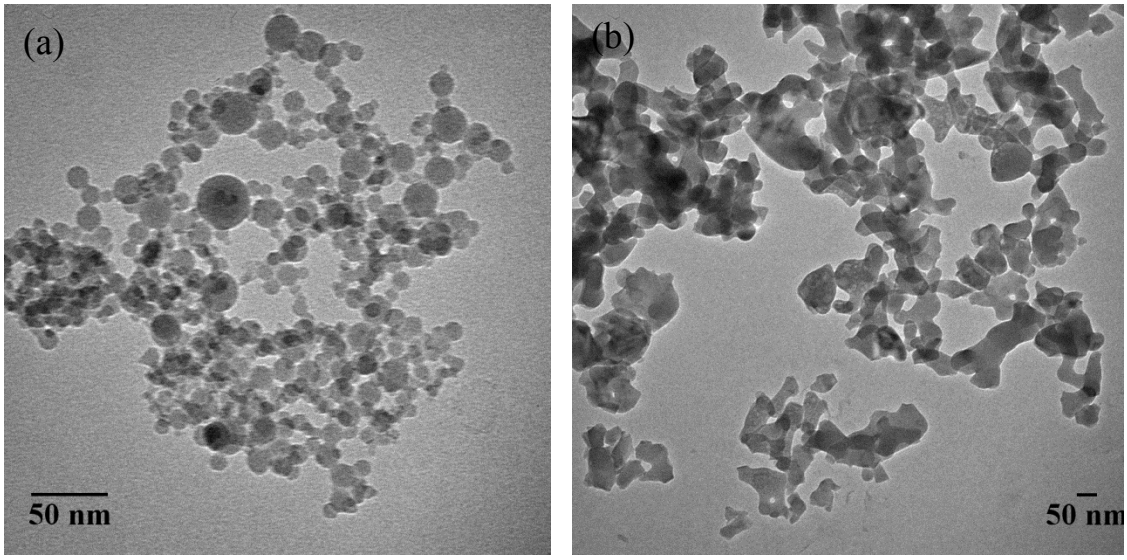

Figure 17: TEM images of $FePO_4$ from 0.2 M precursor solution as-prepared (a) and after annealing at 600°C (b)

As-prepared $FePO_4$ was used as a starting material to produce composite $LiFePO_4$/C with the aid of Li_2CO_3 (as Li source) and glucose as a carbon source and reducing agent. Glucose was used to reduce Fe^{3+} to Fe^{2+} as well as a carbon source for enhancing the electrical conductivity of $LiFePO_4$ [134, 204]. It is known from literature that subsistence production of carbon from the excess glucose helps to suppress the grain growth of $LiFePO_4$ during calcination [134], sustaining its nanostructure shape and properties [195]. Therefore, by addition of glucose to the precursor, the poor electronic conductivity of $LiFePO_4$ is successfully improved via existence of a car-

bon coating and nanosize of the particles. In the first attempt, 2 mol of as-prepared $FePO_4 \cdot xH_2O$ (0.2 M) was mixed thoroughly with 1 mol Li_2CO_3 (see Eq 5) and 16 wt% glucose using mortar and pure ethanol as a solvent before pre-heating at 80°C for 24 hours. The glucose content was chosen based on the calculation from Eq 5 and Eq 6 that calculates the amount of glucose required to reduce and coated $LiFePO_4$. Following complete crystallization of $FePO_4$ at 600°C, $LiFePO_4$ was further calcined at 600°C for 16 hours. Table 4 shows the physical properties of the first result of $LiFePO_4$/C (LFPC1).

Table 4: Specific surface area and particle size of nanocomposite LFPC1

Sample	Specific surface area /m^2 g^{-1}	Particle size D_{BET} / nm	Crystallite size D_{XRD} /nm	Carbon content /wt%
LFPC1	24	69	70	3.9

Nanocomposite $LiFePO_4$/C (LFPC1) was successfully produced using combined gas-phase and solid-state reaction with a particle/crystallite size of 69 and 70 nm calculated from BET and XRD measurement, respectively. From the elemental analysis, the carbon content is determined to be 3.9 wt%. Previously, Scrosati's group showed that the presence of carbon drastically enhanced the electrochemical performance of template-prepared nanocomposite $LiFePO_4$/C by providing 36% of its theoretical capacity at extremely high C-rate (65 C) [100]. It is expected that carbon increase would also improve the electrochemical behavior of the cathode made of this material. Further examination of the physical and chemical properties of nanocomposite $LiFePO_4$/C was conducted using XRD, TEM, XPS and Raman and the results are discussed later.

From the XRD measurements (Figure 18), it is evident that the resultant LFPC1 is composed of no other impurities that could be detected by the X-Ray diffraction. Highly crystalline olivine $LiFePO_4$/C was received after calcination at 600°C and the crystal structure was found to match well with the orthorhombic system of Pnma space group with lattice parameter of a = 10.333, b = 6.012, and c = 4.697 Å. Previously, the group of Yang et al. [205] reported a similar observation for $LiFePO_4$/C that was prepared using the polymer-pyrolysis reduction method. Kwon et al. [142] also reported impurity free $LiFePO_4$/C that was prepared using me-

chanical alloying technique of $LiOH{\cdot}H_2O$, $FeC_2O_4{\cdot}2H_2O$ and $(NH_4)2HPO_4$ powders which the particle sizes were smaller than 500 μm and calcined at 600°C. No peaks associated with carbon were found in the XRD pattern of our data which strongly indicates that carbon subsists in $LiFePO_4$/C in the amorphous form as can be expected due to the low annealing temperature of 600°C.

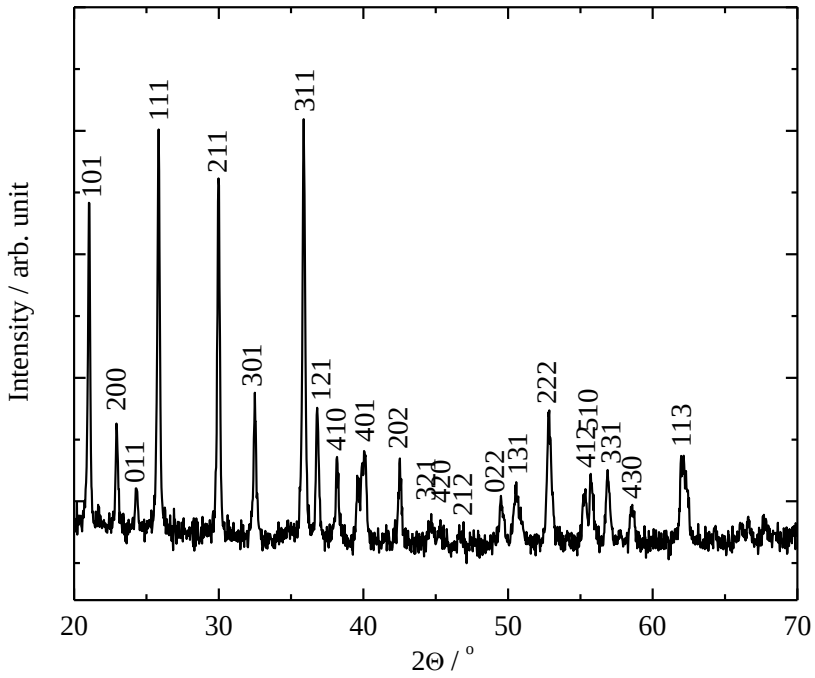

Figure 18: X-ray diffraction pattern of LFPC1 synthesized at 600°C

In order to clarify the type of carbon species in LFPC1, Raman spectroscopy measurement was conducted and the result is shown in Figure 19. There are two main broad peaks related to the sp^3 and sp^2 type at 1350 cm^{-1} and 1590 cm^{-1}, correspondingly. Particularly, the carbon peak assigned with sp^3 and sp^2 is known as disordered carbon (D-band) and graphite-like (G-band) carbon [206]. Thus, it is confirmed that carbon coated $LiFePO_4$/C mostly consists of disordered carbon.

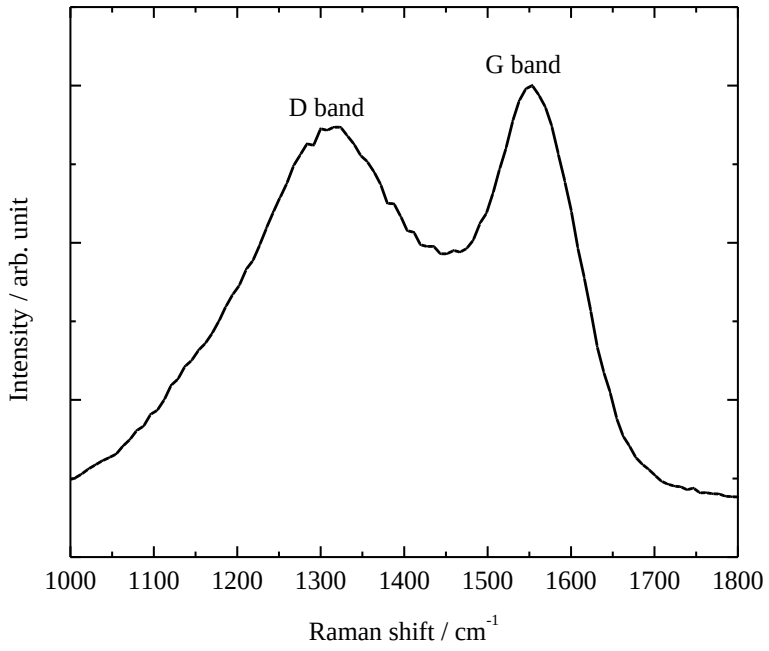

Figure 19: Raman spectrum of residual carbon in LFPC1

Despite detailed examination of the carbon structure of nanocomposite $LiFePO_4$/C, further investigation of oxidation state of iron species was conducted using X-ray photoelectron spectroscopy, Figure 20 illustrates the respective XPS spectrum. All the peaks of lithium, iron, phosphorus, oxygen, and carbon were identified and no other elements were detected. This proves again that this method is able to produce high purity $LiFePO_4$/C. The binding energy (BE) for Li1s, P2p, C1s and O1s was found to be 56, 134, 287, and 532 eV, respectively in agreement with literature [203] and [160]. The inset shows the enlarged spectrum around 720 eV indicating $Fe2p_{3/2}$ and $Fe2p_{1/2}$ with binding energies of 725 and 712 eV, correspondingly. Dedryvère et al. [207] explained that the Fe 2p peak is composed of two parts known as $Fe2p_{3/2}$ and $Fe2p_{1/2}$ as a result of spin-orbit coupling. The binding energy of these two parts resembles the oxidation state of iron species which can be attributed to Fe^{2+} when $Fe2p_{3/2}$ and $Fe2p_{1/2}$ are located at 710.5 and 723 eV, respectively, while $Fe2p_{3/2}$ and $Fe2p_{1/2}$ occurring at 712.5 and 726 eV correspondingly indicate a valence state of Fe^{3+} instead. As the penetration depth of XPS is only a few nm, it can be concluded from Figure 20 that Fe^{3+} is dominating the surface of $LiFePO_4$/C, most probably due to (short) exposure during handling and storage under ambient conditions leading to surface

oxidation of Fe^{2+} to Fe^{3+}. However, the XRD measurements give no indication for a substantial oxidation of the sample.

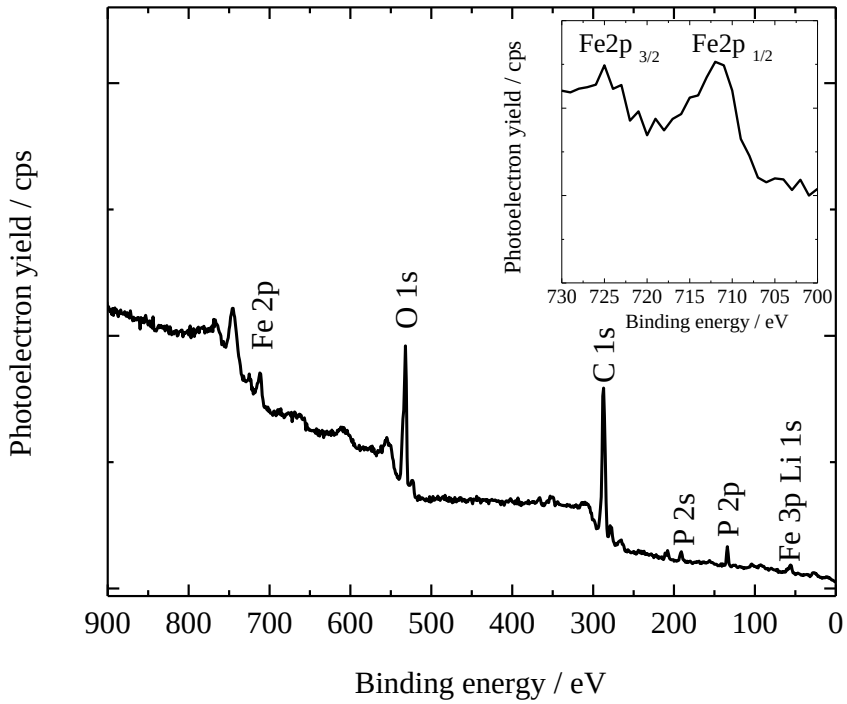

Figure 20: XPS spectrum of LFPC1

Figure 21 (a) shows the SEM image of $LiFePO_4$/C at higher magnification after calcination at 600°C. It clearly displays that $LiFePO_4$/C is composed of spherical particles with a primary particle size that is estimated to be around 60 nm, see also Table 4. However, it is also observed that the particles are partly sintered together leading to an increase in the particle size, up to about 100–150 nm.

An example result of deeper investigations concerning the carbon coating of the active material $LiFePO_4$, performed via TEM measurements, is displayed in Figure 21 (b). Nano $LiFePO_4$ is embedded within an amorphous carbon network.

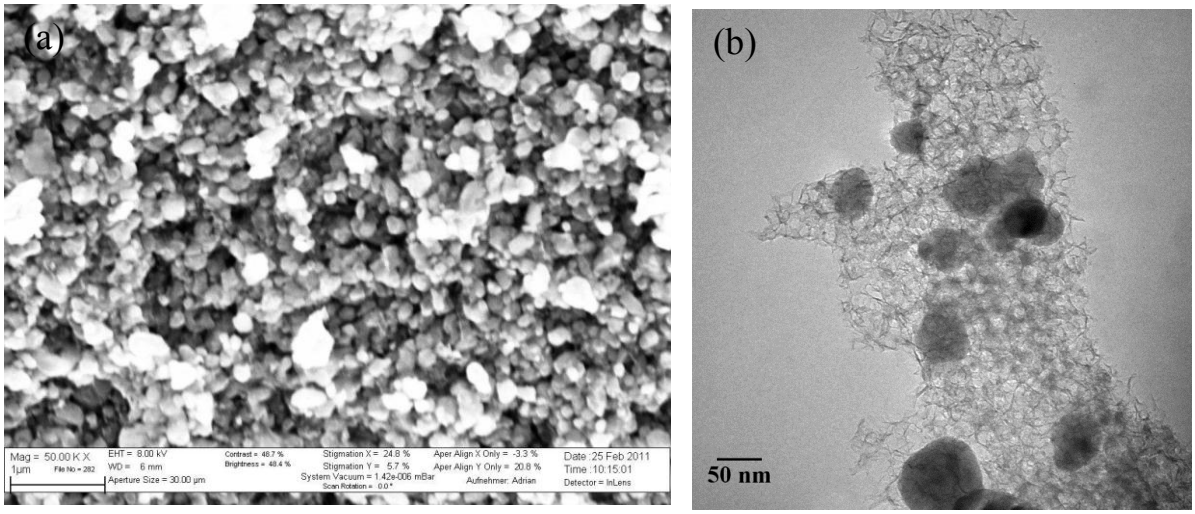

Figure 21: SEM (a) and (b) TEM images of LFPC1

As nanocomposite $LiFePO_4$/C was successfully produced using gas phase and solid-state reactions with no impurities, thus further examination regarding the electrochemical behavior was conducted and the details are presented in the following section.

4.1.2 Electrochemical characterization of nanocomposite $LiFePO_4/C$

The electrochemical measurements described in this thesis were conducted in collaboration with Sebastian Wennig from ZBT. In the first attempt, $LiFePO_4$/C and Super-P Li™ (Timcal) were intensely mixed in a mortar and subsequently dispersed in *N*-methyl-*2*-pyrrolidone (NMP, Acros Organics, extra dry, water < 50 ppm) together with polyvinylidene fluoride (PVdF, Solef 1013, Solvay Solexis). After sonication, the dispersions were further sonicated by 60 minutes. The slurry obtained was cast on an aluminum foil (Alujet, thickness 30 µm) with a wet film thickness of 150 µm by using an adjustable doctor blade and dried under vacuum at 120°C. The samples were then compressed by calendaring and cut into round electrodes with an area of 1.1 cm^2. The typical composition of the dried electrodes was 86 wt% $LiFePO_4$/C, 7 wt% Super-P Li™ and 7 wt% PVdF. The average mass loading of the electrodes was around 4.0 mg cm^{-2}.

In this section, electrochemical characteristics of LFPC1 will be explained. It is worth to mention that the amount of active materials ($LiFePO_4$/C) used in this study is by far higher with 86% of electrode composition than those described in the literature. Nevertheless, the electrode produced in this work possessed good mechanical stability. Electrochemical properties were investigated using Swagelok-type cells with lithium foil as a counter and reference electrode. Figure 22 shows the cyclic voltammogram of $LiFePO_4$/C electrode. As it is clearly illustrated, there are two peaks that are attributed to the oxidation and reduction process that occur at 3.5 V vs Li/Li^+, which is in good agreement with the redox peaks of $LiFePO_4$/C [106, 110, 162, 199]. During the first cycle, a broad peak for oxidation is observed as expected due to initial restructuring of the material during charging. This consequently decelerates the movement of Li^+ ions upon the lithiation process. A symmetric peak of oxidation and reduction appears afterwards (see inset, cycle 2 and 3) indicating that the electrochemical process is reversible and there is a rapid extraction and insertion of Li^+ ions during charging and discharging of $LiFePO_4$/C.

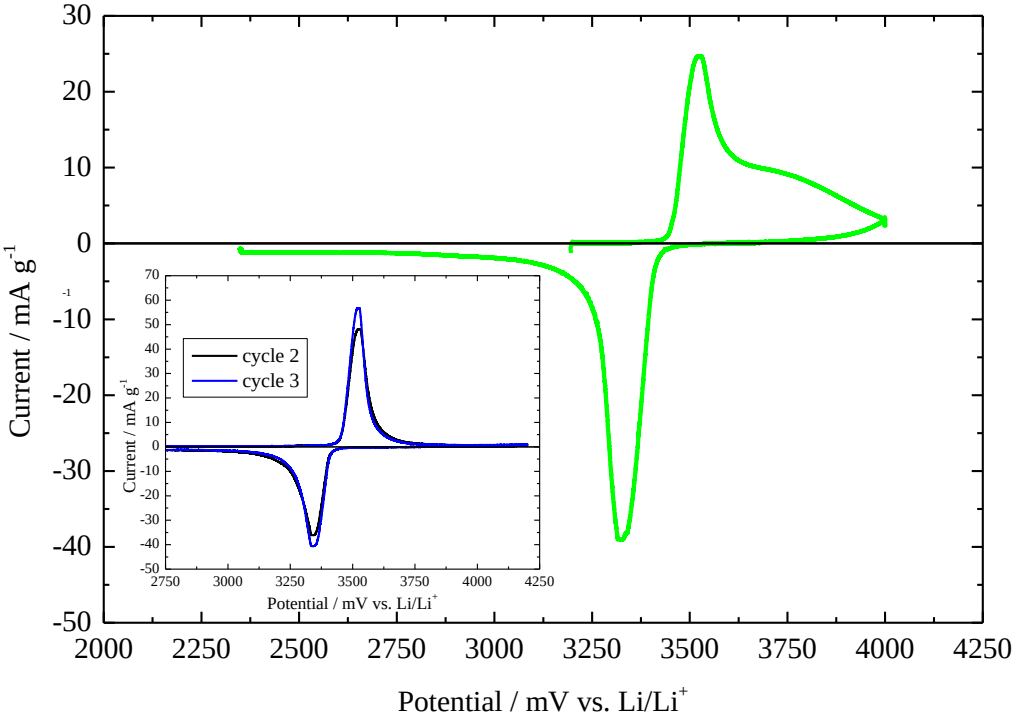

Figure 22: Cyclic voltammetry of LFPC1 at a scan rate of 0.01 mV s^{-1}

Figure 23 shows the discharge curve of nanocomposite $LiFePO_4$/C at 0.05 C. A flat plateau at 3.4 V vs. Li/Li^+ was observed habitually denoting a single phase transition process of $FePO_4$ to $LiFePO_4$. As can be seen, the discharge capacity has a value of 142 mAh g^{-1}. This value is below (by 16%) the theoretical value for $LiFePO_4$ which is 170 mAh g^{-1}. Usually, a cut-off potential of 4.2 to 4.5 V is applied for $LiFePO_4$/C [184, 208] in order to fully delithiate iron phosphate. Since a large surface area of nanocomposite $LiFePO_4$/C is obtained, discharging at higher potentials will probably lead to unwanted side reactions with the electrolyte. Therefore, a lower cut-off potential (4 V) was applied in this work contributing to slightly reduced capacity even at low current rates. However, the capacity attained from $LiFePO_4$/C this work of 117 mAh g^{-1} is approximately close to the value found in the literature (120 mAh g^{-1}) by taking into account a higher mass loading and discharge at a potential lower than the normal cut-off voltage [42, 209, 210].

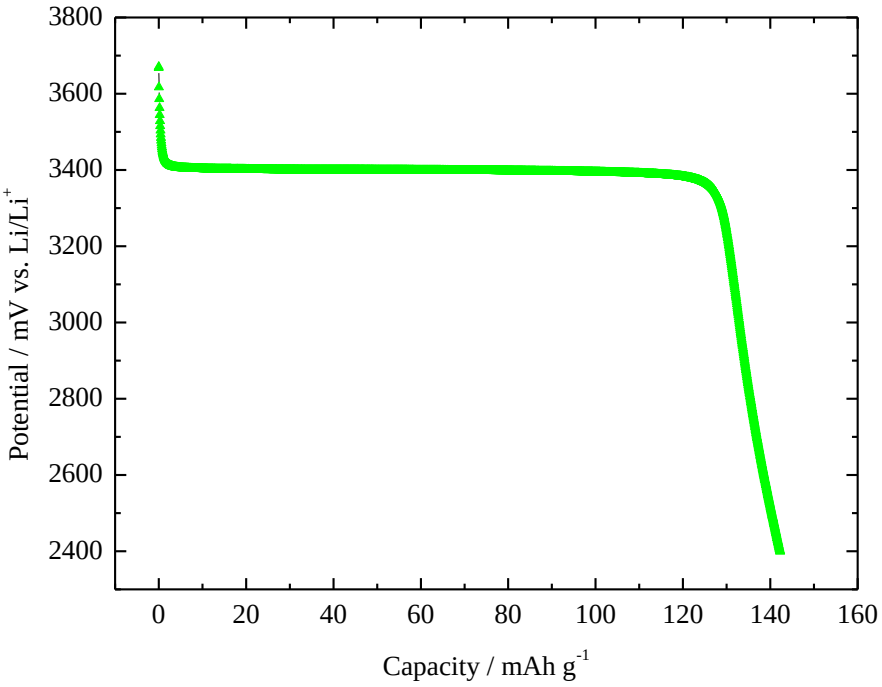

Figure 23: Initial discharge curve at 0.05 C for LFPC1 electrodes.

Figure 24 depicts the discharge curve at different current rates ranging from 0.05 to 16 C. A discharge capacity of 143 mAh g^{-1} was recorded at 0.05 C while the capacity decreased gradually to 40 mAh g^{-1} with increased discharge current of up to 16 C. This behavior is closely related to limited diffusion rates of Li^+ ions and electrons in olivine structure which in the end raises the polarization to a greater value. In addition to that, limited diffusion of electrolyte at higher current rate (i.e., 16 C) may also occur. Considering the overall coating mass used, the capacity at 16 C (40 mAh g^{-1}) is surprisingly higher, by 20%, than the capacity yielded at the very high C-rates previously reported by Waser et al. [159] who produced nanocomposite $LiFePO_4$/C using two step flame spray pyrolysis.

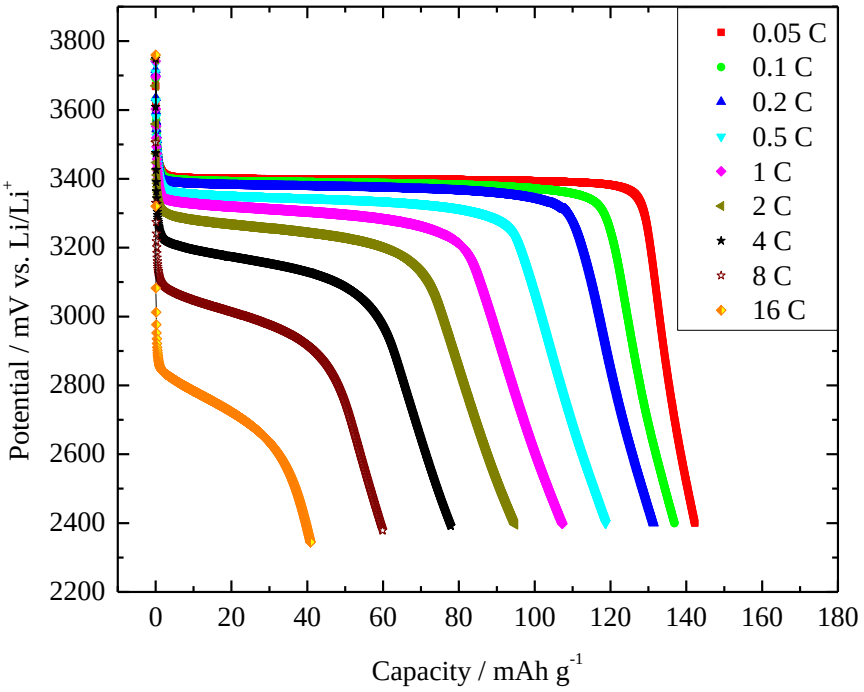

Figure 24: Discharge curve of LFPC1 at various C-rates

Figure 25 shows the rate retention profiles or galvanostatic cycling of nanocomposite $LiFePO_4$/C at various C-rates ranging from 0.05 C to 16 C to study the capability of nanosized $LiFePO_4$/C under different environments of current rate during discharging. The recorded values show that $LiFePO_4$/C is capable of withstanding high C rates by providing 40 mAh g^{-1} at 16 C. Remarkably, the nanosized $LiFePO_4$/C produced an slightly higher discharge capacity after cycling back from 16 C to the initial C rate of 0.01 C. This result proves that the nanocomposite $LiFePO_4$/C produced by combining gas-phase and solid-state reactions is very stable upon discharging at various current rates. This implies that the electrode made from this material is highly stable and competent to be used in the commercial lithium ion battery market as it offers a lightweight compared to the electrodes fabricated with higher amounts of carbon [159].

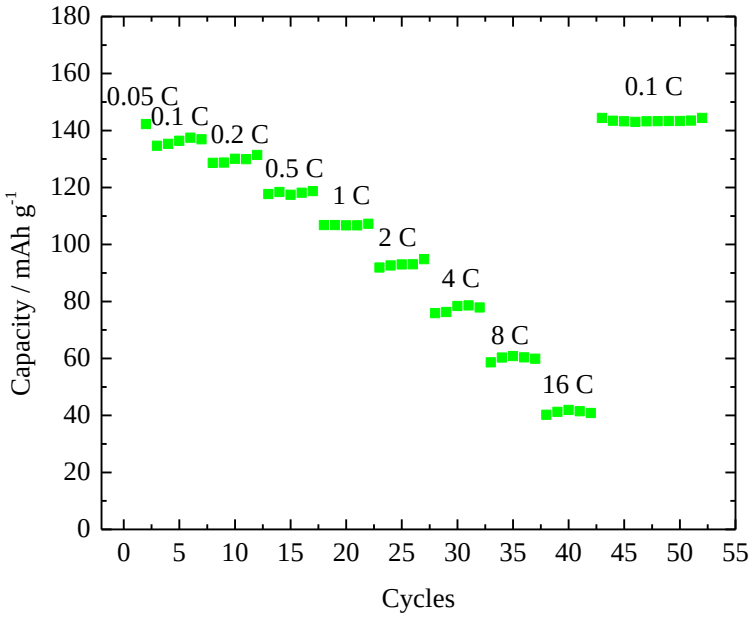

Figure 25: Rate retention performance of $LiFePO_4$/C at various C rates

4.2 Influence of calcination temperature and carbon content on the properties of nanocomposite $LiFePO_4/C$

After successful fabrication with promising electrochemical properties of $LiFePO_4$/C (LFPC1) described before, the second part of this work is related to investigations for the enhancement of electrochemical performances by modification of synthesis condition. In detail, calcination temperature of $LiFePO_4$/C and carbon content is investigated and results will be discussed in the next subsections. It is expected that the electrochemical performance of $LiFePO_4$/C can be enhanced based on optimized calcination temperature and carbon content during synthesizing step.

4.2.1 Characterization of $FePO_4$ and nanocomposite $LiFePO_4/C$

As known from literature, a mean $LiFePO_4$ particle size of about 50 to100 nm seems to be a reasonable compromise between diffusion length (which is directly related to the particle size) and almost unstable and oxidation sensitive high surface area. The investigations concerning concentration-dependent particle size in chapter 4.1.1 have shown that even the highest precursor concentration leads to particle sizes well below 100 nm. As a result, the precursor concentration was further increased to a maximum value with respect to their solubility in toluene. Therefore, nanosized $FePO_4$ with a precursor concentration of 0.35 mol l^{-1} was produced to synthesize $FePO_4$ at a production rate of 5 g h^{-1} using the spray-flame synthesis method described before. As-prepared $FePO_4.xH_2O$ subjected to TG measurement showed the same result with respect to water concentration as the $FePO_4.xH_2O$ from 0.2 M solution. As-prepared and calcined $LiFePO_4$/C were characterized using BET and XRD, results are shown in Table 5. The particle size from BET is calculated from Eq 7 while the crystallite size was obtained from XRD result. As expected, the particle size can be further increased compared to the materials synthesized before, see Table 3 for comparison.

Table 5: Physical properties of as-prepared and calcined $FePO_4$ synthesized from 0.35 M solution

Sample	As-prepared		Calcined at 600°C		
	Specific surface area /$m^2\,g^{-1}$	Particle size D_{BET} /nm	Specific surface area/$m^2\,g^{-1}$	Particle size D_{BET} /nm	Crystallite size D_{XRD} /nm
FP0.35	104	19	42	47	54

In coincidence with the results received for $FePO_4$ synthesized from lower precursor concentration, the typical structure of $FePO_4$ could be identified after annealing, see Figure 26 and Figure 16 (b).

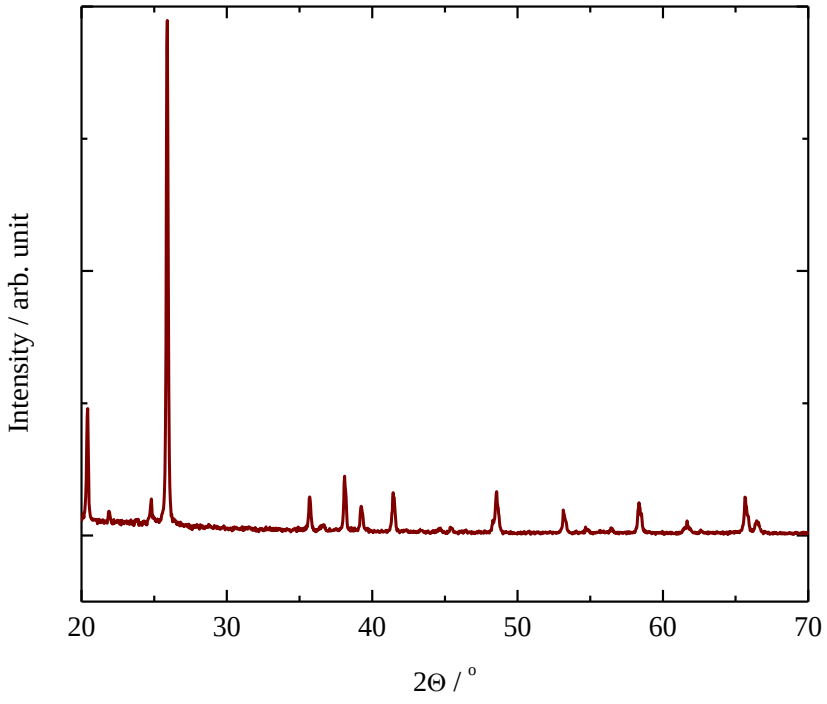

Figure 26: X-ray diffraction pattern of $FePO_4$ synthesized from 0.35 M solution

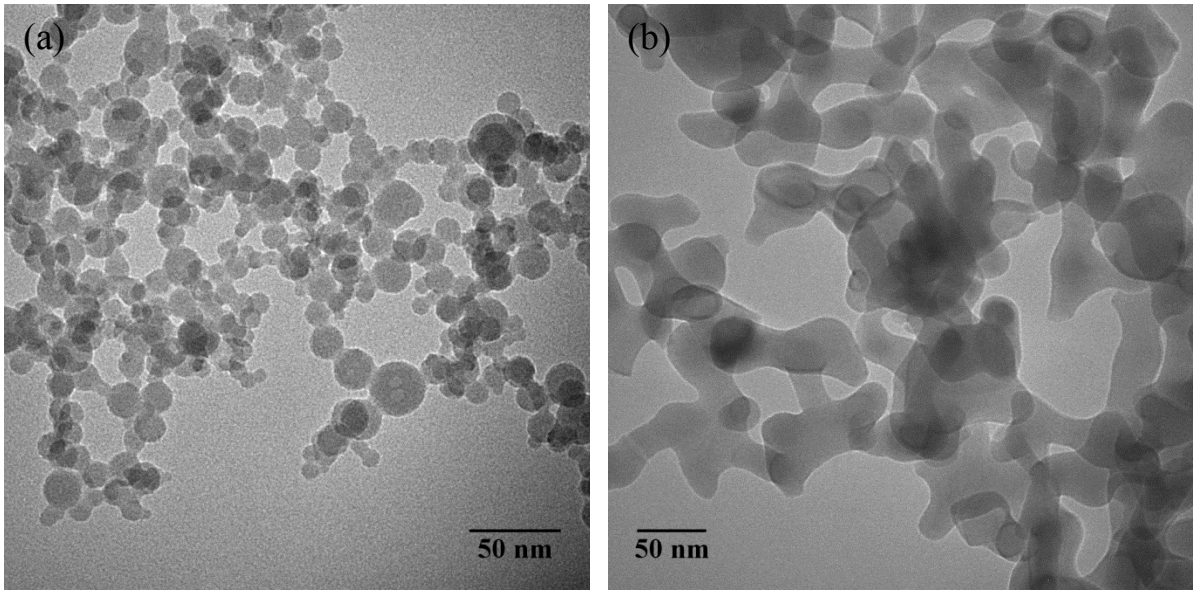

Figure 27: TEM images of $FePO_4$ from 0.35 M precursor solution of as-prepared (a) and after annealing at 600°C (b)

Figure 27 shows the TEM images of $FePO_4$ from 0.35 M solution before and after annealing at 600°C. The morphologies of the particles are quite similar to those observed for particles from 0.2 M concentration (see Figure 17). It signifies that the concentration only affected the size but not the morphology of the resultant particles.

Earlier findings demonstrated that electrochemical properties of $LiFePO_4$/C are strongly influenced by the amount of carbon content and coating thickness [29, 35-37, 39], which solely rely upon synthesis procedure. Therefore, it is an important objective to identify appropriate conditions for well-suited materials with respect to particle size, conductivity and (minimum) carbon loading to ensure a high content of electrochemically active material in the electrodes.

Literature review of $LiFePO_4$/C solid state synthesis clearly showed that milling of the precursor prior to solid-state reaction results in a significant increase in discharge capacity of $LiFePO_4$/C due to intimate and homogeneous mixing, and milling for 12 hours was identified as a proper mixing time [128, 155]. Therefore, all solid precusors ($FePO_4 \cdot xH_2O$, Li_2CO_3, and glucose) were milled for 12 hours prior to calcination.

Systematic investigations were carried out with respect to calcination temperature and carbon content. Thus, as the first step, a series of $LiFePO_4$/C with 20 wt% of glucose as carbon source were calcined at different temperature between 600 and 800°C. The results gained from

BET and CHNS measurements are summarized in Figure 28. The particle tends to grow whenever higher temperature applied, thus lowering the specific surface area of $LiFePO_4$/C which is in accordance with literature data of Mi et al. [197] and Yang et al. [156]. Parallel to this result, it is worth to mention that the same pattern was observed for the residual carbon content. However, significant decreases in carbon content are observed from 700°C and above, see also [156, 204].

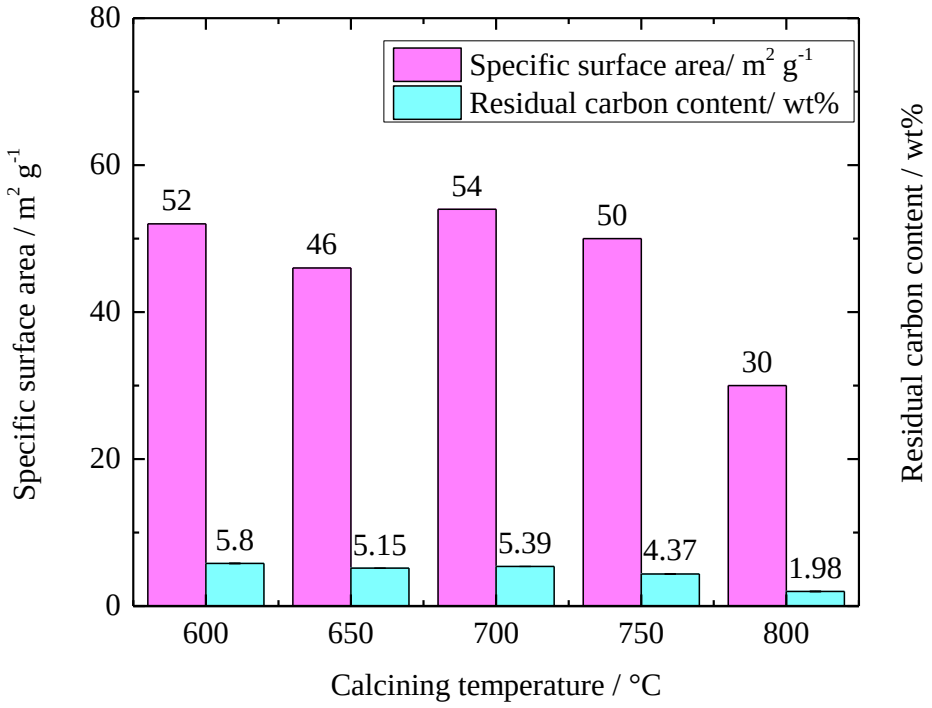

Figure 28: Correlation between calcining temperature with specific surface area (m^2 g^{-1}) and residual carbon content (wt%) of nanocomposite $LiFePO_4$/C

Further investigation regarding the crystal structure of the different $LiFePO_4$/C samples was conducted by X-ray diffraction and the results are shown in Figure 29. For each sample, the peaks match well with the orthorhombic structure of triphylite $LiFePO_4$ with space group of Pnma. Nevertheless, impurities related to conducting phase, Fe_2P were increasingly visible after calcination at 700 to 800°C (stars), and FeP was identified within the samples calcined at lower temperature of 600–650°C (open circles). The conducting phase of iron phosphide, Fe_2P is understood to promote the electrical conductivity of $LiFePO_4$/C thus directly enhancing the electrochemical properties of this material. Several groups found that coexistence of iron phosphide

helps to provide high discharge capacity and stable rate-retention of $LiFePO_4$/C at elevated current rate [36, 211-213]. The analysis of the XRD measurements reveals that the crystal size of $LiFePO_4$/C at 600, 650, 700, 750, and 800°C is calculated as 34, 35, 31, 34, and 48 nm, respectively. These values match well with the results acquired from BET measurements.

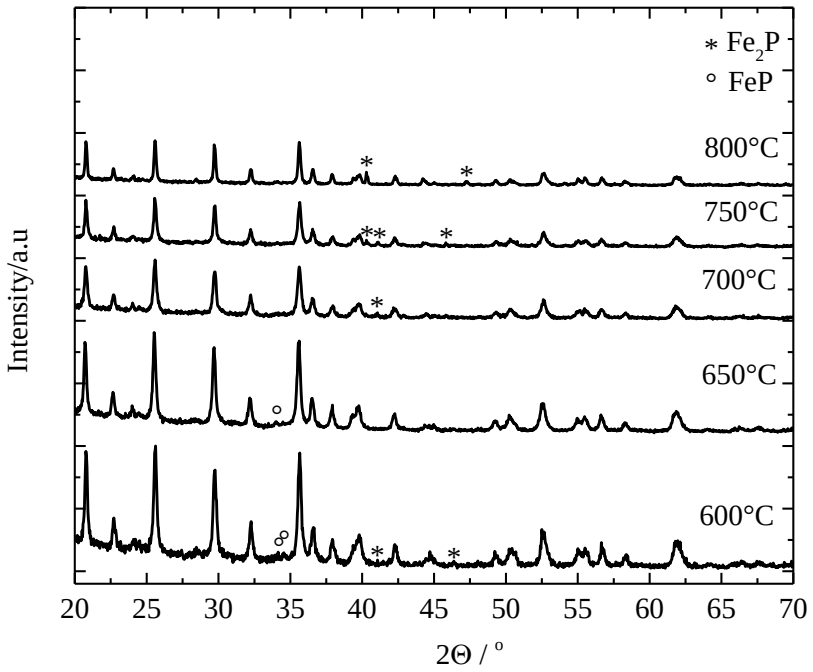

Figure 29: X-Ray Diffraction pattern for nanocomposite $LiFePO_4$/C synthesized at different calcination temperature

Figure 30 (a–b) shows typical transmission electron microscopy images of nanocomposite $LiFePO_4$/C with a carbon content of 7.3 wt% at low and high magnification, respectively, TEM images of the other samples look similar. At low magnification it can be seen that the $LiFePO_4$ particles form small aggregates homogenously surrounded by a coating layer. There is a significant difference between $LiFePO_4$/C with 7.3 wt% C Figure 30 (a) and LFPC1 described earlier (see Figure 21), as the latter exhibits a porous carbon web while the new samples show a homogeneous carbon layer with a certain thickness. The main reason is that LFPC1 was produced via mechanical mixing of the solid reactants in a mortar before calcination while the present materials were milled for 12 hours prior to calcination. Therefore, the present samples were prepared from a very homogeneous mixture while the reaction mixture used to synthesize

LFPC1 is expected to consist of a mixture with much bigger inhomogeneities and high local carbon content leading to the porous carbon network. From Figure 30 (b), a carbon layer surrounding the active material with a thickness around 2–3 nm is observed. This value is in very good agreement with the value of 2.9 nm that can be calculated using mean particle size obtained by BET and the measured carbon content. This is somewhat higher than the value proposed by Dominko et al. [45] who suggest that the optimum carbon thickness is ideally around 1–2 nm. However, carbon thickness in this work ($LiFePO_4$/C with 7.3 wt% C) is slightly more than the optimum value.

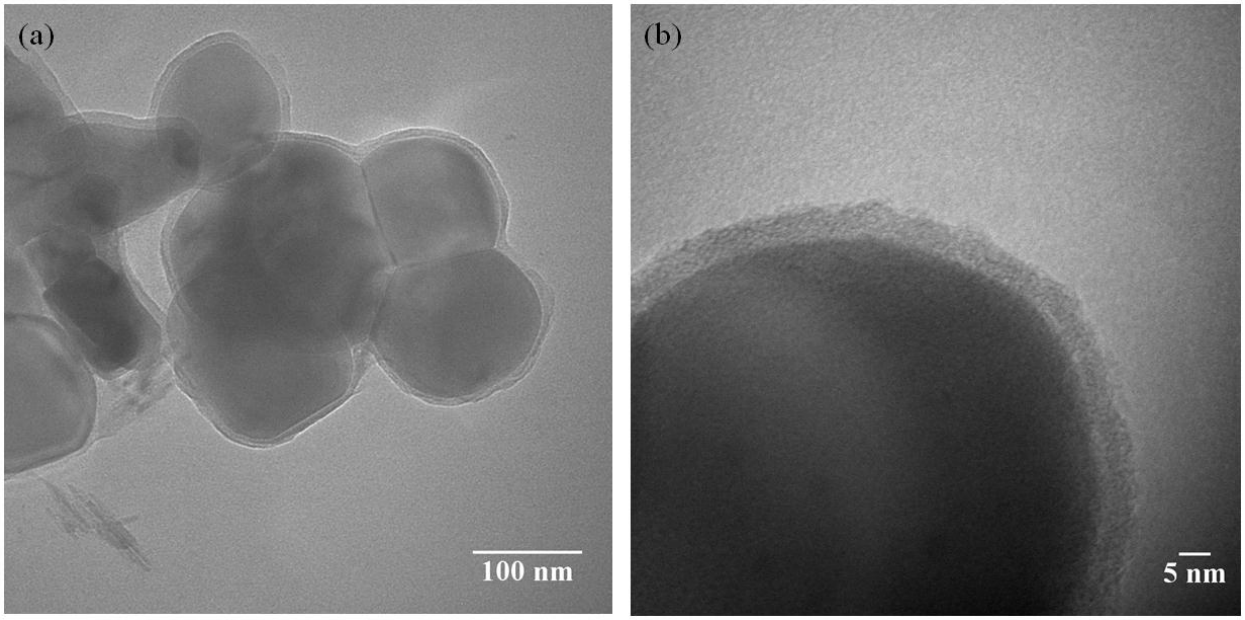

Figure 30: TEM images of $LiFePO_4$/C with 7.3 wt% residual carbon content at lower (a) and higher (b) magnification

Examination of the carbon structure surrounding the nanosized $LiFePO_4$/C calcined at different temperature was done with Raman spectroscopy as described above. Figure 31 shows the respective Raman spectra of $LiFePO_4$/C synthesized at different calcination temperatures. The quality of carbon coating can be determined by checking the intensity ratio between the D-band over the G-band (I_d/I_g). Lower ratios have been shown to result in a good quality of carbon coating and are useful for enhancing the conductivity of $LiFePO_4$/C and vice versa [36]. The results indicate that the samples do not show much difference, however, a slight tendency in intensity ratio towards higher I_d/I_g ratio with increasing temperature is observed.

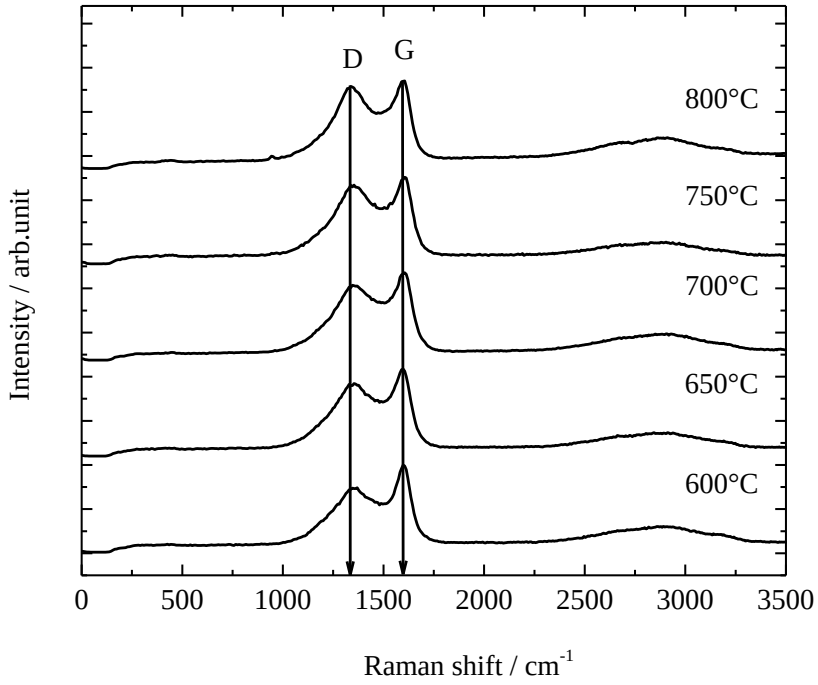

Figure 31: Raman spectra of nanocomposite $LiFePO_4$/C at different calcination temperature

Hence, XRD results as well as measurements of particle size and residual carbon content strengthen the finding that a calcination temperature of 700°C is preferred as this temperature holds a minimum crystal size and having insignificant amount of iron phosphide. Thus, all the samples prepared to investigate the influence of carbon content were calcined at 700°C.

It is known from literature that the addition of glucose and subsequent calcination has three major benefits (i) to restrain the growth of particles (ii) to reduce the oxidation state of iron from Fe^{3+} to Fe^{2+} and (iii) to increase the electronic conductivity significantly [21, 23, 199], However, it is detrimental to have huge carbon coating surrounding the active material $LiFePO_4$ as the pathway for Li^+ ions movement may be blocked with increasing coating thickness, thus degrading the performance of battery during intercalation and deintercalation whilst too less carbon will left the electronic conductivity of $LiFePO_4$/C unaltered. Thus, it is an important criterium to coat the nanosized $LiFePO_4$ with sufficient amount of carbon to provide good electronic conductivity but allowing fast passage of Li^+ ions during both, charging and discharging.

In order to achieve this mission, a series of experiments with varied amount of glucose were performed. All materials were milled for 12 hours and calcined at 700°C for 16 hours. Figure 32 illustrates how the increasing glucose content affects the particle size of resultant $LiFePO_4$/C based on BET measurements. It is expected that particle with the smallest particle size will shorten the diffusion length of Li^+ ions during cycling resulting in stable rate retention at immense discharge rate.

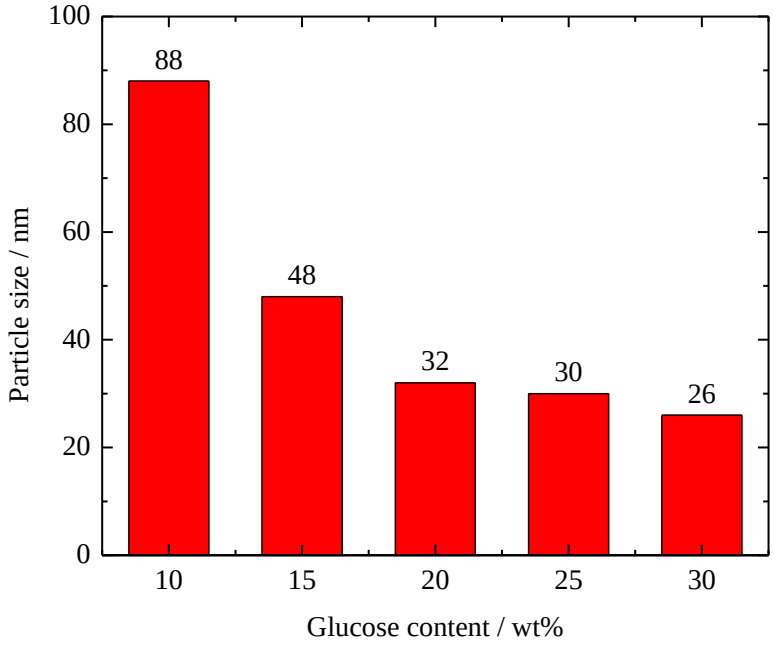

Figure 32: Physical properties of nanocomposite $LiFePO_4$/C at different glucose contents

From Figure 32 it is obvious that the particle size is significantly reduced with increasing glucose content. Figure 33 shows the correlation between glucose content, residual carbon content and electrical conductivity. It is found that the residual carbon content obtained from decomposition of glucose under inert atmosphere changes almost linearly with the initial glucose amount. This result was found to be in good agreement with previous finding [198] with respects to glucose as carbon source. Accordingly, the electrical conductivity steeply increases which would be beneficial for electrochemical properties. Bewlay et al. [157] also found that the electrical conductivity of $LiFePO_4$/C produced using spray synthesis route increased sharply with increasing amount of carbon content of up to 31 wt%.

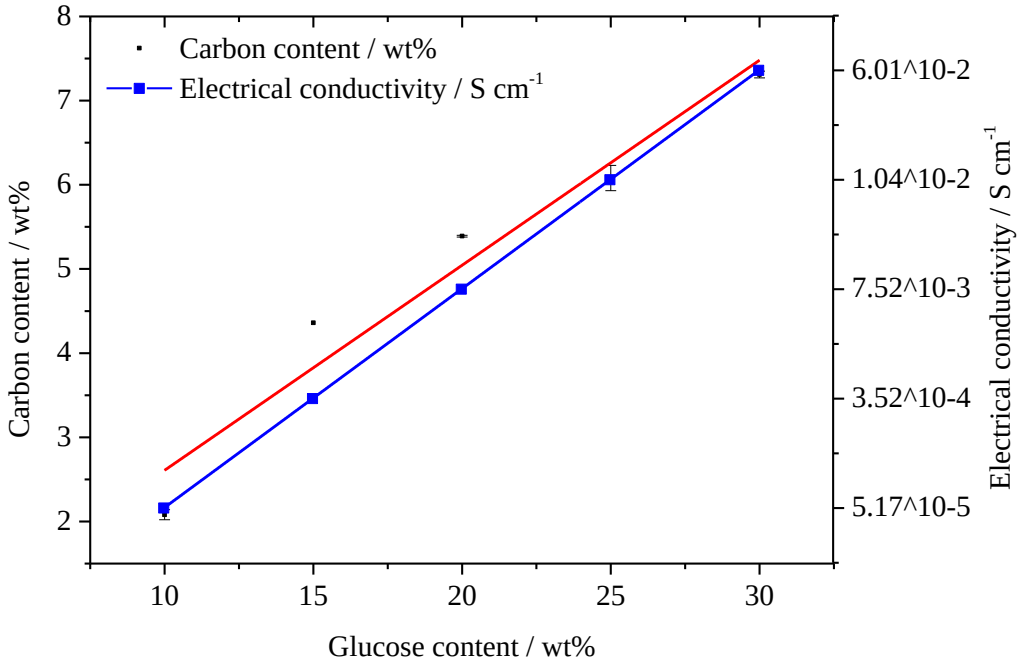

Figure 33: Relation of glucose content with residual carbon content for $LiFePO_4$/C after milled for 12 hours and calcined at 700°C for 16 hours

XRD measurements were accomplished to investigate the effect towards crystallinity, see Figure 34. Again, all the samples show the same, well-crystalline structure and can be indexed according to orthorhombic structure with space group of Pnma. Samples with 10 and 15 wt% of glucose reveal very little impurities related to FeP while samples with 20 to 30 wt% of glucose present high purity structure. In accordance with the BET measurements, the crystallinity of the samples which is directly related to the peak height decreases with higher amount of glucose. Consequently, it is expected that sample with lofted amount of glucose will have the smallest crystal size. In order to validate this assumption, crystallite size were calculated using XRD data and value is noted to be 40, 34, 31, 36, and 33 nm for glucose content of 10, 15, 20, 25, and 30 wt%, respectively. All the samples were then electrochemically characterized to testify the hypothesis mentioned earlier that higher amount of residual carbon would potentially enhance the electrochemical performance.

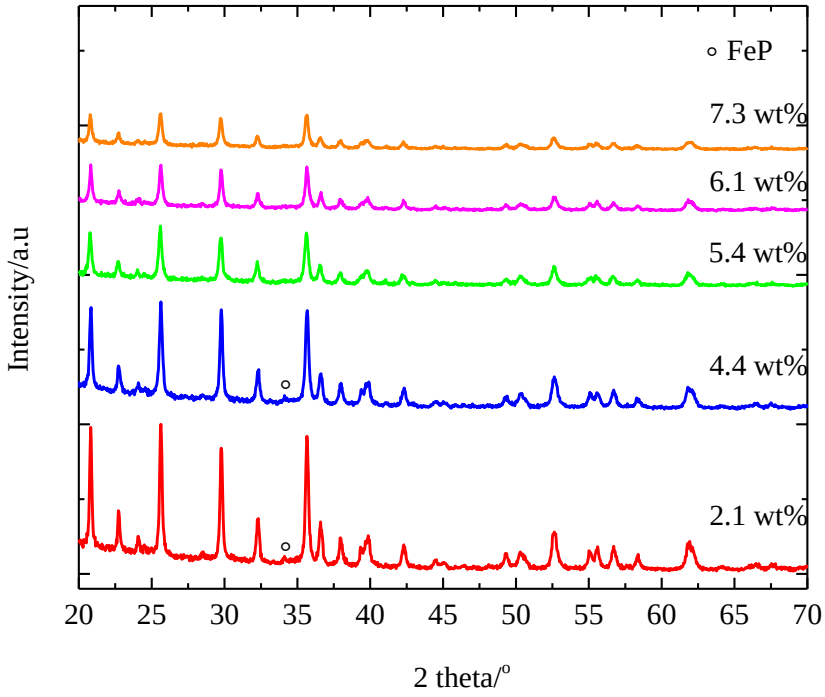

Figure 34: XRD pattern of $LiFePO_4$/C at different carbon content

The Raman spectra of the different samples are shown in Figure 35. There are again two prominent peaks showing that mainly graphitic and disordered carbon. As shown before, there is almost no difference in the Raman spectra, which can be expected from the fact that the annealing temperature was the same for all samples.

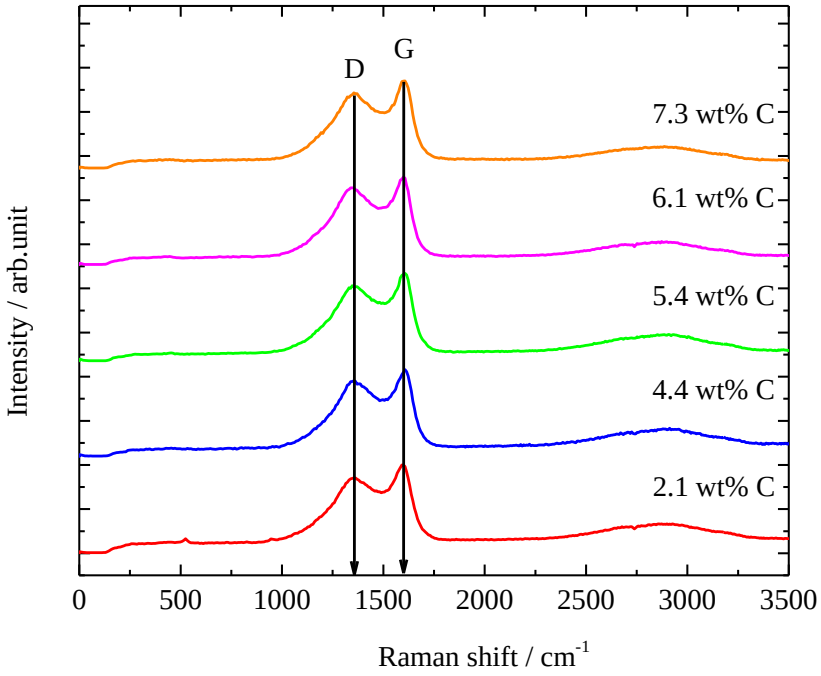

Figure 35: Raman spectra of LiFePO4/C measured at varied carbon contents

Another criterion that is important to be examined is the oxidation state of iron species as it is desired to have Fe^{2+} inside the nanocomposite $LiFePO_4$/C. Therefore, non-destructive XPS measurements were conducted for all samples. Besides investigating the degree of iron oxidation, XPS also allows for determination of the elements that exist in the samples. Figure 36a shows the XPS spectra of $LiFePO_4$/C at different amounts of carbon content. All the peaks corresponding to $LiFePO_4$/C were easily identified and could be assigned according to the binding energy of the elements. The binding energy (BE) for Li1s, P2p, C1s and O1s were found to be 56, 134, 287, and 532 eV, respectively. In the meantime, no other peaks are detected by this technique confirming the purity of the samples. In addition to that, Dedryvère et al. [207] explained that the Fe2p peak is composed of two parts known as $Fe2p_{3/2}$ and $Fe2p_{1/2}$ as a result of spin-orbit coupling. The binding energy of these two parts resembles the oxidation state of iron species which can be attributed to Fe^{2+} when $Fe2p_{3/2}$ and $Fe2p_{1/2}$ are located at 710.5 and 723 eV, respectively, while $Fe2p_{3/2}$ and $Fe2p_{1/2}$ occurring at 712.5 and 726 eV correspondingly indicate a valence state of Fe^{3+} instead. As the penetration depth of XPS is only a few nm, it can be concluded from Figure 36 (b) that Fe^{3+} is dominating the surface of $LiFePO_4$/C, most probably due

to (short) exposure during handling and storage under ambient conditions leading to surface oxidation of Fe^{2+} to Fe^{3+}. However, the XRD measurements give no indication for a substantial oxidation of the sample.

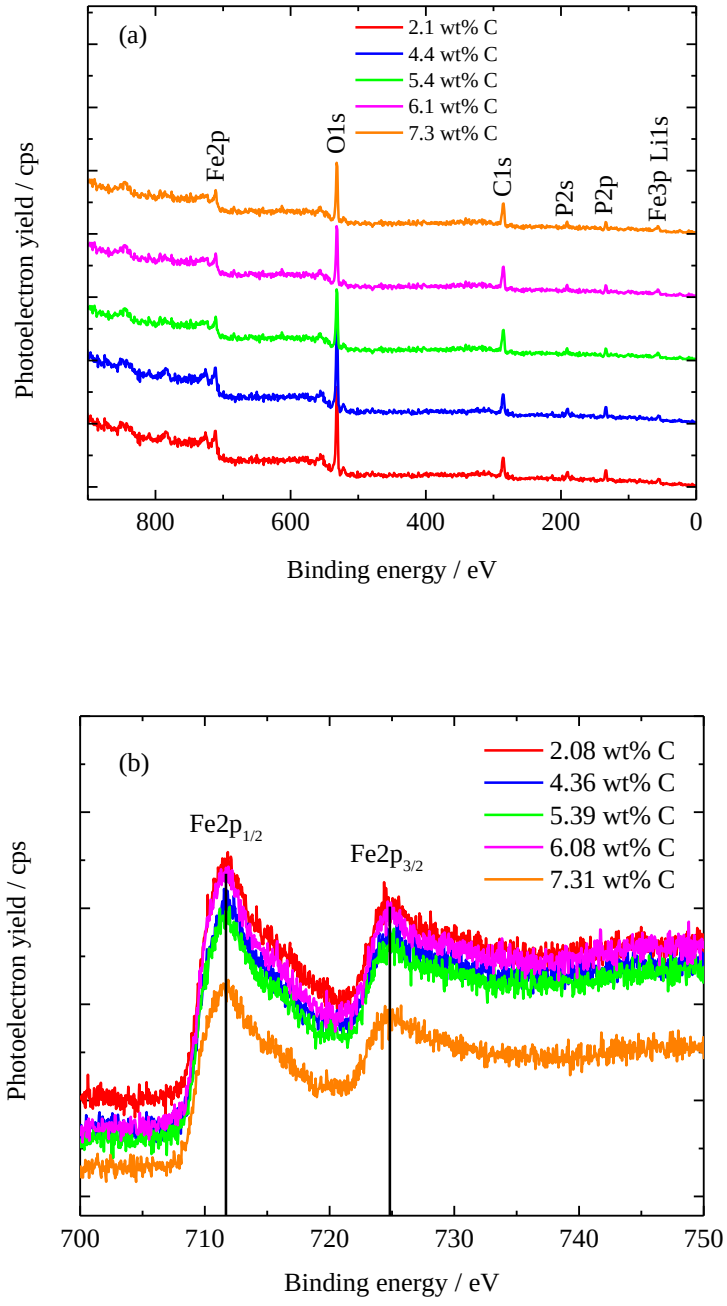

Figure 36: XPS pattern (a) and enlarged spectra (b) of $LiFePO_4/C$

As the results from XPS typically provide information from the surface but not from the bulk, an additional investigation concerning the valence state of iron was carried out using Mößbauer spectroscopy. Owing to its high sensitivity towards amorphous and nanoscale particles, this technique is profoundly useful to determine bulk properties of the kind of valence state of iron in particular. The Mößbauer spectrum of $FePO_4$ which was produced directly using spray-flame synthesis is shown in Figure 37, bottom graph. In the same figure, the Mößbauer spectra of the different nanocomposites are also shown.

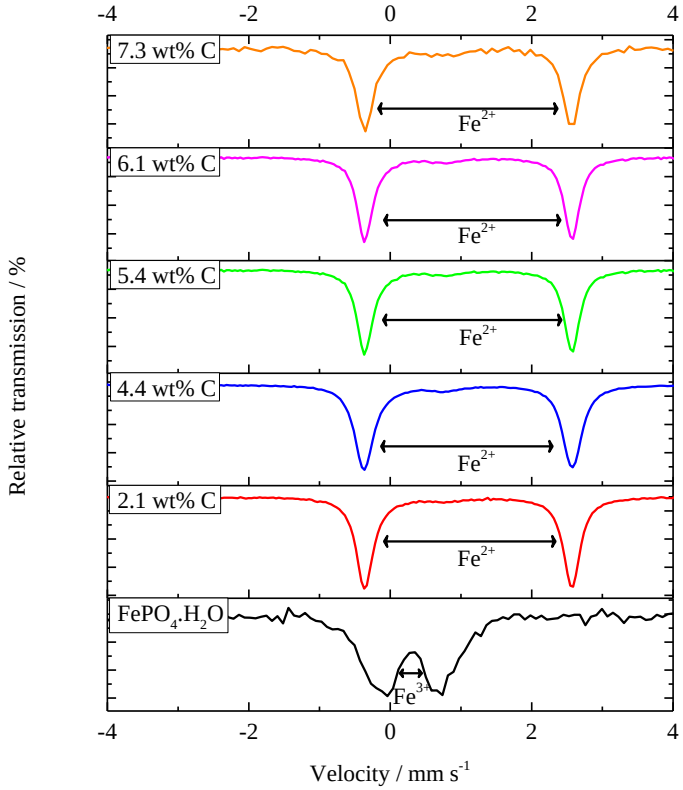

Figure 37: Mößbauer spectra of as-prepared $FePO_4$ and the different $LiFePO_4$/C samples

Amorphous $FePO_4$ shows one symmetric doublet with an isomer shift (IS) value of 0.39 and 0.37 mm s^{-1} with relative areas of 62 and 38%, respectively. This value clearly indicates that amorphous $FePO_4$ solely consists of Fe^{3+}, that is in agreement with the value found in the literature [200]. From the measurements on $LiFePO_4$/C it can be seen that all samples show mainly one symmetric doublet and one very weak signal with IS values of 0.43–0.45 mm s^{-1} which belong to the Fe^{3+} impurities regardless of the amount of residual carbon. The symmetry doublet,

having a dominant IS value of 1.21 mm s^{-1}, is typically observed for octahedral coordinated Fe^{2+} in $LiFePO_4$ [115, 214, 215]. The relative area of the doublet which resembled Fe^{2+} for each sample with a carbon content of 2.08, 4.38, 5.36, 6.08, and 7.31 wt% was calculated to be 94, 93, 93, 92, and 90%, respectively, indicating a slight decrease in Fe^{2+} content with increasing amount of carbon. As a result it can be stated that all nanocomposite $LiFePO_4$/C samples mainly contain Fe^{2+} with a few traces of Fe^{3+} located at the particle surface, most probably due to handling of the materials under inert conditions.

4.2.2 Electrochemical characterization of $LiFePO_4$/C with varied carbon content

In contrast to the electrochemical experiments shown before. $LiFePO_4$/C electrodes were fabricated using a binder system composed of polyacryrilic acid (PAA) as intermediate investigations of Sebastian Wennig have shown that this binder system works better than the PVdF used before. Super-P Li™ (Timcal) were intensely mixed in a mortar and subsequently dispersed with sonication and a turbo mixer at 10,000 rpm in a solution composed of ethanol (VWR BDH Prolabo®, AnalaR Normapur, absolute) and water (Sartorius Stedim Biotech arium® 611 UV) together with polyacrylic acid (PAA, Alfa Aesar®, 25 wt% solution in water, average molar weight 240,000 g mol^{-1}). The slurry obtained was cast on an aluminum foil (Alujet, thickness: 30 µm) with a wet film thickness of 100 µm by using an adjustable doctor blade and dried under vacuum at 90°C. The samples were subsequently cut into round electrodes with an area of 1.1 cm^2. The typical composition of the dried electrodes was 88 wt.% $LiFePO_4$/C, 7 wt.% Super-P Li™ and 5 wt.% PAA.

Electrochemical measurements were carried out using Swagelok-type electrode cells. Lithium foil (Chemetall, 100 µm thick) served as counter and reference electrodes and polypropylene fleeces impregnated with electrolyte were used as a separator. A solution of 1 M $LiPF_6$ in ethylene carbonate and diethyl carbonate (3/7; *m/m*) was used as electrolyte. The test cells were assembled in an argon filled glove box.

Due to problems with electrodes fabricated with $LiFePO_4$/C 5.4 wt% and limited battery tester capacity, $LiFePO_4$/C with 5.4 wt% is excluded from the electrochemical characterization discussion. The results of CV measurements on $LiFePO_4$/C nanocomposites with carbon content of 2.1, 4.4, 6.1, and 7.3 wt% are shown in Figure 38 (a). All the samples possessed a similar pattern of single pair redox reaction that occurred at approximately 3.42 V, indicating two-phase

charge-discharge reaction of Fe^{2+}/Fe^{3+} redox couple. As for the sample with 2.1 wt%, the cathodic peak is observed at 3.35 V while the anodic peak appears at 3.48 V. This result in a voltage separation of 0.13 V and this value is found to be independent of the carbon content. A sharper peak of oxidation and reduction is recorded after the second cycle, suggesting restructuring of $LiFePO_4$/C during the first cycle as mentioned before (Figure 38b). All the $LiFePO_4$/C samples with different carbon content comprise symmetrical peaks regardless of the amount of carbon in the $LiFePO_4$/C. The sluggish oxidation reaction of the sample with the lowest amount of carbon was improved after the first cycling, which is most probably due to microstructural alteration or improvement of wetting in the electrode. Nonetheless, the sample with 7.3 wt% shows the sharpest redox peaks signifying intense efficiency of the redox reaction that is obtainable as a result of the highest electronic conductivity (60.1 mS cm^{-2}). This finding is consistent with the recent work conducted by Lin et al. showing that sharp oxidation and reduction peaks of $LiFePO_4$/C suggest good kinetics behavior. They observed respective results when the carbon content is as high as 7 wt%. Overall, results of first and second CV point to one solid conclusion. That is coating with higher amounts of glucose provides small particle size and leads to increased electronic conductivity resulting in increasingly sharp profiles during CV measurement. It also validates that reduced particle size efficiently enhances the movement of Li^+ ions during the lithiathion/delithiation process for $LiFePO_4$.

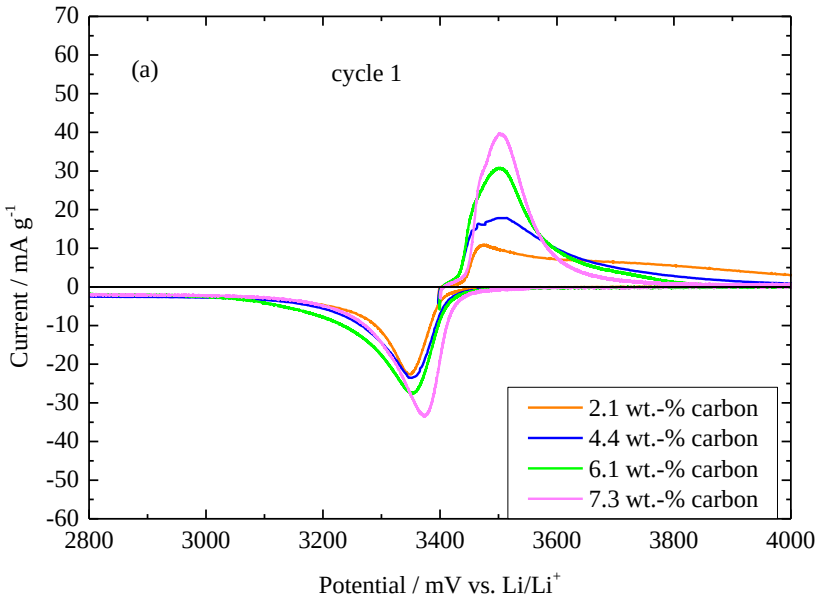

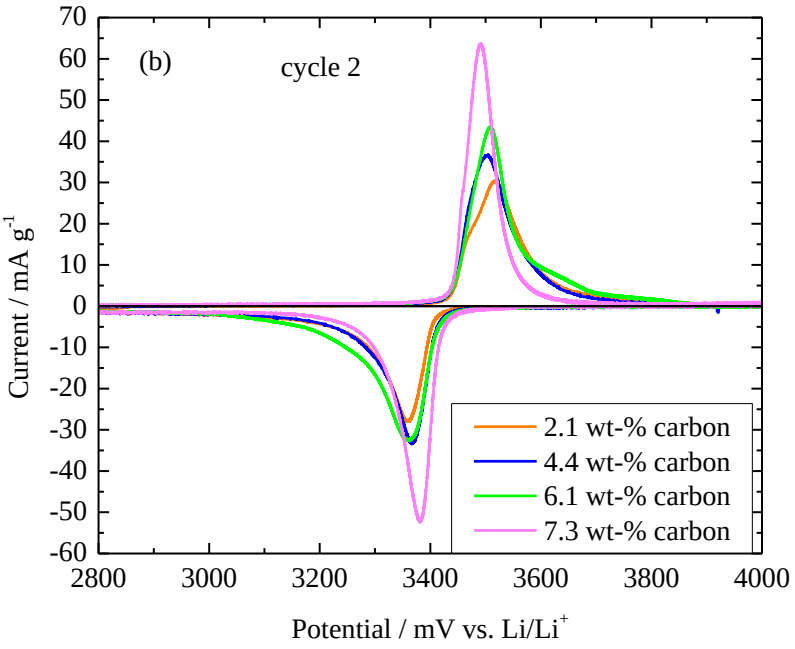

Figure 38: Cyclic voltammetry of $LiFePO_4$/C with different amounts of carbon; (a) first cycle measured and (b) second cycle.

Nanocomposite $LiFePO_4$/C with varied amount of carbon was taken through 75 cycles to determine the capability and sustainability of this material upon charging/discharging at a constant current of 1 C. All samples showed a stable cycle performance after repeated cycling indicating high stability and uniform coating with conductive carbon. As it can be seen from Figure 39, the samples with 6.4 and 7.3 wt% carbon possess approximately the same value (119 mAh g^{-1}) of capacity at 1 C rate, while the sample with the least amount of carbon (2.1 wt%) barely reaches 72 mAh g^{-1}. However, as the cycling continues, the capacity of this sample began to rise gradually to reach 80 mAh g^{-1} at cycle 75. This stunning behavior is governed by the fact that nanosized $LiFePO_4$/C particles effectively boost the cycling performance even at amounts as low as 2.1 wt%. In comparison, $LiFePO_4$/C with 4.4 wt% carbon shows a significant decrease in capacity at 1 C compared to the first results obtained for LFPC1 (4.4 wt% of carbon, prepared without applying milling) featuring a capacity of 117 mAh g^{-1} at 1C rate. The reason for the difference is not clear. It might be either attributed to the different binder system or to the network structure of the carbon found for LFPC1. The comparison between LFPC1 conducted first and

$LiFePO_4$/C with 4.4 wt% indicates that milling during synthesizing $LiFePO_4$/C is affecting the electrochemical performance as milling efficiently provide homogeneous coating surrounded the active material of $LiFePO_4$/C.

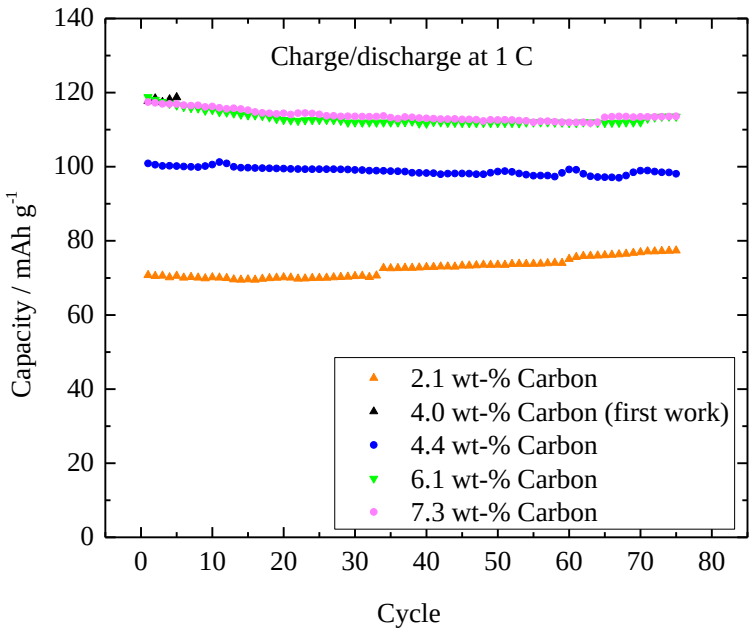

Figure 39: Cycling capability of $LiFePO_4$/C with different amounts of carbon content at a constant current of 1 C

Therefore, it is always difficult to directly compare the performances of $LiFePO_4$/C as each and every researcher uses a different technique or a different combination of the factors affecting materials performance. Nonetheless, it was found that the same phenomena of excellent cycling performance of $LiFePO_4$/C with the highest amount of carbon was also observed by many groups working on a finding the best amount of carbon content for $LiFePO_4$/C [91, 106, 130, 216].

Figure 40 represents the rate retention of $LiFePO_4$/C at different current rates ranging from 0.05 to 16 C and returning to 0.1 C. Again, the samples containing 6.1 and 7.3 wt% of carbon provide identical capacities, initially and also at higher current rates. It is a normal trend for battery materials to produce a lower capacity with higher current rates [217]. Surprisingly, at a current of 16 C, all three samples with 4.4, 6.1, and 7.3 wt%, showed the same value of 40 mAh

g^{-1}. This result suggests that either the electrolyte or the lithium counter electrode are limiting the current. However, $LiFePO_4$/C with the least amount of carbon (2.1 wt%) continuously recorded increments in capacity at each current rate employed, indicating restructuring of the particle after cycling. After cycling back to 0.01 C, the capacity of $LiFePO_4$/C with 2.1 wt% of carbon substantially rose by about 16% from its initial recorded value. This implies that the morphology of this material was altered during discharge that has improved the capacity after a certain number of cycles at varied current rates.

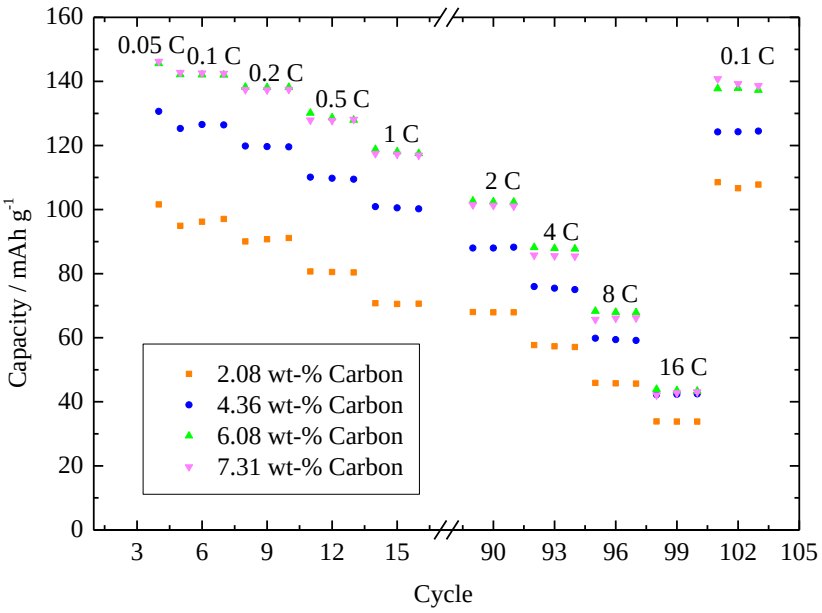

Figure 40: Rate capability at different amounts of residual carbon content $LiFePO_4$/C

In conclusion, carbon coating has proved to yield a significant impact on the electrochemical behavior of $LiFePO_4$ regardless of the amount used. Typically, a higher amount of carbon will sharply increase the electronic conductivity that leads to improved rate retention. In this work, at least 6 wt% of residual carbon would be beneficial to significantly enhance the capacity of $LiFePO_4$ at moderate and high current rates. Hence, this method ascertains production of high performance nanocomposite $LiFePO_4$/C with promising and sustaining electrochemical properties.

4.3 $LiFe_{0.7}Mn_{0.3}PO_4/C$

4.3.1 Synthesis and characterization of $LiFe_{0.7}Mn_{0.3}PO_4/C$

After the promising electrochemical properties obtained with nanocomposite $LiFePO_4/C$, doping of this material with a suitable cation towards higher energy density of $LiFePO_4/C$ is investigated. Therefore, the third part of this thesis deals with the synthesis and characterization of $Fe_{1-x}Mn_xPO_4$. It is known that adopting certain amount of Mn beneficially increases the energy density of $LiFePO_4/C$. Manganese is frequently studied and used in the cathodes of Li-ion batteries as described by previous work done earlier [61, 62, 218]. As Mn^{3+}/Mn^{2+} has a higher potential of 4.2 V vs Li/Li^+ (compared to Fe^{3+}/Fe^{2+} at 3.4 V), substituting a certain amount of iron for manganese would increase the energy density of $LiFePO_4$. Doping was carried out in the initial first step of the cathode material synthesis, the spray-flame synthesis of the phosphate. Therefore, manganese (III) acetylacetonate was mixed with iron acetylacetonate and tributyl phosphate in toluene. Due to the limited solubility of manganese (III) acetylacetonate, a 0.20 M solution was prepared substituting 30 mol% of $Fe(acac)_3$ by $Mn(acac)_3$. As was found from the synthesis of iron phosphates at different molar concentrations, there is only a marginal difference between materials synthesized from 0.2 and 0.35 M solution, respectively After spray-flame synthesis the resultant sample was calcined at 600°C. Table 6 shows the particle sizes received from BET and XRD measurements of as-prepared $Fe_{0.7}Mn_{0.3}PO_4$ and those calcined at 600°C.

Table 6: Particle size of pristine and annealed $FePO_4$ doped with 30 mol% Manganese

Dopant concentration/ mol %	As-prepared		Calcined at 600°C		
	Specific surface area /m^2 g^{-1}	Particle size D_{BET} /nm	Specific surface area/m^2 g^{-1}	Particle size D_{BET} /nm	Crystallite size/nm
30	80	26	24	81	39

As-prepared $Fe_{0.7}Mn_{0.3}PO_4$ has a higher specific surface area of 80 m^2 g^{-1} compared to the calcined $Fe_{0.7}Mn_{0.3}PO_4$ (24 m^2 g^{-1}). Accordingly, the calculated particle sizes are 26 and 81 nm, respectively. As mentioned before, this is due to the fact that the particles grow during heated at 600°C in the same manner as undoped $FePO_4$.

Figure 41 shows the XRD pattern for $Fe_{0.7}Mn_{0.3}PO_4$ calcined at 600°C. Regardless of doping, the trigonal structure with space group P321 was found similar to the undoped $FePO_4$ explained earlier in this thesis. However, there is one peak at $2\theta = 29°$ which can be assigned to Mn_3O_4 as a by-product of the calcination process suggesting that the manganese doped material is not as thermodynamically stable as the undoped. The comparison between particle sizes received from BET and XRD also suggests that the annealed material consists of bigger aggregates containing a couple of smaller crystallites of about 40 nm. Like the addition of carbon, segregation of Mn_3O_4 might also hamper particle growth during calcination.

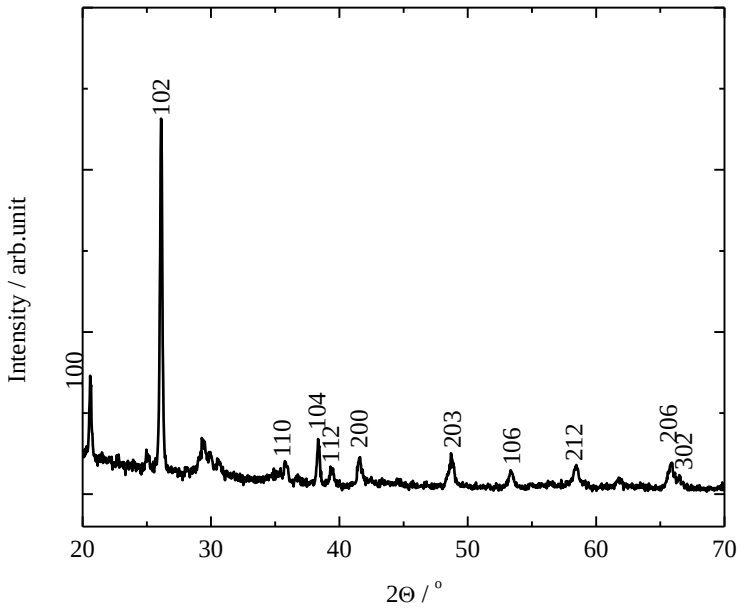

Figure 41: XRD pattern of calcined $FePO_4$ doped with 30 mol% Mn

Nevertheless, the established procedure towards the carbon nanocomposite was continued. Similar to the experiments on LFPC1, $Fe_{0.7}Mn_{0.3}PO_4 \cdot xH_2O$ was mixed with Li_2CO_3 and 16 wt% of glucose using a mortar. This was done in particular to compare the electrochemical behavior of manganese doped lithium iron phosphate with the first result obtained for the undoped $LiFePO_4$/C. The synthesized sample was characterized with BET, XRD, XPS, Raman, TEM, EDX and SEM. Table 7 shows the particle size of $LiFe_{0.7}Mn_{0.3}PO_4$/C (LFMPC1) characterized using BET and XRD. Doping with 30 mol% Mn shows a high specific surface area for $LiFe_{0.7}Mn_{0.3}PO_4$/C. The particle size calculated from BET is 54 nm, which is in line with the

crystal size calculated from XRD indicating that this sample is composed mostly of separate, single crystalline particles.

Table 7: Physical properties of first attempt $LiFe_{0.7}Mn_{0.3}PO_4/C$ (LFMPC1)

Sample	Specific surface area /m^2 g^{-1}	Particle size D_{BET} /nm	Crystallite size D_{XRD}/nm	Carbon content/ wt%
LFMPC1	31	54	50	4.0

Figure 42 illustrates the X-Ray diffraction pattern for $LiFe_{0.7}Mn_{0.3}PO_4/C$ calcined at 600°C (similar to LFPC1). The pattern indicates that $LiFe_{0.7}Mn_{0.3}PO_4/C$ is highly crystalline and consists of pure olivine phase which could be indexed to orthorhombic structure with space group of Pnma and lattice constants of a = 10.355, b = 6.026 and c = 4.709 Å.

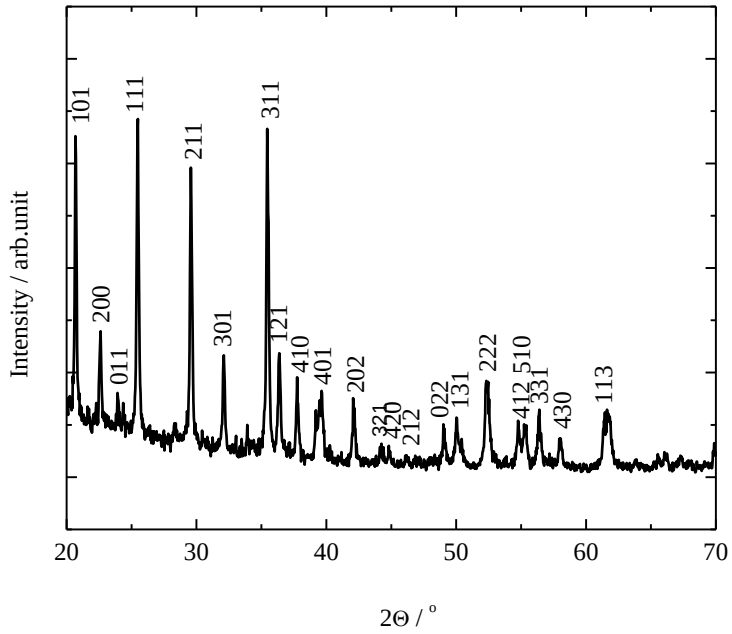

Figure 42: X-Ray Diffraction pattern for $LiFe_{0.7}Mn_{0.3}PO_4/C$ synthesized at 600°C for 16 hours (LFMPC1)

It is worth to mention that there is an increase in unit cell volume of about 0.7% compared to LFPC1. This is in good agreement with the work of Honma et al. [66] who observed a

linear increase in lattice parameter when substituting iron in $LiFePO_4$/C with manganese from 0 to 80 mol% and can be explained by Vegard's law. In addition, there are no peaks related to carbon structures or to other, manganese containing species as was observed before.

The carbon content determined using elemental analysis is 4.0 wt% derived from decomposition of glucose during calcinations at 600°C, which is almost identical to the value found for LFPC1. A Raman measurement was conducted in order to investigate the typical structure of carbon in $LiFe_{0.7}Mn_{0.3}PO_4$/C and again a similar pattern as obtained for all other samples was observed, see Figure 43.

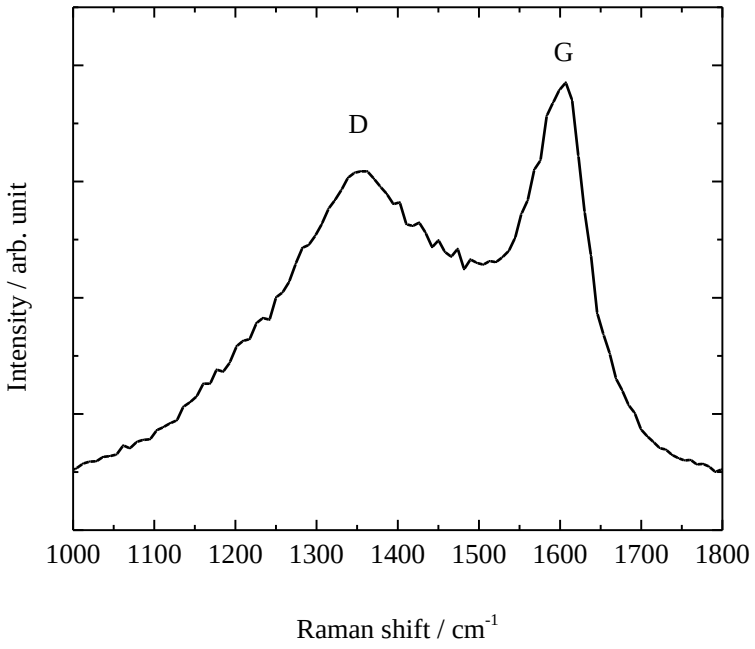

Figure 43: Raman spectrum for $LiFe_{0.7}Mn_{0.3}PO_4$/C (LFMPC1)

Since the structure of carbon was already identified by Raman measurement, another important criterion worth investigating was the valence state of Fe in nanocomposite $LiFe_{0.7}Mn_{0.3}PO_4$/C. Therefore, X-ray photoelectron spectroscopy was performed and the result is shown in Figure 44. From this figure it is clear that the nanocomposite $LiFe_{0.7}Mn_{0.3}PO_4$/C is composed of only Li, Fe, Mn, P, O and C with no impurities detected. Analysis of Fe3p provides information about the bulk properties of the material as compared to the Fe2p peak which basically gives an overview of the surface properties as the kinetic energy of photoelectrons coming

into the analyzer is 770 eV for Fe2p and 1430 eV for Fe3p. This resulted in photoelectron depth about 1.5 times greater for Fe3p than for Fe2p [207]. As analyzed from the Fe3p peak which located at 55 eV, Fe^{2+} is the dominating valence state indicating that good electrochemical properties are attainable with this sample. However, detailed examination of Fe2p shows binding energy of $Fe2p_{3/2}$ and $Fe2p_{1/2}$ at 712 eV and 726 eV which suggests that the valence state of iron is Fe^{3+}. Thus, it is clear that the surface of this material was covered by Fe^{3+} instead of Fe^{2+} probably due to oxidation with the atmosphere during handling and transporting in air.

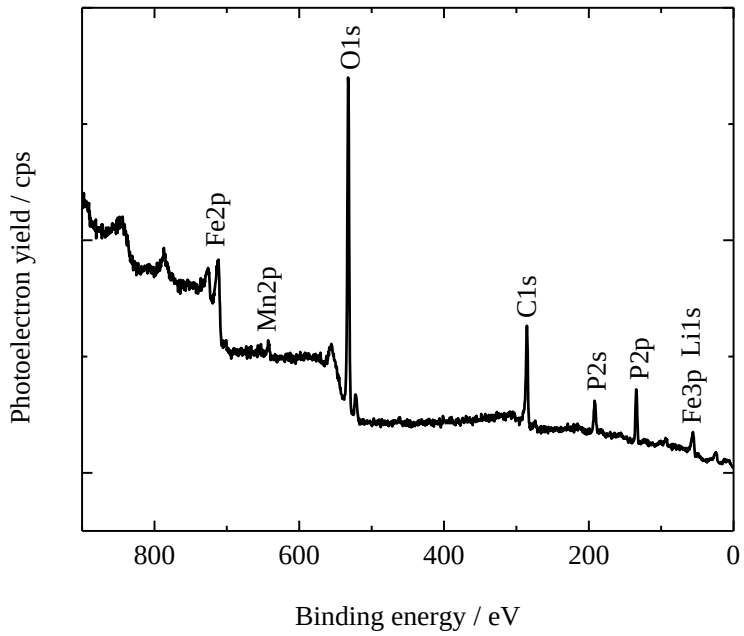

Figure 44: X-ray photoelectron spectrum for $LiFe_{0.7}Mn_{0.3}PO_4/C$ (LFMPC1)

Figure 45 (a) demonstrates the morphological structure of $LiFe_{0.7}Mn_{0.3}PO_4/C$ obtained by TEM measurement. The image suggests that the active material $LiFe_{0.7}Mn_{0.3}PO_4$ is coated with an inhomogeneous amorphous layer of 1 to 4 nm. In addition to this, SEM measurements were conducted to study the morphology of $LiFe_{0.7}Mn_{0.3}PO_4/C$ in lower magnification. It can be seen from Figure 45 (b) that the material is composed of a lot of primary particle measuring around 50 nm in accordance to the results from BET and XRD.

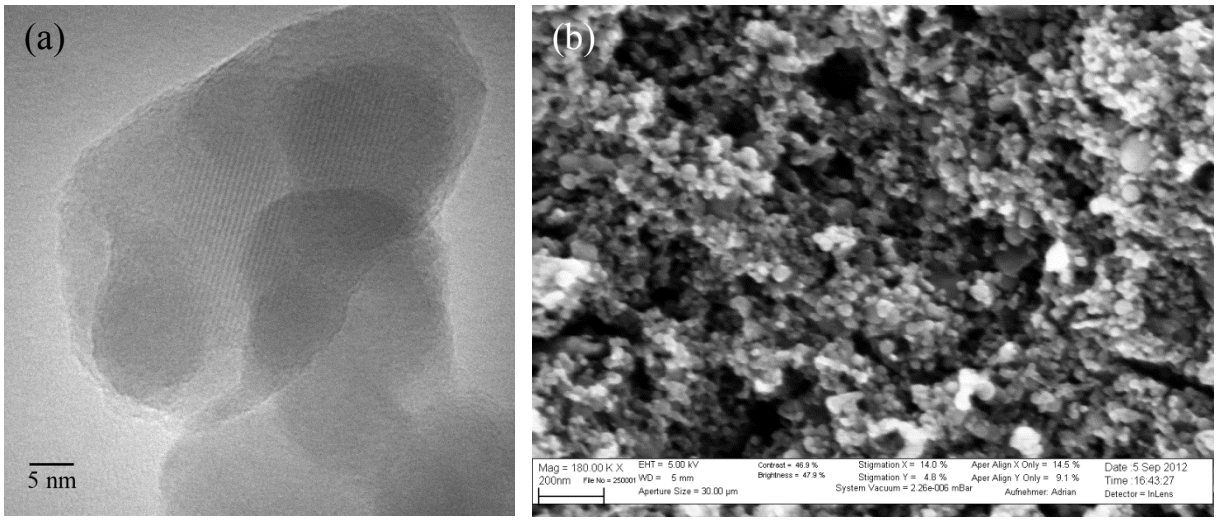

Figure 45: TEM (a) and SEM images of LFMPC1

4.3.2 Electrochemical characterization of $LiFe_{0.7}Mn_{0.3}PO_4/C$

The resultant powder was formulated as a cathode material using polyacrylic acid as a binder which was conducted as before by Sebastian Wennig. Figure 46 (a) shows the cyclic voltammetry of this sample recorded between 2.6 and 4.7 V vs Li/Li^+ with a sweep rate of 0.01 mV s^{-1}. Two pairs of redox reactions take place in this CV measurement involving Fe and Mn species. Oxidation and reduction reaction for Fe species were recorded at 3.51/3.39 V, and 4.05/3.93 V were recorded for manganese, respectively. A voltage interval of 0.12 V was calculated for the first cycle of iron and this interval value decreased to 0.07 V after the second cycle demonstrating reversibility and faster kinetics of the redox reaction. Similarly, the interval voltage of Mn species reduced gradually after the second cycle from 0.15 to 0.02 V, indicating low polarization that leads to enhanced redox reactions. Therefore, this result strongly demonstrates the successful incorporation of electrochemically active manganese into the olivine structure. It is also worth mentioning that the voltage of the reduction reaction of Fe species is slightly shifted as a result of expansion of the unit cell volume. This result is in good agreement with the work conducted by Kobayashi et al. [218], which also reported a shifted voltage of the iron redox pair for Mn-doped $LiFePO_4$.

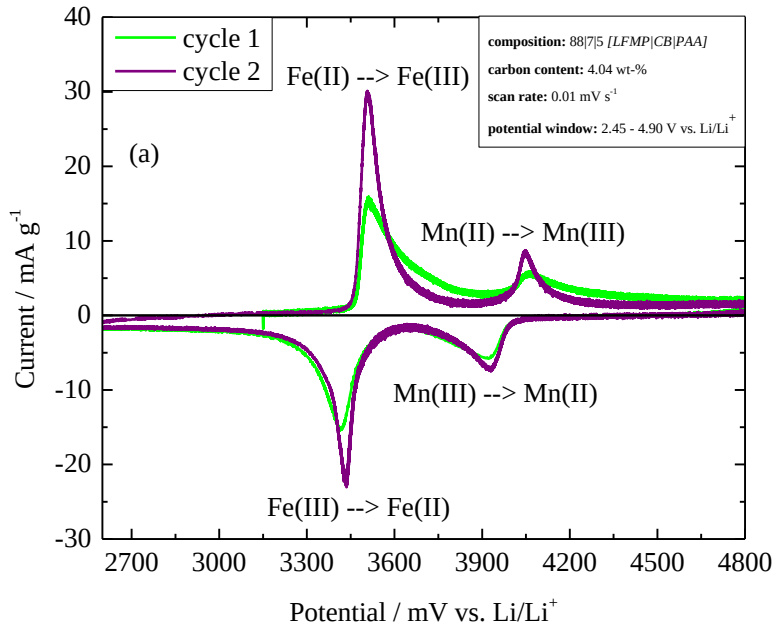

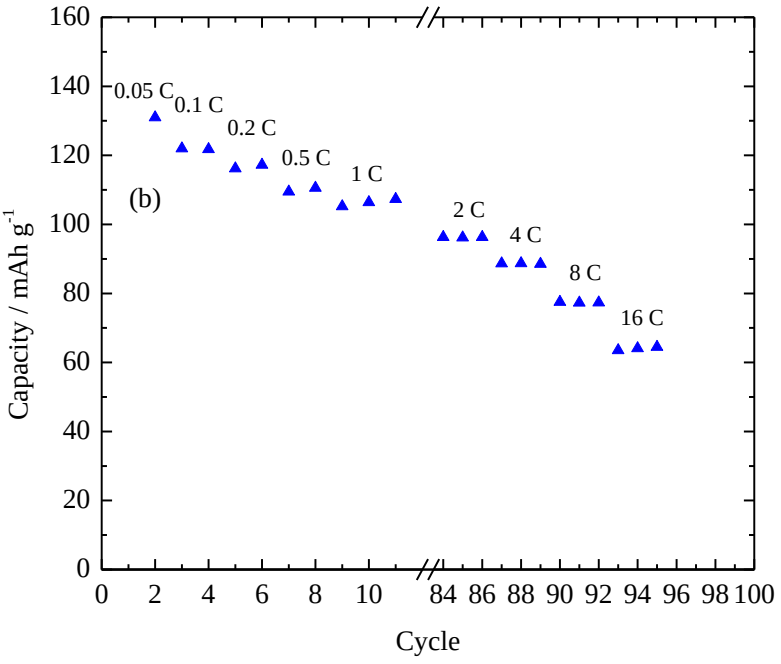

Figure 46: Cyclic voltammetry (a) and rate capability (b) of nanocomposite $LiFe_{0.7}Mn_{0.3}PO_4/C$

Figure 46 (b) depicts the initial discharge capacity of nanocomposite $LiFe_{0.7}Mn_{0.3}PO_4/C$ from 0.05 C up to 16 C. A higher discharge capacity of 130 mAh g^{-1} is recorded at low currents (0.05 C) and this value decreased gradually to 108 mAh g^{-1} after a greater discharge current (1 C) was applied. The capacity degraded even lower when the current reach 16 C with capacity of 66 mAh g^{-1}. This shows that the electrode polarization resistance of $LiFe_{0.7}Mn_{0.3}PO_4/C$ increases sharply with increasing current rate.

The electrode was further cycled at 1 C rate for 50 cycles to determine the capability of this material to sustain its capacity for a certain period of time. Figure 47 shows the cycling capability diagram of $LiFe_{0.7}Mn_{0.3}PO_4/C$ at a constant current of 1 C. Similarly as observed for the lithium iron phosphates investigated before, there is no capacity fading after 70 cycles and the capacity is stable at 114 mAh g^{-1}.

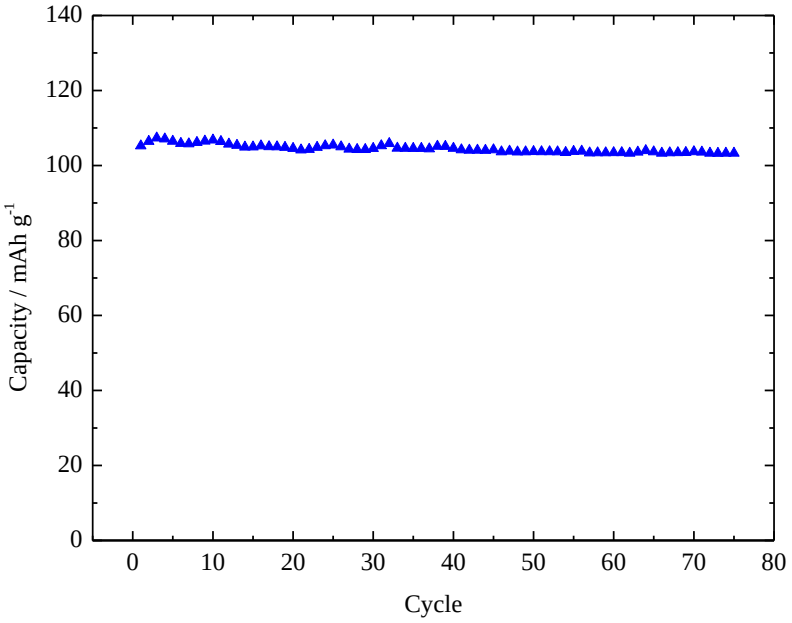

Figure 47: Cycling performance of nanocomposite nanocomposite $LiFe_{0.7}Mn_{0.3}PO_4/C$ at 1 C rate

This indicates a great stability under high current rates that is obtained for this material. Earlier, Yao et al. [68] produced $LiFePO_4/C$ doped with 30 mol% Mn using the sol-gel method and had a bad capacity fading from 98 to 40 mAh g^{-1} after 50 cycles at 0.125 C rate while Chang et al. [219] reported fluctuating cycling performances with capacities around 115 mAh g^{-1} rec-

orded at 0.2 C rate for $LiFe_{0.7}Mn_{0.3}PO_4/C$ obtained from solid-state reaction. Thus, this promising result of doping with Mn gave rise to further work to be done in order to vary the Mn content.

4.4 Influence of Mn concentration in $LiFe_{(1-x)}Mn_xPO_4/C$ (x = 0.02 and 0.20)

4.4.1 Characterization of $Fe_{(1-x)}Mn_xPO_4$ and $LiFe_{(1-x)}Mn_xPO_4/C$

In order to investigate the influence of manganese content on the electrochemical properties, $FePO_4$ was doped during gas-phase synthesis with manganese amounts of 1, 2 and 20 mol%. The initial experiments elaborated before deal with 30 mol% Mn doped into $FePO_4$ and subsequent post-treatment with Li_2CO_3 and 16 wt% glucose to produce $LiFe_{0.7}Mn_{0.3}PO_4/C$. However, the calcination temperature used was conducted based on the minimum temperature for $FePO_4$ crystallization extracted from TG measurement (see Figure 16). Firstly, the calcination temperature needed to produce nanocomposite $LiFe_{(1-x)}Mn_xPO_4/C$ without any impurities is investigated and the results will be described. Additionally, the effect of different amounts of Mn is explored while applying 25 wt% of glucose which was found to provide the optimum carbon content of about 6% with respect to materials prepared by the method used within this thesis. Spray-flame synthesis was used to fabricate $Fe_{(1-x)}Mn_xPO_4 \cdot xH_2O$ (x = 0.01, 0.02 and 0.20) by applying the same precursor used before. All samples were characterized using BET and XRD prior to post-treatment with Li_2CO_3 and glucose.

Table 8 shows the particle sizes received from BET and XRD measurements. While the samples containing 1 and 2 mol% Mn are almost identical, the sample containing 20 mol% of Mn shows a slight but almost negligible decrease in particle size.

Table 8: Physical properties of as-prepared and calcined at 600°C $Fe_{(1-x)}Mn_xPO_4$ (x = 0.01, 0.02 and 0.20)

Dopant concentration/ mol %	As-prepared		Calcined at 600°C		
	Specific surface area /m^2 g^{-1}	Particle size D_{BET} /nm	Specific surface area /m^2 g^{-1}	Particle size D_{BET} /nm	Crystallite size/nm
1	75	28	23	86	42
2	72	29	23	86	41
20	82	25	25	80	36

Thermogravimetric measurement was performed in order to determine the temperature needed to remove excess water inside the samples and to produce crystalline $Fe_{(1-x)}Mn_xPO_4$.

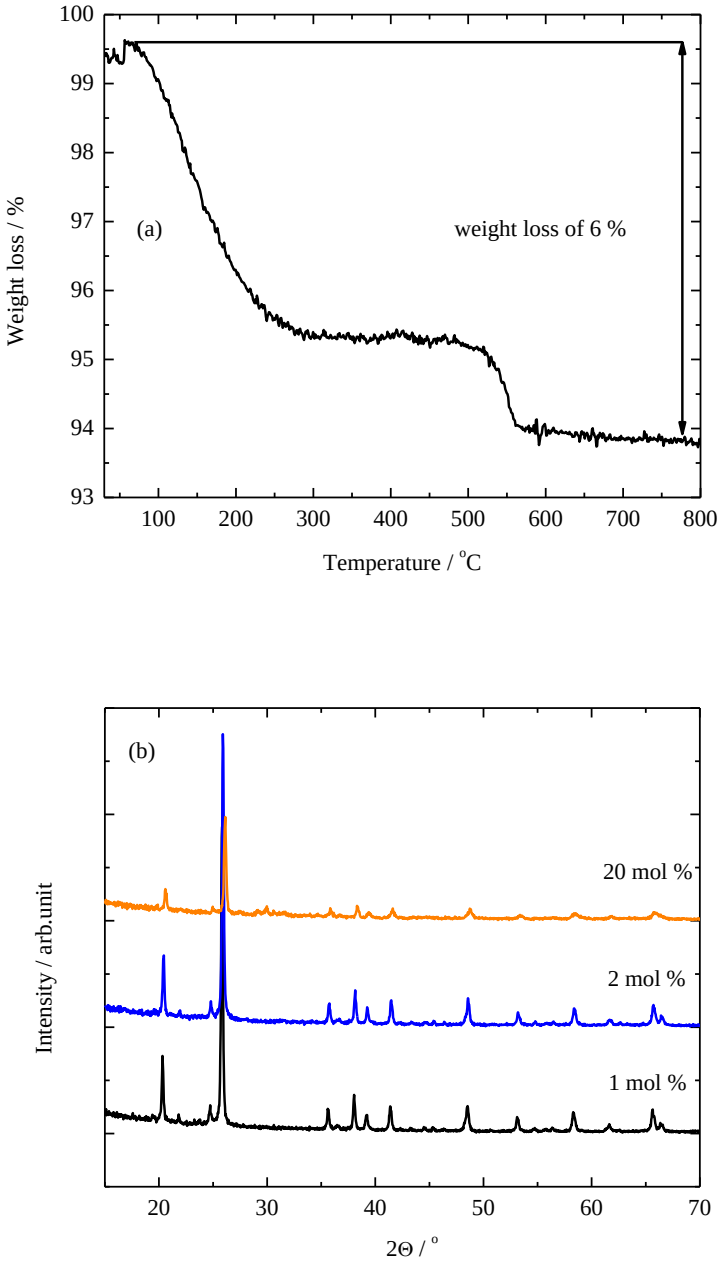

Figure 48: Thermogravimetry measurement of amorphous $Fe_{(1-x)}Mn_xPO_4$ (a) and XRD pattern for $Fe_{(1-x)}Mn_xPO_4$ (with x = 0.01,0.02 and 0.20) after being calcined at 600°C (b)

All samples show very similar behaviour, Figure 48 (a) depicts the TG diagram obtained from $Fe_{0.8}Mn_{0.2}PO_4$. The result indicates that calcination of the materials requires at least a minimum temperature of 560°C. Hence, the samples were annealed at 600–800°C.

Figure 48 (b) illustrates the XRD pattern for $Fe_{(1-x)}Mn_xPO_4$ with x = 0.01, 0.02 and 0.2 annealed at 600°C. All the samples are highly crystalline with a trigonal structure that matches well with ICDD 29-0715. The results are in accordance to the undoped $FePO_4$ and they show that the materials are free from any impurities detectable by XRD. As before, it indicates that doping with small amounts of Mn causes no changes in the crystalline structure of $FePO_4$. It is worth to mention that the peak intensity becomes lesser for $Fe_{0.8}Mn_{0.2}PO_4$ compared to $Fe_{0.99}Mn_{0.01}PO_4$ and $Fe_{0.98}Mn_{0.02}PO_4$ indicating a smaller crystallite size of $Fe_{0.8}Mn_{0.2}PO_4$, see also Figure 48. Because of the similarity of $Fe_{0.99}Mn_{0.01}PO_4$ and $Fe_{0.98}Mn_{0.02}PO_4$, the further study upon the effect of Mn towards the electrochemical performance of $LiFePO_4$/C will be conducted using $Fe_{0.98}Mn_{0.02}PO_4$ and $Fe_{0.8}Mn_{0.2}PO_4$ and the resultant results will be discussed hereafter.

To determine the influence of calcination temperature, a series of the sample with 20 mol% Mn was milled for 12 hours with $LiCO_3$ and 25 wt% glucose before calcination and the annealed samples were characterized using BET and XRD before further investigation concerning the influence of Mn content in $LiFe_{(1-x)}Mn_xPO_4$/C.

Figure 49 shows the particle sizes of $LiFe_{0.8}Mn_{0.2}PO_4$/C calcined at 600 to 800°C with 50°C intervals. Regardless of the applied temperature, it is found that all the samples have a particle size that is less than 50 nm. This is an excellent indication that this route assures nanosized materials even under harsh calcination temperatures. It is clearly illustrated that the residual carbon content based on the initial glucose content of 25 wt% decreased significantly at temperatures above 700°C and the particle size of $LiFe_{0.8}Mn_{0.2}PO_4$/C rose gradually from 32 to 37 nm.

Calcination at 650°C insinuates the smallest particle size and directly thus expresses the highest specific surface area of $LiFe_{0.8}Mn_{0.2}PO_4$/C. Hence, as the smallest particle size attainable after calcination at 650°C, this temperature was used with respect of the investigation of Mn-dopant content.

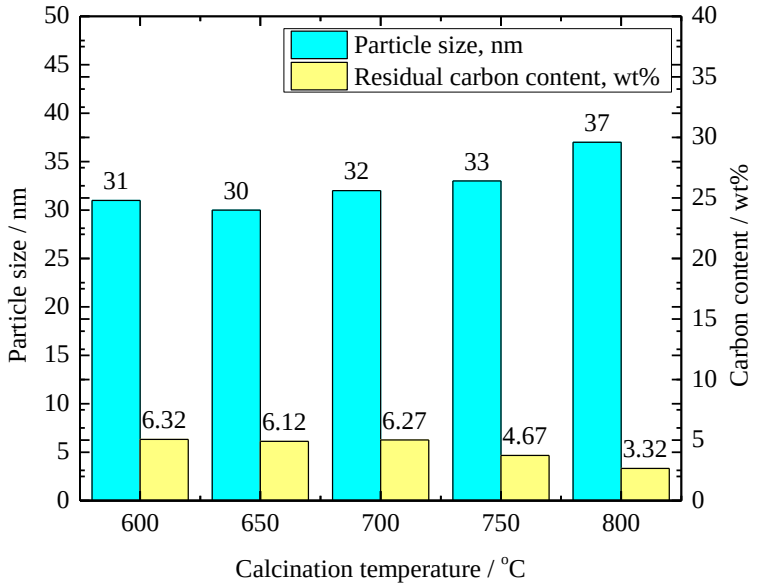

Figure 49: Particle size and residual carbon content of nanocomposite $LiFe_{0.8}Mn_{0.2}PO_4/C$ at different calcination temperatures

Characterization of the resultant $LiFe_{0.8}Mn_{0.2}PO_4/C$ was further expanded to XRD after analysed with BET measurements. As shown in Figure 50, all samples are highly crystalline after calcination at 600 to 800°C. As the existence of carbon in $LiFe_{0.8}Mn_{0.2}PO_4$ greatly inhibits the crystal growth, a lower amount of carbon in this nanocomposite proves to be insufficient to harness the further enlargement of crystals at higher temperatures. It has been shown in the previous section that the amount of carbon begins to decrease significantly after calcination at 650°C. Therefore, there is chance that crystal development starts after the material is calcined at 700°C. The crystallite size determined from the XRD measurements was calculated to be 42 nm, 36, 41, 43, and 45 nm for calcination temperatures of 600, 650, 700, 750, and 800°C, respectively, which is in reasonable accordance to the values received from BET. In addition, the figure indicates no impurities except for the existence of Fe_2P which is detected after calcinating at 750 and 800°C, and no carbon peak is identified in all samples. This finding is comparable with findings from literature [70, 71]. Hence, a calcination temperature of 650°C was found to be the optimum temperature used for synthesizing high purity $LiFe_{(1-x)}Mn_xPO_4/C$ (x = 0.02 and 0.20) with low particle size.

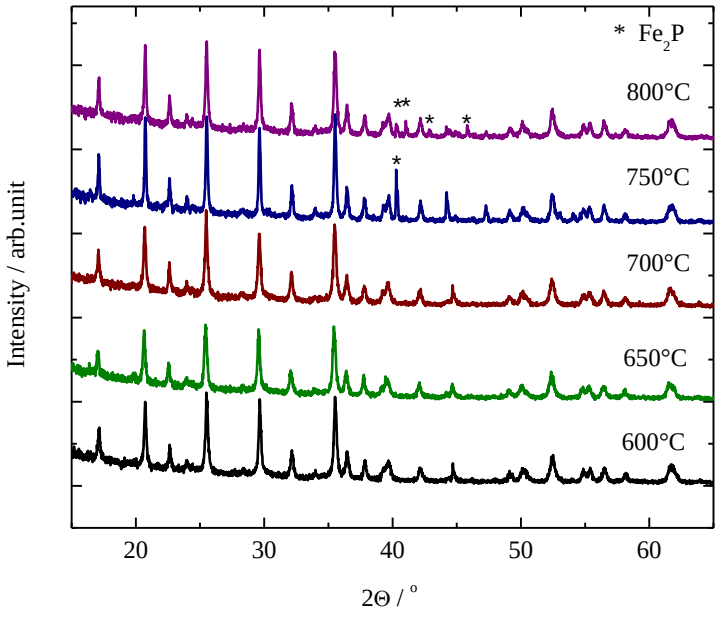

Figure 50: X-Ray diffraction pattern of $LiFe_{0.8}Mn_{0.2}PO_4/C$ calcined at different temperature

In order to compare manganese doped $LiFe_{(1-x)}Mn_xPO_4/C$, two samples with 2 and 20 mol% of Mn were milled with Li_2CO_3 and 25 wt% glucose for 12 hours prior to calcination at 650°C producing nanocomposite $LiFe_{(1-x)}Mn_xPO_4/C$ with x = 0.02 and 0.20. The results obtained from BET and electrical conductivity measurements are shown in Table 9. As observed before (annealing of $Fe_{(1-x)}Mn_xPO_4 \cdot xH_2O$, see Table 8), increasing in dopant concentration from 2 to 20 mol% leads to a slight increase in specific surface area and a respective reduction of the particle size This result is also in parallel to the work conducted by Nakamura's group [62] who stated that the particle size of Mn-doped iron phosphate was insignificantly affected by the amount of Mn. The electrical conductivity of the sample with 2 mol% of Mn is almost identical to the best values obtained for undoped $LiFePO_4/C$ (48 and 60 mS cm^{-1}, resp.) while the electrical conductivity of the sample with 20 mol% Mn is about the double in accordance to the fact that its carbon content is slightly higher.

Table 9: Specific surface area, particle size and electric conductivity of nanocomposite $LiFe_{(1-x)}Mn_xPO_4/C$ at different manganese contents

Sample	Dopant concentration/ mol %	Specific surface area /$m^2\ g^{-1}$	Particle size D_{BET} /nm	Crystallite size D_{XRD}/nm	Carbon content/ wt%	Electrical conductivity/ mS cm^{-1}
LFMPC02	2	47	35	32	5.45	48
LFMPC20	20	50	33	31	5.99	125

Figure 51 shows the crystalline structure of the two different $LiFe_{(1-x)}Mn_xPO_4/C$ samples indicating no impurities such as Fe_2P, FeP or $Mn_2P_2O_7$. Both samples show similar crystallinity and crystallite size, see also Table 9.

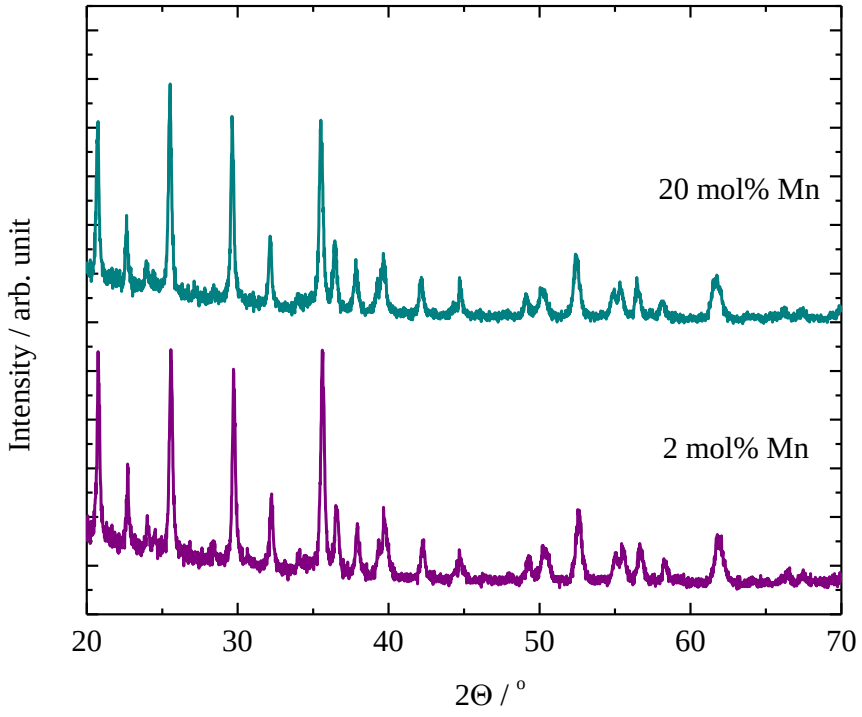

Figure 51: X-Ray diffraction pattern of $LiFe_{(1-x)}Mn_xPO_4/C$ synthesized at 650°C for 16 hours

As Mn^{2+} has a bigger ionic radius of 0.83 Å compared to Fe^{2+} with a radius of 0.78 Å [31], Mn incorporation into the lattice structure should directly influence the lattice parameters. Based on Rietveld refinement using the MAUD program [188], the lattice parameters were calculated and plotted in the manner presented by Figure 52. It can be seen that the lattice parameters of $LiFe_{(1-x)}Mn_xPO_4/C$ system vary almost linearly with the amount of Mn^{2+} replacement which obeyed Vegard's law and is in good agreement with previous findings [31, 56, 62, 66, 69, 220].

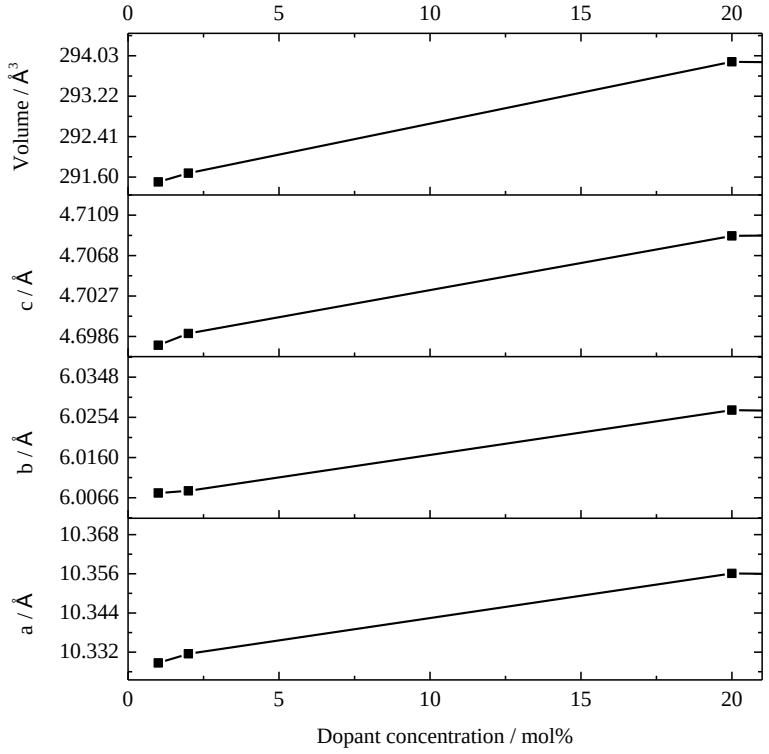

Figure 52: Dependence of the lattice parameters of $LiFe_{(1-x)}Mn_xPO_4/C$ on the Mn content

Figure 53 shows the XPS spectrum for $LiFe_{(1-x)}Mn_xPO_4/C$ for 2 and 20 mol% Mn. The pattern show peaks associated with Li, Fe, Mn, P, O and C. Following a detailed analysis on Fe2p (see Figure 53 (b)) shows that the valence state of iron species in $LiFe_{(1-x)}Mn_xPO_4/C$ is mainly dominated by Fe^{3+} as $Fe2p_{3/2}$ and $Fe2p_{1/2}$ located at 711 and 724 eV, respectively [69]. It is observed that the peak belonging to Mn2p significantly rises for the sample with 20 mol%. An enlarged spectrum of Mn2p reveal that $Mn2p_{3/2}$ and $Mn2p_{1/2}$ located at 641.6 and 653.8 eV, cor-

respondingly is shown in Figure 53 (c) indicating that Mn^{3+} is the dominating oxidation state of Mn [221]. The main possible reason for the oxidation of iron and manganese species is short exposure during handling or transportation in air.

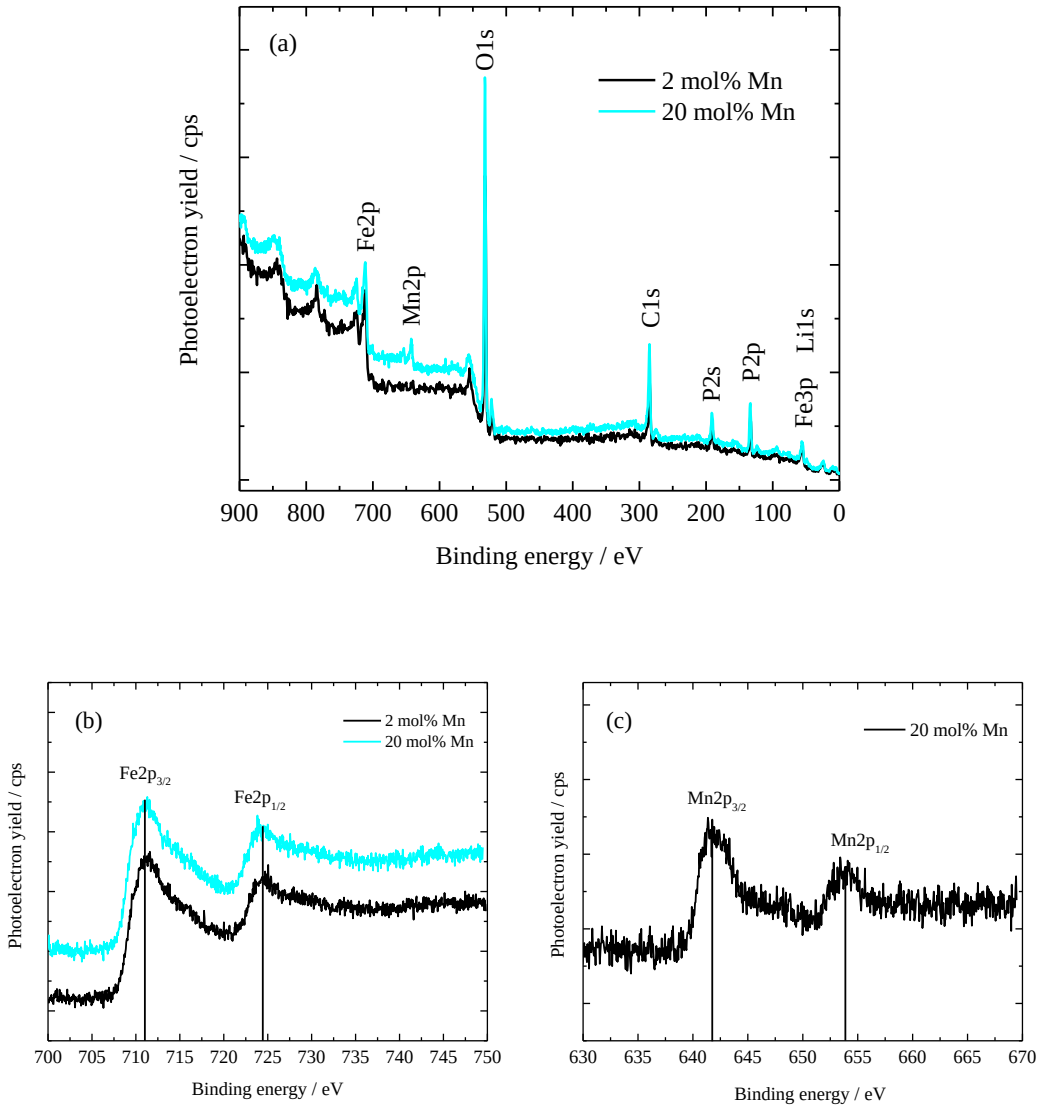

Figure 53: XPS spectra of $LiFe_{(1-x)}Mn_xPO_4/C$ (a), enlarged Fe2p (b) and Mn2p (c) spectra

4.4.2 Electrochemical characterization of $LiFe_{(1-x)}Mn_xPO_4/C$

The promising result of preliminary made $LiFePO_4/C$ doped with 30 mol% Mn leads to further investigation of Mn content in $LiFe_{(1-x)}Mn_xPO_4/C$ in order to determine more precisely the effect of manganese doping towards the electrochemical properties of $LiFe_{(1-x)}Mn_xPO_4/C$. Figure 54 (a) shows the CV diagram of $LiFePO_4/C$ doped with varied amount of Mn at the first cycle with a sweeping rate of 0.01 mV s^{-1}. Referring to the CV diagram, it can be seen that there are two phases of reaction that occur involving oxidation and reduction of Fe and Mn species at 3.44 and 3.98 V vs. Li/Li^+, respectively. Clearly, the oxidation peak for Fe species occurred steadily at a potential of 3.51 V vs. Li/Li^+ while the potential recorded for reduction peak increased from 3.36 to 3.41 V vs. Li/Li^+ accordingly with increasing amount of Mn. This is in good agreement with work done by Nakamura et. al [62] who reported a similar CV behavior for doped $LiFePO_4/C$ which describes that Mn doping had a larger impact on the discharging reaction than on the charging reaction. Figure 54 (b) depicts the subsequent cycle of redox reaction for doped $LiFePO_4/C$ recorded at potentials ranging from 3.0 to 4.3 V vs. Li/Li^+. Sharp peaks for both, the oxidation and reduction reactions were obtained for $LiFe_{0.98}Mn_{0.02}PO_4/C$ and $LiFe_{0.80}Mn_{0.20}PO_4/C$ samples indicating an improved kinetic of the redox reaction. This is also presented by the small potential difference between the anodic and cathodic peaks, doping with 20 mol% Mn provides the lowest polarization. Thus, by doping with a certain amount of Mn, the electrochemical properties of $LiFePO_4/C$ are enhanced compared to the undoped materials. It is not surprising that the manganese-related redox process of the sample with 2% Mn cannot be identified due to the low concentration.

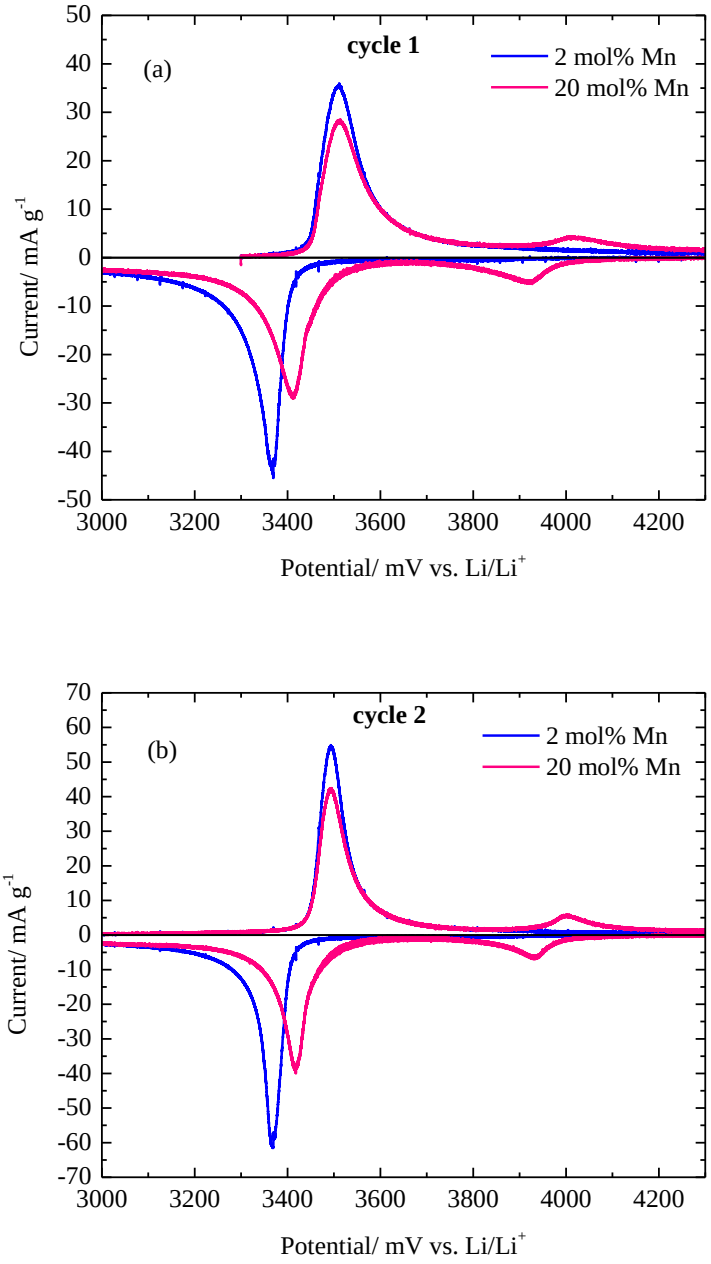

Figure 54: Cyclic voltammetry of $LiFe_{(1-x)}Mn_xPO_4/C$ at first (a) and second cycle (b)

Figure 55 illustrates the rate capability for doped $LiFePO_4/C$ recorded at different C rates. All the samples were cycled three times at each C rate between current intervals. The capacity for each sample is found to decrease gradually with increasing discharge current from 0.05 C to 16 C. Doping with 2 mol% of Mn proved to cause insignificant changes in the electrochemical

properties of $LiFe_{(1-x)}Mn_xPO_4/C$ while the Mn content of 20 mol% leads to increased discharge capacities at higher C rates. These results are also in line with findings from Li et. al [222] and Nakamura et. al [62] who reported excellent electrochemical behavior at high C rates for $LiFe_{(1-x)}Mn_xPO_4/C$ prepared by the modified mechanochemical activation method and the solid-state reaction method, respectively.

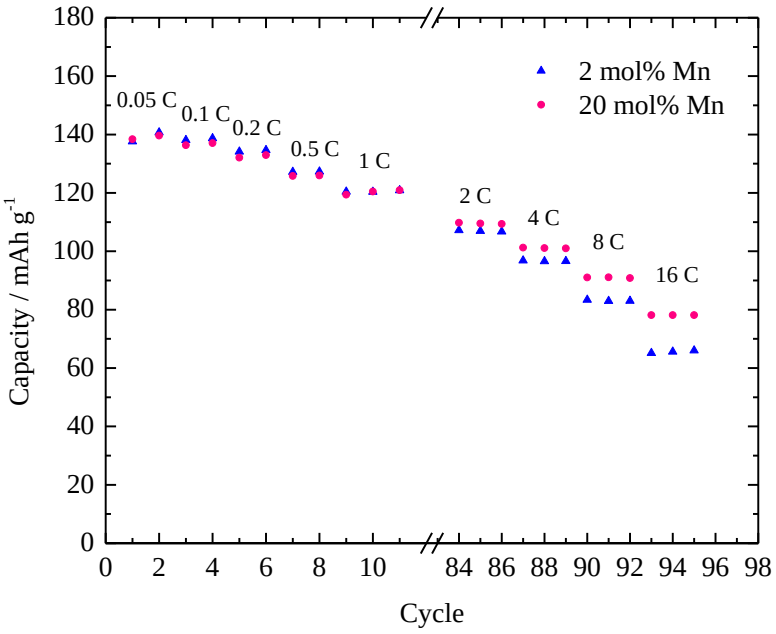

Figure 55: Rate capability of $LiFe_{(1-x)}Mn_xPO_4/C$ at different C rates

The cycle performance of $LiFe_{(1-x)}Mn_xPO_4/C$ (x = 0.02 and 0.20) at a constant current of 1 C is shown in Figure 56. Both samples with 2 and 20 mol% Mn shows a similar capacity of 120 mAh g^{-1} at 1 C rate. As it can be seen, the electrode is extremely within the measured interval of 75 cycles without any significant capacity fading which is considerably better than results reported from literature [71] based on doped $LiFePO_4/C$ with 40 mol% Mn. Thus, it can be stated that the nanocomposite $LiFe_{(1-x)}Mn_xPO_4/C$ prepared from gas-phase $Fe_{(1-x)}Mn_xPO_4$ and subsequent solid-state reaction is capable of producing highly stable cathode materials with excellent electrochemical properties which are suitable for the utilization in Li-ion batteries.

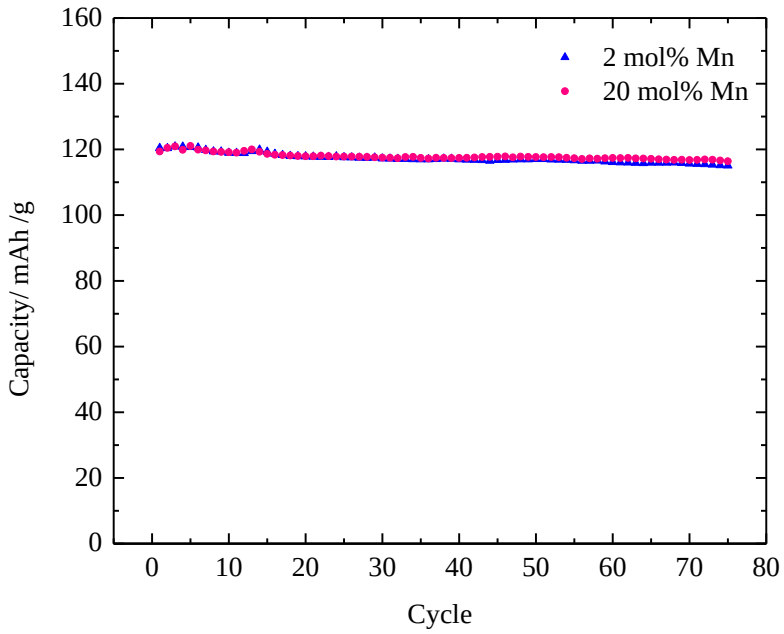

Figure 56: Rate retention of $LiFe_{(1-x)}Mn_xPO_4/C$ at a constant discharge current of 1 C

4.5 Comparison of $LiFePO_4/C$ and $LiFe_{0.8}Mn_{0.2}PO_4/C$ and discussion

In order to determine the effect of Mn doping towards the electrochemical performance of $LiFePO_4/C$, the optimum results obtained for bare and doped $LiFePO_4/C$ are compared. Factors taken into account are kinetics of the electrochemical reaction, capability of producing high capacity at elevated current rate and cycling stability at higher C rates. Figure 57 (a) shows the CV diagram of bare and doped $LiFePO_4/C$ scanned with 0.01 mV s^{-1} at the first cycle. It can be seen that two pairs of redox reactions occur at 3.45 V for $Fe^{2+/3+}$ and 3.98 V for $Mn^{2+/3+}$. Both anodic and cathodic peaks are found to be slightly shifted for doped $LiFePO_4/C$ with a broader shape at the first cycle indicating slow kinetics reaction for the initial charging/discharging process. Polarization resistance for bare and doped $LiFePO_4/C$ was found to be 0.13 V and 0.10 V respectively. This clearly indicates that Mn^{2+} substitution helps to lower the polarization resistance leading to a faster charge/discharge process. Broad redox peaks of the Mn species at about 4 V suggests in this respect a sluggish reaction during the first cycle of delithiation/lithiation process.

However, after the second cycle Figure 57 (b) the redox peaks became symmetrically sharper and provided also a reduced further decreased polarization difference of 0.11 V and 0.08 V for bare and doped $LiFePO_4/C$, respectively. In both cases, polarization of the doped material is reduced compared to pure $LiFePO_4/C$. This result strongly suggests that the reaction kinetics can be improved by doping with manganese and might be attributed to the change in lattice constants thus widening the transport channels for lithium ions. This result is in good agreement with the preceeding work done by Nakamura et. al [62] who described the redox reaction of bare and doped $LiFePO_4/C$ with 20 mol% Mn. As mentioned earlier, faster kinetics of discharging/charging is mainly related to an increase in electronic and ionic conductivity.

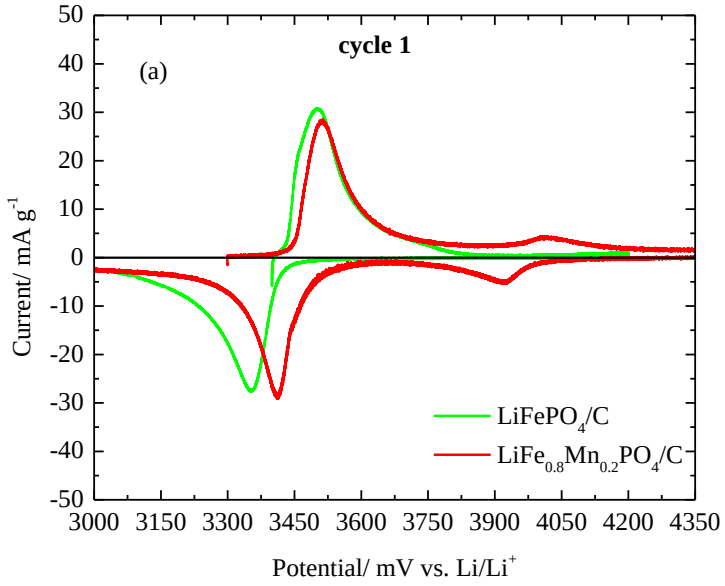

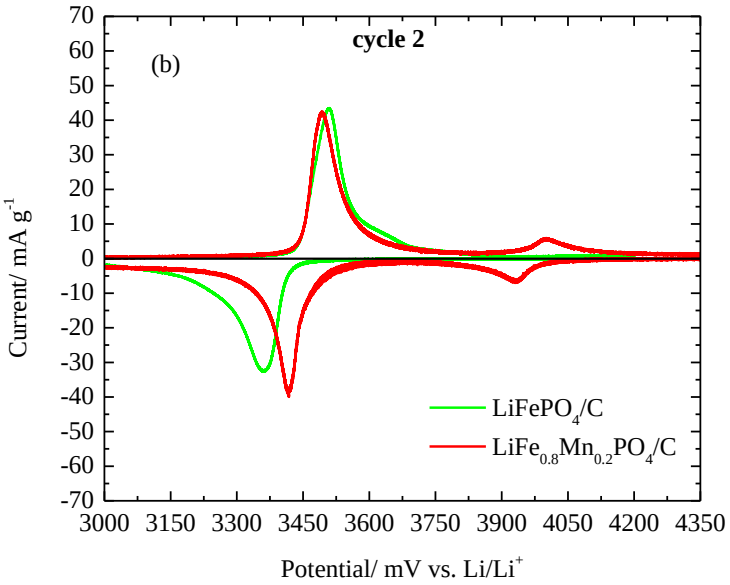

Figure 57: Comparison of cyclic voltammetry of $LiFePO_4/C$ and $LiFe_{0.8}Mn_{0.2}PO_4/C$ at the first cycle (a) and the second cycle (b)

The rate capability or galvanostatic cycling of bare and doped $LiFePO_4/C$ at various C rates is depicted in Figure 58. At low C rates (below 1 C), bare $LiFePO_4/C$ produces a slightly higher capacity than the doped one while around 1 C both, bare and doped $LiFePO_4/C$, provide a

similar capacity of 120 mAh g^{-1}. As the particle size of both materials is almost identical, it indicates that the doped cathode material probably does not provide as many accessible sites for lithium ions as the undoped one. Nevertheless, manganese substitution significantly starts to enhance the rate performance with increasing discharge current, especially at extreme current rates of 16 C. Bare $LiFePO_4$/C is reported to provide 44 mAh g^{-1} while the doped $LiFePO_4$/C provides almost 80 mAh g^{-1}. Similar phenomena are reported earlier also indicating that Mn^{2+} substitution promotes excellent rate capability especially at high C rates [59, 72].

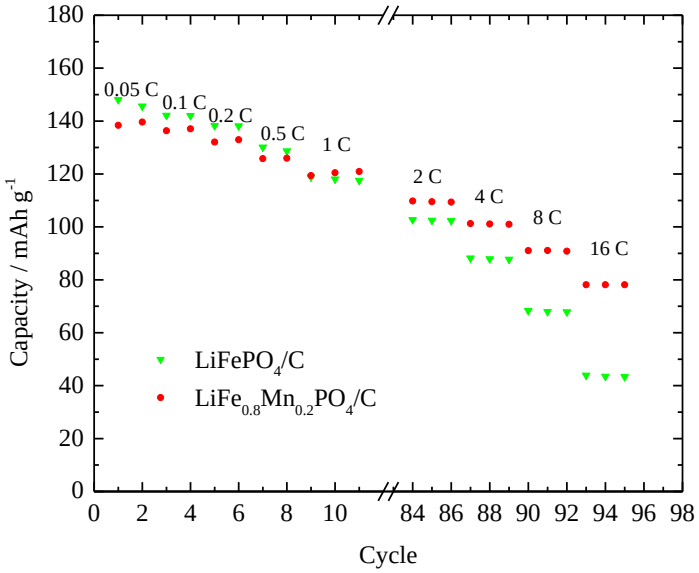

Figure 58: Galvanostatic cycling of $LiFePO_4$/C and $LiFe_{0.8}Mn_{0.2}PO_4$/C at various C rates

Additional examination concerning the cycling capability of bare and doped $LiFePO_4$/C was investigated and the results are illustrated in Figure 59. Both samples were taken through 75 cycles at a constant discharge current of 1 C. The capacities are very similar and only slight degradation is observed. To summarize, these results clearly indicate the importance of doping and nanostructure towards the electrochemical behavior of $LiFePO_4$/C, especially at high current rates and indicates that the manganese doped material is highly suitable for high power applications.

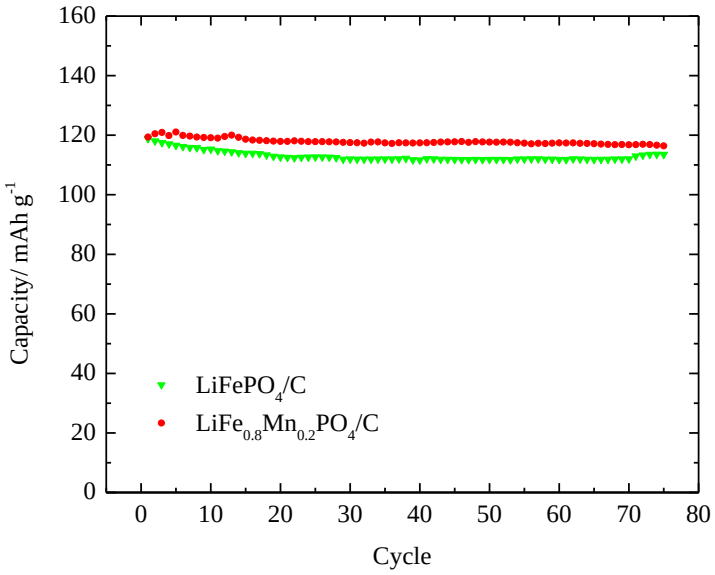

Figure 59: Rate retention of $LiFePO_4/C$ and $LiFe_{0.8}Mn_{0.2}PO_4/C$ at 1 C rate

Moreover, high energy applications also benefit from the addition of manganese as shown in Figure 60 (a). Due to the higher voltage of the Mn^{2+}/Mn^{3+} redox reaction, the energy density of the doped material is in all cases higher than those of bare $LiFePO_4/C$. As a result, nanoscale $LiFe_{0.8}Mn_{0.2}PO_4/C$ is found to be a material of choice with respect to high power and high energy demand. Figure 60 (b) shows the impressive result that the energy density of this material at 16 C is 44% higher than those of the undoped material.

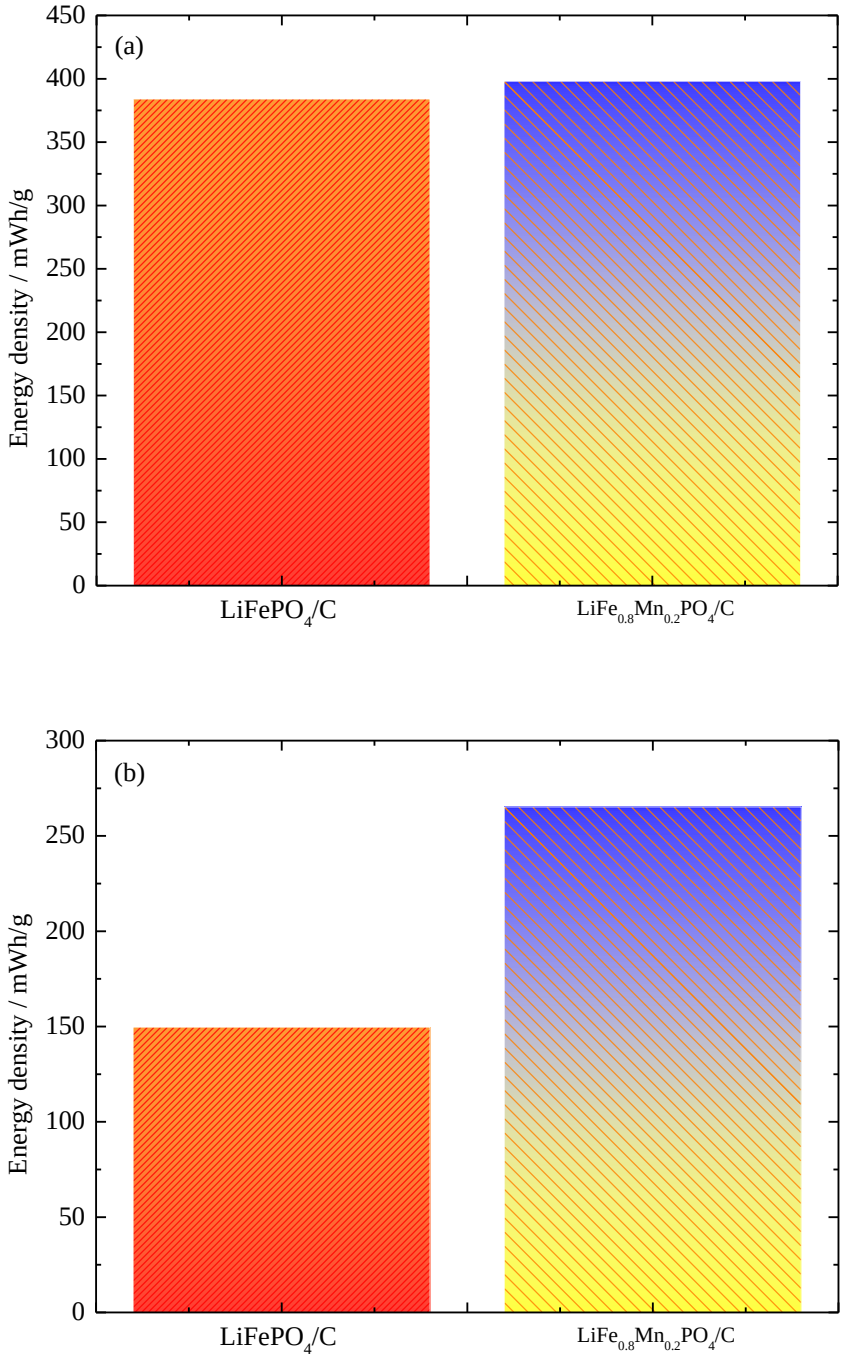

Figure 60: Energy density of $LiFePO_4/C$ and $LiFe_{0.8}Mn_{0.2}PO_4/C$ at 1 C rate (a) and 16 C rate (b)

5 Summary and future work

5.1 Summary

Lithium-ion batteries are of high interest for energy storage in portable and stationary applications. Current and future applications mainly require safe, cheap, high-energy and high-power Li-ion batteries with long lifetimes. The development of cathode material with enhanced electrochemical properties is one of the key factors towards improved batteries. Cost and performance of the cathode materials heavily rely on the synthesis route. Conventional methods namely solid- and solution-based routes provide materials with good electrochemical performance. Nevertheless, there is room for improvement especially with respect to less conducting but potentially high-power materials that demand short diffusion and transport lengths. Nanoscaled cathode materials can meet these requirements thus widening the potentially suitable materials diversity.

This work establishes a new approach towards the synthesis of nanoscaled cathode materials based on lithium iron phosphate. Nanoscaled raw materials are prepared by cost-efficient and scalable gas-phase synthesis followed by a single-step solid-state reaction. Spray-flame synthesis is used to prepare $FePO_4$ from different concentrations of iron(III)acetylacetonate mixed with tributylphosphate in toluene. Even high precursor concentrations of up to 0.35 mol l^{-1} are suitable to produce amorphous iron phosphate nanoparticles with mean particle sizes well below 25 nm. Heating of the pristine powder at 600°C leads to pure, nanocrystalline $FePO_4$ with crystallite sizes below 100 nm suitable for the subsequent solid-state reaction. Annealing of this raw material with Li_2CO_3 and glucose leads to phase-pure $LiFePO_4$/C with olivine structure when applying a temperature in the range of 650–700°C, while milling of the powder mixture in advance provides a homogeneous distribution of carbon in the final product. Investigations with respect to a carbon content that provides sufficient electrical conductivity and good electrochemical performance indicate that at least 5 wt% of residual carbon is required for optimized electrochemical properties. Moreover, residual carbon also suppresses the formation of bigger crystallites and aggregates thus resulting in a typical crystallite and particle size of 30–50 nm. Further physicochemical characterization of the materials by Mößbauer and XPS spectroscopy reveal that the oxidation state of iron is mostly Fe^{2+} as required with a slight oxidation at the surface

resulting in some Fe^{3+}. Raman measurements related to the carbon coating indicate a mixture of amorphous disordered as well as graphite-like carbon in all samples.

A way towards an increase in energy density is investigated by partial substitution of iron by manganese based on its higher redox potential compared to iron. $Fe_{1-x}Mn_xPO_4$ raw materials are made by spray-flame synthesis using a mixture of the respective iron and manganese precursors. Due to solubility limits of manganese-acetylacetonate it is not possible to use as high precursor concentrations as before, nevertheless, it is possible to synthesize materials with almost identical particle size and morphology as before. The resulting structure after the solid-state reaction is always olivine even at manganese concentrations of up to 30 mol% while the lattice constants increases with increasing Mn content in accordance with Vegard's law. Cyclovoltammetry clearly indicates the electrochemical functionality of manganese within the sample. The redox kinetics of manganese doped samples is faster compared to undoped $LiFePO_4$/C leading to significantly decreases the material's polarization. These findings are attributed to the increase in lattice constants thus leading to a widening of the pathways for lithium ions. The detailed investigations towards the properties of undoped and doped $LiFePO_4$/C presented in this thesis show that electrochemical properties can be improved by utilizing methods that can affect the structure as well as the composition of materials. The combination of gas-phase synthesis of nanoparticles and subsequent solid-state reactions is suitable for synthesizing undoped and doped $LiFePO_4$/C with excellent electrochemical properties.

5.2 Future work

Despite the fact that (doped) $LiFePO_4$ is one of the preferred cathode materials for Li-ion batteries due to low costs and high availability, it cannot overcome certain (physical) limits in terms of energy density. A great leap forward could be achieved if one succeeds to incorporate more than one electrochemically active Lithium ion per formula unit. This would require the incorporation either cations or anions or both towards multivalent compositions, i.e., Li_2MnO_3 or $Li_3V_2PO_4$. Unfortunately, most of the principally suitable systems lack of poor ionic conductivity therefore limiting the achievable charge and discharge currents. The methods presented in this thesis enable for further material development where nanostructuring helps to overcome poor bulk properties. Especially the formation of nanoscaled raw materials providing structures with short diffusion pathways and the homogeneous incorporation of carbon supplying the required

electronic conductivity while hampering the formation of aggregates can help to develop new, promising cathode materials.

6 References

[1] M. Winter, R.J. Brodd, What Are Batteries, Fuel Cells, and Supercapacitors?, *Chemical Reviews*, **104** (2004) 4245.

[2] A.S. Arico, P. Bruce, B. Scrosati, J.-M. Tarascon, W. van Schalkwijk, Nanostructured materials for advanced energy conversion and storage devices, *Nat Mater*, **4** (2005) 366.

[3] T. Ohzuku, R.J. Brodd, An overview of positive-electrode materials for advanced lithium-ion batteries, *Journal of Power Sources*, **174** (2007) 449.

[4] T.a.T. Nagaura, K, Lithium ion rechargeable battery, *Prog. Batteries Solar Cells*, **9** (1990) 209.

[5] B.J. Landi, M.J. Ganter, C.D. Cress, R.A. DiLeo, R.P. Raffaelle, Carbon nanotubes for lithium ion batteries, *Energy & Environmental Science*, **2** (2009) 638.

[6] M.S. Whittingham, Materials Challenges Facing Electrical Energy Storage, *MRS Bulletin*, **33** (2008) 411.

[7] M.S. Whittingham, Electrical energy storage and intercalation chemistry, *Science*, **192** (1976) 1126.

[8] J.R. Dahn, E.W. Fuller, M. Obrovac, U. von Sacken, Thermal stability of Li_xCoO_2, Li_xNiO_2 and λ-MnO_2 and consequences for the safety of Li-ion cells, *Solid State Ionics*, **69** (1994) 265.

[9] I. Belharouak, W. Lu, D. Vissers, K. Amine, Safety characteristics of $Li(Ni_{0.8}Co_{0.15}Al_{0.05})O_2$ and $Li(Ni_{1/3}Co_{1/3}Mn_{1/3})O_2$, *Electrochemistry Communications*, **8** (2006) 329.

[10] M.S. Whittingham, Lithium Batteries and Cathode Materials, *Chemical Reviews*, **104** (2004) 4271.

[11] J.M. Tarascon, M. Armand, Issues and challenges facing rechargeable lithium batteries, *Nature*, **414** (2001) 359.

[12] A.K. Padhi, K.S. Nanjundaswamy, J.B. Goodenough, Phospho-olivines as Positive-Electrode Materials for Rechargeable Lithium Batteries, *Journal of the Electrochemical Society*, **144** (1997) 1188.

[13] X. Jie, G. Liang, L. Wang, X.K. Zhi, L. Gao, Kinetics of $LiFePO_4$ cathode material prepared by carbothermal reduction method, *Advanced Materials Research*, **178** (2011) 172.

[14] A.S. Andersson, B. Kalska, L. Häggström, J.O. Thomas, Lithium extraction/insertion in $LiFePO_4$: an X-ray diffraction and Mössbauer spectroscopy study, *Solid State Ionics*, **130** (2000) 41.

[15] B.L. Ellis, K.T. Lee, L.F. Nazar, Positive Electrode Materials for Li-Ion and Li-Batteries, *Chemistry of Materials*, **22** (2010) 691.

[16] K.S. Nanjundaswamy, A.K. Padhi, J.B. Goodenough, S. Okada, H. Ohtsuka, H. Arai, J. Yamaki, Synthesis, redox potential evaluation and electrochemical characteristics of NASICON-related-3D framework compounds, *Solid State Ionics*, **92** (1996) 1.

[17] J. Jiang, J.R. Dahn, ARC studies of the thermal stability of three different cathode materials: $LiCoO_2$; $Li[Ni_{0.1}Co_{0.8}Mn_{0.1}]O_2$; and $LiFePO_4$, in $LiPF_6$ and LiBoB EC/DEC electrolytes, *Electrochemistry Communications*, **6** (2004) 39.

[18] R. Amin, P. Balaya, J. Maier, Anisotropy of Electronic and Ionic Transport in LiFePO4 Single Crystals, *Electrochemical and Solid-State Letters*, **10** (2007) A13.

[19] M. Gaberscek, R. Dominko, J. Jamnik, Is small particle size more important than carbon coating? An example study on LiFePO4 cathodes, *Electrochemistry Communications*, **9** (2007) 2778.

[20] K.T. Lee, J. Cho, Roles of nanosize in lithium reactive nanomaterials for lithium ion batteries, *Nano Today*, **6** (2011) 28.

[21] S. Franger, C. Benoit, C. Bourbon, F. Le Cras, Chemistry and electrochemistry of composite $LiFePO_4$ materials for secondary lithium batteries, *Journal of Physics and Chemistry of Solids*, **67** (2006) 1338.

[22] M.-S. Song, Y.-M. Kang, J.-H. Kim, H.-S. Kim, D.-Y. Kim, H.-S. Kwon, J.-Y. Lee, Simple and fast synthesis of $LiFePO_4$-C composite for lithium rechargeable batteries by ball-milling and microwave heating, *Journal of Power Sources*, **166** (2007) 260.

[23] H. Huang, S.-C. Yin, L.F. Nazar, Approaching Theoretical Capacity of $LiFePO_4$ at Room Temperature at High Rates, *Electrochemical and Solid-State Letters*, **4** (2001) A170.

[24] N. Meethong, Y.-H. Kao, S.A. Speakman, Y.-M. Chiang, Aliovalent Doping for Improved Battery Performance: Aliovalent Substitutions in Olivine Lithium Iron Phosphate and Impact on Structure and Properties. , *Advanced Functional Materials*, **19** (2009) 1060.

[25] S.-Y. Chung, J.T. Bloking, Y.-M. Chiang, Electronically conductive phospho-olivines as lithium storage electrodes, *Nat Mater*, **1** (2002) 123.

[26] J.F. Ni, H.H. Zhou, J.T. Chen, X.X. Zhang, $LiFePO_4$ doped with ions prepared by co-precipitation method, *Materials Letters*, **59** (2005) 2361.

[27] G.X. Wang, S. Needham, J. Yao, J.Z. Wang, R.S. Liu, H.K. Liu, A study on $LiFePO_4$ and its doped derivatives as cathode materials for lithium-ion batteries, *Journal of Power Sources*, **159** (2006) 282.

[28] H.C. Shin, W.I. Cho, H. Jang, Electrochemical properties of carbon-coated $LiFePO_4$ cathode using graphite, carbon black, and acetylene black, *Electrochimica Acta*, **52** (2006) 1472.

[29] M.M. Doeff, J.D. Wilcox, R. Kostecki, G. Lau, Optimization of carbon coatings on $LiFePO_4$, *Journal of Power Sources*, **163** (2006) 180.

[30] S.-T. Myung, S. Komaba, N. Hirosaki, H. Yashiro, N. Kumagai, Emulsion drying synthesis of olivine $LiFePO_4$/C composite and its electrochemical properties as lithium intercalation material, *Electrochimica Acta*, **49** (2004) 4213.

[31] T. Nakamura, Y. Miwa, M. Tabuchi, Y. Yamada, Structural and Surface Modifications of $LiFePO_4$ Olivine Particles and Their Electrochemical Properties, *Journal of the Electrochemical Society*, **153** (2006) A1108.

[32] Y. Lin, M.X. Gao, D. Zhu, Y.F. Liu, H.G. Pan, Effects of carbon coating and iron phosphides on the electrochemical properties of $LiFePO_4$/C, *Journal of Power Sources*, **184** (2008) 444.

[33] J. Wang, X. Sun, Understanding and recent development of carbon coating on $LiFePO_4$ cathode materials for lithium-ion batteries, *Energy & Environmental Science*, **5** (2012) 5163.

[34] Z. Chen, J.R. Dahn, Reducing Carbon in $LiFePO_4$ / C Composite Electrodes to Maximize Specific Energy, Volumetric Energy, and Tap Density, *Journal of The Electrochemical Society*, **149** (2002) A1184.

[35] M. Doeff, J. Wilcox, R. Yu, A. Aumentado, M. Marcinek, R. Kostecki, Impact of carbon structure and morphology on the electrochemical performance of $LiFePO_4$/C composites, *Journal of Solid State Electrochemistry*, **12** (2008) 995.

[36] Y. Kadoma, J.-M. Kim, K. Abiko, K. Ohtsuki, K. Ui, N. Kumagai, Optimization of electrochemical properties of $LiFePO_4$/C prepared by an aqueous solution method using sucrose, *Electrochimica Acta*, **55** (2010) 1034.

[37] Y.-H. Nien, J.R. Carey, J.-S. Chen, Physical and electrochemical properties of $LiFePO_4$/C composite cathode prepared from various polymer-containing precursors, *Journal of Power Sources*, **193** (2009) 822.

[38] G. Liang, L. Wang, X. Ou, X. Zhao, S. Xu, Lithium iron phosphate with high-rate capability synthesized through hydrothermal reaction in glucose solution, *Journal of Power Sources*, **184** (2008) 538.

[39] M.M. Doeff, Y. Hu, F. McLarnon, R. Kostecki, Effect of Surface Carbon Structure on the Electrochemical Performance of $LiFePO_4$, *Electrochemical and Solid-State Letters*, **6** (2003) A207.

[40] Y.-D. Cho, G.T.-K. Fey, H.-M. Kao, The effect of carbon coating thickness on the capacity of $LiFePO_4$/C composite cathodes, *Journal of Power Sources*, **189** (2009) 256.

[41] L. Zhang, H. Xiang, X. Zhu, W. Yang, H. Wang, Synthesis of $LiFePO_4$/C composite as a cathode material for lithium-ion battery by a novel two-step method, *Journal of Materials Science*, **47** (2012) 3076.

[42] W. Peng, L. Jiao, H. Gao, Z. Qi, Q. Wang, H. Du, Y. Si, Y. Wang, H. Yuan, A novel sol-gel method based on $FePO_4 \cdot 2H_2O$ to synthesize submicrometer structured $LiFePO_4$/C cathode material, *Journal of Power Sources*, **196** (2011) 2841.

[43] J. Moskon, R. Dominko, R. Cerc-Korosec, M. Gaberscek, J. Jamnik, Morphology and electrical properties of conductive carbon coatings for cathode materials, *Journal of Power Sources*, **174** (2007) 683.

[44] A. Awarke, S. Lauer, S. Pischinger, M. Wittler, Percolation–tunneling modeling for the study of the electric conductivity in $LiFePO_4$ based Li-ion battery cathodes, *Journal of Power Sources*, **196** (2011) 405.

[45] R. Dominko, M. Bele, M. Gaberscek, M. Remskar, D. Hanzel, S. Pejovnik, J. Jamnik, Impact of the Carbon Coating Thickness on the Electrochemical Performance of $LiFePO_4$ / C Composites, *Journal of The Electrochemical Society*, **152** (2005) A607.

[46] B.L. Ellis, M. Wagemaker, F.M. Mulder, L.F. Nazar, Comment on "Aliovalent Substitutions in Olivine Lithium Iron Phosphate and Impact on Structure and Properties", *Advanced Functional Materials*, **20** (2010) 186.

[47] P.S. Herle, B. Ellis, N. Coombs, L.F. Nazar, Nano-network electronic conduction in iron and nickel olivine phosphates, *Nat Mater*, **3** (2004) 147.

[48] G.X. Wang, S.L. Bewlay, K. Konstantinov, H.K. Liu, S.X. Dou, J.H. Ahn, Physical and electrochemical properties of doped lithium iron phosphate electrodes, *Electrochimica Acta*, **50** (2004) 443.

[49] H.C. Shin, S.B. Park, H. Jang, K.Y. Chung, W.I. Cho, C.S. Kim, B.W. Cho, Rate performance and structural change of Cr-doped $LiFePO_4$/C during cycling, *Electrochimica Acta*, **53** (2008) 7946.

[50] T.-H. Teng, M.-R. Yang, S.-h. Wu, Y.-P. Chiang, Electrochemical properties of $LiFe_{0.9}Mg_{0.1}PO_4$ / carbon cathode materials prepared by ultrasonic spray pyrolysis, *Solid State Communications*, **142** (2007) 389.

[51] C.S. Sun, Z. Zhou, Z.G. Xu, D.G. Wang, J.P. Wei, X.K. Bian, J. Yan, Improved high-rate charge/discharge performances of $LiFePO_4$/C via V-doping, *Journal of Power Sources*, **193** (2009) 841.

[52] R. Amin, C. Lin, J. Maier, Aluminium-doped LiFePO4 single crystals Part I. Growth, characterization and total conductivity, *Physical Chemistry Chemical Physics*, **10** (2008) 3519.

[53] M. Wagemaker, B.L. Ellis, D. Lützenkirchen-Hecht, F.M. Mulder, L.F. Nazar, Proof of Supervalent Doping in Olivine $LiFePO_4$, *Chemistry of Materials*, **20** (2008) 6313.

[54] C.A.J. Fisher, V.M. Hart Prieto, M.S. Islam, Lithium Battery Materials $LiMPO_4$ (M = Mn, Fe, Co, and Ni): Insights into Defect Association, Transport Mechanisms, and Doping Behavior, *Chemistry of Materials*, **20** (2008) 5907.

[55] L. Wang, H. Wang, Z. Liu, C. Xiao, S. Dong, P. Han, Z. Zhang, X. Zhang, C. Bi, G. Cui, A facile method of preparing mixed conducting $LiFePO_4$/graphene composites for lithium-ion batteries, *Solid State Ionics*, **181** (2010) 1685.

[56] J. Hong, F. Wang, X. Wang, J. Graetz, $LiFe_xMn_{1-x}PO_4$: A cathode for lithium-ion batteries, *Journal of Power Sources*, **196** (2011) 3659.

[57] S.-M. Oh, H.-G. Jung, C.S. Yoon, S.-T. Myung, Z. Chen, K. Amine, Y.-K. Sun, Enhanced electrochemical performance of carbon–$LiMn_{1-x}Fe_xPO_4$ nanocomposite cathode for lithium-ion batteries, *Journal of Power Sources*, **196** (2011) 6924.

[58] B. Zhang, X. Wang, H. Li, X. Huang, Electrochemical performances of $LiFe_{1-x}Mn_xPO_4$ with high Mn content, *Journal of Power Sources*, **196** (2011) 6992.

[59] Y. Wang, D. Zhang, X. Yu, R. Cai, Z. Shao, X.-Z. Liao, Z.-F. Ma, Mechanoactivation-assisted synthesis and electrochemical characterization of manganese lightly doped $LiFePO_4$, *Journal of Alloys and Compounds*, **492** (2010) 675.

[60] A. Yamada, Y. Kudo, K.-Y. Liu, Reaction Mechanism of the Olivine-Type $Li_x(Mn_{0.6}Fe_{0.4})PO_4$ $(0 \leqslant x \leqslant 1)$ *Journal of The Electrochemical Society*, **148** (2001) A747.

[61] M. Bini, M.C. Mozzati, P. Galinetto, D. Capsoni, S. Ferrari, M.S. Grandi, V. Massarotti, Structural, spectroscopic and magnetic investigation of the $LiFe_{1-x}Mn_xPO_4$ (x=0–0.18) solid solution, *Journal of Solid State Chemistry*, **182** (2009) 1972.

[62] T. Nakamura, K. Sakumoto, M. Okamoto, S. Seki, Y. Kobayashi, T. Takeuchi, M. Tabuchi, Y. Yamada, Electrochemical study on Mn^{2+}-substitution in $LiFePO_4$ olivine compound, *Journal of Power Sources*, **174** (2007) 435.

[63] C.H. Mi, X.G. Zhang, X.B. Zhao, H.L. Li, Synthesis and performance of $LiMn_{0.6}Fe_{0.4}PO_4$/nano-carbon webs composite cathode, *Materials Science and Engineering: B*, **129** (2006) 8.

[64] Y. Lin, B. Zeng, Y. Lin, X. Li, G. Zhao, T. Zhou, H. Lai, Z. Huang, Electrochemical properties of carbon-coated $LiFePO_4$ and $LiFe_{0.98}Mn_{0.02}PO_4$ cathode materials synthesized by solid-state reaction, *Rare Metals*, **31** (2012) 145.

[65] S.K. Martha, J. Grinblat, O. Haik, E. Zinigrad, T. Drezen, J.H. Miners, I. Exnar, A. Kay, B. Markovsky, D. Aurbach, $LiMn_{0.8}Fe_{0.2}PO_4$: An Advanced Cathode Material for Rechargeable Lithium Batteries, *Angewandte Chemie International Edition*, **48** (2009) 8559.

[66] T. Honma, K. Nagamine, T. Komatsu, Fabrication of olivine-type $LiMn_xFe_{1-x}PO_4$ crystals via the glass–ceramic route and their lithium ion battery performance, *Ceramics International*, **36** (2010) 1137.

[67] J.-K. Kim, G.S. Chauhan, J.-H. Ahn, H.-J. Ahn, Effect of synthetic conditions on the electrochemical properties of $LiMn_{0.4}Fe_{0.6}PO_4$/C synthesized by sol–gel technique, *Journal of Power Sources*, **189** (2009) 391.

[68] J. Yao, S. Bewlay, K. Konstantionv, V.A. Drozd, R.S. Liu, X.L. Wang, H.K. Liu, G.X. Wang, Characterisation of olivine-type $LiMn_xFe_{1-x}PO_4$ cathode materials, *Journal of Alloys and Compounds*, **425** (2006) 362.

[69] R.-R. Zhao, B.-Y. Lan, H.-Y. Chen, G.-Z. Ma, Hydrothermal synthesis and properties of manganese-doped $LiFePO_4$, *Ionics*, **18** (2012) 873.

[70] K.T. Lee, K.S. Lee, Electrochemical properties of $LiFe_{0.9}Mn_{0.1}PO_4/Fe_2P$ cathode material by mechanical alloying, *Journal of Power Sources*, **189** (2009) 435.

[71] D.-H. Baek, J.-K. Kim, Y.-J. Shin, G.S. Chauhan, J.-H. Ahn, K.-W. Kim, Effect of firing temperature on the electrochemical performance of $LiMn_{0.4}Fe_{0.6}PO_4$/C materials prepared by mechanical activation, *Journal of Power Sources*, **189** (2009) 59.

[72] O. Toprakci, L. Ji, Z. Lin, H.A.K. Toprakci, X. Zhang, Fabrication and electrochemical characteristics of electrospun $LiFePO_4$/carbon composite fibers for lithium-ion batteries, *Journal of Power Sources*, **196** (2011) 7692.

[73] G. Li, H. Azuma, M. Tohda Optimized $LiMn_yFe_{1-y}PO_4$ as the Cathode for Lithium Batteries, *Journal of The Electrochemical Society*, **149** (2002) A743.

[74] Y. Xu, J. Yu, S. Peng, S. Liu, Z. Wei, X. Li, Y. Li, Preparation and electrochemical properties of homogeneous carbon-coated $LiFe_{0.9}Mn_{0.1}PO_4$ as cathode material for lithium-ion batteries, *Journal of the Brazilian Chemical Society*, **23** (2012) 1298.

[75] B. Zhang, X. Wang, Z. Liu, H. Li, X. Huang, Enhanced Electrochemical Performances of Carbon Coated Mesoporous $LiFe_{0.2}Mn_{0.8}PO_4$, *Journal of The Electrochemical Society*, **157** (2010) A285.

[76] B.Z. Li, Y. Wang, L. Xue, X.P. Li, W.S. Li, Acetylene black-embedded $LiMn_{0.8}Fe_{0.2}PO_4$/C composite as cathode for lithium ion battery, *Journal of Power Sources*, **232** (2013) 12.

[77] S. Yang, P.Y. Zavalij, M. Stanley Whittingham, Hydrothermal synthesis of lithium iron phosphate cathodes, *Electrochemistry Communications*, **3** (2001) 505.

[78] S. Yang, Y. Song, P.Y. Zavalij, M. Stanley Whittingham, Reactivity, stability and electrochemical behavior of lithium iron phosphates, *Electrochemistry Communications*, **4** (2002) 239.

[79] J. Chen, M.S. Whittingham, Hydrothermal synthesis of lithium iron phosphate, *Electrochemistry Communications*, **8** (2006) 855.

[80] J. Chen, S. Wang, M.S. Whittingham, Hydrothermal synthesis of cathode materials, *Journal of Power Sources*, **174** (2007) 442.

[81] B. Jin, H.-B. Gu, Preparation and characterization of $LiFePO_4$ cathode materials by hydrothermal method, *Solid State Ionics*, **178** (2008) 1907.

[82] G. Meligrana, C. Gerbaldi, A. Tuel, S. Bodoardo, N. Penazzi, Hydrothermal synthesis of high surface $LiFePO_4$ powders as cathode for Li-ion cells, *Journal of Power Sources*, **160** (2006) 516.

[83] S. Bodoardo, C. Gerbaldi, G. Meligrana, A. Tuel, S. Enzo, N. Penazzi, Optimisation of some parameters for the preparation of nanostructured $LiFePO_4$/C cathode, *Ionics*, **15** (2009) 19.

[84] K. Shiraishi, K. Dokko, K. Kanamura, Formation of impurities on phospho-olivine LiFePO4 during hydrothermal synthesis, *Journal of Power Sources*, **146** (2005) 555.

[85] S. Franger, F. Le Cras, C. Bourbon, H. Rouault, Comparison between different $LiFePO_4$ synthesis routes and their influence on its physico-chemical properties, *Journal of Power Sources*, **119–121** (2003) 252.

[86] S. Tajimi, Y. Ikeda, K. Uematsu, K. Toda, M. Sato, Enhanced electrochemical performance of $LiFePO_4$ prepared by hydrothermal reaction, *Solid State Ionics*, **175** (2004) 287.

[87] J. Lee, A.S. Teja, Synthesis of $LiFePO_4$ micro and nanoparticles in supercritical water, *Materials Letters*, **60** (2006) 2105.

[88] C. Xu, J. Lee, A.S. Teja, Continuous hydrothermal synthesis of lithium iron phosphate particles in subcritical and supercritical water, *The Journal of Supercritical Fluids*, **44** (2008) 92.

[89] L.L. Hench, J.K. West, The sol-gel process, *Chemical Reviews*, **90** (1990) 33.

[90] R. Dominko, M. Bele, M. Gaberscek, M. Remskar, D. Hanzel, J.M. Goupil, S. Pejovnik, J. Jamnik, Porous olivine composites synthesized by sol–gel technique, *Journal of Power Sources*, **153** (2006) 274.

[91] J.-K. Kim, G. Cheruvally, J.-H. Ahn, G.-C. Hwang, J.-B. Choi, Electrochemical properties of carbon-coated $LiFePO_4$ synthesized by a modified mechanical activation process, *Journal of Physics and Chemistry of Solids*, **69** (2008) 2371.

[92] R. Dominko, J.M. Goupil, M. Bele, M. Gaberscek, M. Remskar, D. Hanzel, J. Jamnik, Impact of $LiFePO_4$/C Composites Porosity on Their Electrochemical Performance, *Journal of The Electrochemical Society*, **152** (2005) A858.

[93] K.-F. Hsu, S.-Y. Tsay, B.-J. Hwang, Physical and electrochemical properties of $LiFePO_4$/carbon composite synthesized at various pyrolysis periods, *Journal of Power Sources*, **146** (2005) 529.

[94] J. Yang, J.J. Xu, Nonaqueous Sol-Gel Synthesis of High-Performance $LiFePO_4$, *Electrochemical and Solid-State Letters*, **7** (2004) A515.

[95] D. Choi, P.N. Kumta, Surfactant based sol–gel approach to nanostructured $LiFePO_4$ for high rate Li-ion batteries, *Journal of Power Sources*, **163** (2007) 1064.

[96] C. Julien, A. Mauger, A. Ait-Salah, M. Massot, F. Gendron, K. Zaghib, Nanoscopic scale studies of $LiFePO_4$ as cathode material in lithium-ion batteries for HEV application, *Ionics*, **13** (2007) 395.

[97] N. Iltchev, Y. Chen, S. Okada, J.-i. Yamaki, $LiFePO_4$ storage at room and elevated temperatures, *Journal of Power Sources*, **119–121** (2003) 749.

[98] A.A. Salah, A. Mauger, C.M. Julien, F. Gendron, Nano-sized impurity phases in relation to the mode of preparation of $LiFePO_4$, *Materials Science and Engineering: B*, **129** (2006) 232.

[99] F. Croce, A. D' Epifanio, J. Hassoun, A. Deptula, T. Olczac, B. Scrosati, A Novel Concept for the Synthesis of an Improved $LiFePO_4$ Lithium Battery Cathode, *Electrochemical and Solid-State Letters*, **5** (2002) A47.

[100] C.R. Sides, F. Croce, V.Y. Young, C.R. Martin, B. Scrosati, A High-Rate, Nanocomposite $LiFePO_4$/Carbon Cathode, *Electrochemical and Solid-State Letters*, **8** (2005) A484.

[101] M. Koltypin, D. Aurbach, L. Nazar, B. Ellis, More on the performance of $LiFePO_4$ electrodes—The effect of synthesis route, solution composition, aging, and temperature, *Journal of Power Sources*, **174** (2007) 1241.

[102] K.-F. Hsu, S.-Y. Tsay, B.-J. Hwang, Synthesis and characterization of nano-sized $LiFePO_4$ cathode materials prepared by a citric acid-based sol-gel route, *Journal of Materials Chemistry*, **14** (2004) 2690.

[103] J.-K. Kim, J.-W. Choi, G.S. Chauhan, J.-H. Ahn, G.-C. Hwang, J.-B. Choi, H.-J. Ahn, Enhancement of electrochemical performance of lithium iron phosphate by controlled sol-gel synthesis, *Electrochimica Acta*, **53** (2008) 8258.

[104] K.S. Park, K.T. Kang, S.B. Lee, G.Y. Kim, Y.J. Park, H.G. Kim, Synthesis of $LiFePO_4$ with fine particle by co-precipitation method, *Materials Research Bulletin*, **39** (2004) 1803.

[105] P. Gibot, M. Casas-Cabanas, L. Laffont, S. Levasseur, P. Carlach, S. Hamelet, J.-M. Tarascon, C. Masquelier, Room-temperature single-phase Li insertion/extraction in nanoscale Li_xFePO_4, *Nat Mater*, **7** (2008) 741.

[106] Z.-R. Chang, H.-J. Lv, H.-W. Tang, H.-J. Li, X.-Z. Yuan, H. Wang, Synthesis and characterization of high-density $LiFePO_4$/C composites as cathode materials for lithium-ion batteries, *Electrochimica Acta*, **54** (2009) 4595.

[107] Y. Xu, Y. Lu, P. Yin, L. Yan, Z. Yang, R. Yang, A versatile method for preparing $FePO_4$ and study on its electrode performance in lithium ion batteries, *Journal of Materials Processing Technology*, **204** (2008) 513.

[108] J.-c. Zheng, X.-h. Li, Z.-x. Wang, H.-j. Guo, S.-y. Zhou, $LiFePO_4$ with enhanced performance synthesized by a novel synthetic route, *Journal of Power Sources*, **184** (2008) 574.

[109] M.-H. Lee, J.-Y. Kim, H.-K. Song, A hollow sphere secondary structure of $LiFePO_4$ nanoparticles, *Chemical Communications*, **46** (2010) 6795.

[110] Y. Lan, X. Wang, J. Zhang, J. Zhang, Z. Wu, Z. Zhang, Preparation and characterization of carbon-coated $LiFePO_4$ cathode materials for lithium-ion batteries with resorcinol–formaldehyde polymer as carbon precursor, *Powder Technology*, **212** (2011) 327.

[111] P.P. Prosini, M. Carewska, S. Scaccia, P. Wisniewski, S. Passerini, M. Pasquali, A New Synthetic Route for Preparing $LiFePO_4$ with Enhanced Electrochemical Performance, *Journal of The Electrochemical Society*, **149** (2002) A886.

[112] G. Arnold, J. Garche, R. Hemmer, S. Ströbele, C. Vogler, M. Wohlfahrt-Mehrens, Fine-particle lithium iron phosphate $LiFePO_4$ synthesized by a new low-cost aqueous precipitation technique, *Journal of Power Sources*, **119–121** (2003) 247.

[113] D. Jugovic, M. Mitric, N. Cvjeticanin, B. Jancar, S. Mentus, D. Uskokovic, Synthesis and characterization of $LiFePO_4$/C composite obtained by sonochemical method, *Solid State Ionics*, **179** (2008) 415.

[114] G. Kobayashi, S.-i. Nishimura, M.-S. Park, R. Kanno, M. Yashima, T. Ida, A. Yamada, Isolation of Solid Solution Phases in Size-Controlled Li_xFePO_4 at Room Temperature, *Advanced Functional Materials*, **19** (2009) 395.

[115] A. Yamada, S.C. Chung, K. Hinokuma Optimized $LiFePO_4$ for Lithium Battery Cathodes, *Journal of the Electrochemical Society*, **148** (2001) A224.

[116] H.-C. Kang, D.-K. Jun, B. Jin, E.M. Jin, K.-H. Park, H.-B. Gu, K.-W. Kim, Optimized solid-state synthesis of $LiFePO_4$ cathode materials using ball-milling, *Journal of Power Sources*, **179** (2008) 340.

[117] C. Lai, Q. Xu, H. Ge, G. Zhou, J. Xie, Improved electrochemical performance of $LiFePO_4$/C for lithium-ion batteries with two kinds of carbon sources, *Solid State Ionics*, **179** (2008) 1736.

[118] A. Ait Salah, A. Mauger, K. Zaghib, J.B. Goodenough, N. Ravet, M. Gauthier, F. Gendron, C.M. Julien, Reduction Fe^{3+} of Impurities in $LiFePO_4$ from Pyrolysis of Organic

Precursor Used for Carbon Deposition, *Journal of The Electrochemical Society*, **153** (2006) A1692.

[119] K. Zaghib, A. Mauger, F. Gendron, C. Julien, Relationship between local structure and electrochemical performance of $LiFePO_4$ in Li-ion batteries, *Ionics*, **14** (2008) 271.

[120] G.T.-K. Fey, T.-L. Lu, Morphological characterization of $LiFePO_4$/C composite cathode materials synthesized via a carboxylic acid route, *Journal of Power Sources*, **178** (2008) 807.

[121] C.M. Julien, K. Zaghib, A. Mauger, M. Massot, A. Ait-Salah, M. Selmane, F. Gendron, Characterization of the carbon coating onto $LiFePO_4$ particles used in lithium batteries, *Journal of Applied Physics*, **100** (2006).

[122] C.H. Mi, G.S. Cao, X.B. Zhao, Low-cost, one-step process for synthesis of carbon-coated $LiFePO_4$ cathode, *Materials Letters*, **59** (2005) 127.

[123] Y. Wang, Z. Liu, S. Zhou, An effective method for preparing uniform carbon coated nano-sized $LiFePO_4$ particles, *Electrochimica Acta*, **58** (2011) 359.

[124] B. Zhao, Y. Jiang, H. Zhang, H. Tao, M. Zhong, Z. Jiao, Morphology and electrical properties of carbon coated $LiFePO_4$ cathode materials, *Journal of Power Sources*, **189** (2009) 462.

[125] C.H. Mi, X.G. Zhang, X.B. Zhao, H.L. Li, Effect of sintering time on the physical and electrochemical properties of $LiFePO_4$/C composite cathodes, *Journal of Alloys and Compounds*, **424** (2006) 327.

[126] F. Cheng, W. Wan, Z. Tan, Y. Huang, H. Zhou, J. Chen, X. Zhang, High power performance of nano-$LiFePO_4$/C cathode material synthesized via lauric acid-assisted solid-state reaction, *Electrochimica Acta*, **56** (2011) 2999.

[127] N. Lyczko, A. Nzihou, P. Sharrock, A. Germeau, C. Toussaint, Characterization of $LiFePO_4$/C cathode for lithium ion batteries, *Industrial and Engineering Chemistry Research*, **51** (2012) 292.

[128] Y. Xia, M. Yoshio, H. Noguchi, Improved electrochemical performance of $LiFePO_4$ by increasing its specific surface area, *Electrochimica Acta*, **52** (2006) 240.

[129] J. Barker, M.Y. Saidi, J.L. Swoyer Lithium Iron(II) Phospho-olivines Prepared by a Novel Carbothermal Reduction Method, *Electrochemical and Solid-State Letters*, **6** (2003) A53.

[130] H.-p. Liu, Z.-x. Wang, X.-h. Li, H.-j. Guo, W.-j. Peng, Y.-h. Zhang, Q.-y. Hu, Synthesis and electrochemical properties of olivine $LiFePO_4$ prepared by a carbothermal reduction method, *Journal of Power Sources*, **184** (2008) 469.

[131] H. Liu, P. Zhang, G. Li, Q. Wu, Y. Wu, $LiFePO_4$/C composites from carbothermal reduction method, *Journal of Solid State Electrochemistry*, **12** (2008) 1011.

[132] F. Yu, J. Zhang, Y. Yang, G. Song, Reaction mechanism and electrochemical performance of $LiFePO_4$/C cathode materials synthesized by carbothermal method, *Electrochimica Acta*, **54** (2009) 7389.

[133] L. Yang, G. Liang, L. Wang, X. Zhi, X. Ou, Synthesis and Characterization of $LiFePO_4$/C Composite Obtained by One-Step Solid-State Reaction Using Solid PVA as Carbon Source, *MRS Online Proceedings Library*, **1170** (2009).

[134] L. Wang, G.C. Liang, X.Q. Ou, X.K. Zhi, J.P. Zhang, J.Y. Cui, Effect of synthesis temperature on the properties of $LiFePO_4$/C composites prepared by carbothermal reduction, *Journal of Power Sources*, **189** (2009) 423.

[135] M.E. Zhong, Z.T. Zhou, Preparation of high tap-density $LiFePO_4$/C composite cathode materials by carbothermal reduction method using two kinds of Fe^{3+} precursors, *Materials Chemistry and Physics*, **119** (2010) 428.

[136] K. Zaghib, A. Mauger, F. Gendron, C.M. Julien, Surface Effects on the Physical and Electrochemical Properties of Thin $LiFePO_4$ Particles, *Chemistry of Materials*, **20** (2007) 462.

[137] M. Konarova, I. Taniguchi, Preparation of carbon coated $LiFePO_4$ by a combination of spray pyrolysis with planetary ball-milling followed by heat treatment and their electrochemical properties, *Powder Technology*, **191** (2009) 111.

[138] J.-K. Kim, G. Cheruvally, J.-W. Choi, J.-U. Kim, J.-H. Ahn, G.-B. Cho, K.-W. Kim, H.-J. Ahn, Effect of mechanical activation process parameters on the properties of $LiFePO_4$ cathode material, *Journal of Power Sources*, **166** (2007) 211.

[139] J.-K. Kim, J.-W. Choi, G. Cheruvally, J.-U. Kim, J.-H. Ahn, G.-B. Cho, K.-W. Kim, H.-J. Ahn, A modified mechanical activation synthesis for carbon-coated $LiFePO_4$ cathode in lithium batteries, *Materials Letters*, **61** (2007) 3822.

[140] K. Wang, R. Cai, T. Yuan, X. Yu, R. Ran, Z. Shao, Process investigation, electrochemical characterization and optimization of $LiFePO_4$/C composite from mechanical activation using sucrose as carbon source, *Electrochimica Acta*, **54** (2009) 2861.

[141] G.T.-K. Fey, Y.G. Chen, H.-M. Kao, Electrochemical properties of $LiFePO_4$ prepared via ball-milling, *Journal of Power Sources*, **189** (2009) 169.

[142] S.J. Kwon, C.W. Kim, W.T. Jeong, K.S. Lee, Synthesis and electrochemical properties of olivine $LiFePO_4$ as a cathode material prepared by mechanical alloying, *Journal of Power Sources*, **137** (2004) 93.

[143] N. Kosova, E. Devyatkina, On mechanochemical preparation of materials with enhanced characteristics for lithium batteries, *Solid State Ionics*, **172** (2004) 181.

[144] C.W. Kim, M.H. Lee, W.T. Jeong, K.S. Lee, Synthesis of olivine $LiFePO_4$ cathode materials by mechanical alloying using iron(III) raw material, *Journal of Power Sources*, **146** (2005) 534.

[145] C.H. Mi, X.G. Zhang, H.L. Li, Electrochemical behaviors of solid $LiFePO_4$ and $Li_{0.99}Nb_{0.01}FePO_4$ in Li_2SO_4 aqueous electrolyte, *Journal of Electroanalytical Chemistry*, **602** (2007) 245.

[146] M. Higuchi, K. Katayama, Y. Azuma, M. Yukawa, M. Suhara, Synthesis of $LiFePO_4$ cathode material by microwave processing, *Journal of Power Sources*, **119–121** (2003) 258.

[147] K.S. Park, J.T. Son, H.T. Chung, S.J. Kim, C.H. Lee, H.G. Kim, Synthesis of $LiFePO_4$ by co-precipitation and microwave heating, *Electrochemistry Communications*, **5** (2003) 839.

[148] B. Ellis, W.H. Kan, W.R.M. Makahnouk, L.F. Nazar, Synthesis of nanocrystals and morphology control of hydrothermally prepared $LiFePO_4$, *Journal of Materials Chemistry*, **17** (2007) 3248.

[149] M.-S. Song, Y.-M. Kang, Y.-I. Kim, K.-S. Park, H.-S. Kwon, Nature of Insulating-Phase Transition and Degradation of Structure and Electrochemical Reactivity in an Olivine-Structured Material, $LiFePO_4$, *Inorganic Chemistry*, **48** (2009) 8271.

[150] Y. Zhang, H. Feng, X. Wu, L. Wang, A. Zhang, T. Xia, H. Dong, M. Liu, One-step microwave synthesis and characterization of carbon-modified nanocrystalline $LiFePO_4$, *Electrochimica Acta*, **54** (2009) 3206.

[151] M. Konarova, I. Taniguchi, Synthesis of carbon-coated $LiFePO_4$ nanoparticles with high rate performance in lithium secondary batteries, *Journal of Power Sources*, **195** (2010) 3661.

[152] S. Akao, M. Yamada, T. Kodera, T. Ogihara, Mass Production of $LiFePO_4$/C Powders by Large Type Spray Pyrolysis Apparatus and Its Application to Cathode for Lithium Ion Battery, *International Journal of Chemical Engineering*, **2010** (2010) 1.

[153] J. Liu, T.E. Conry, X. Song, M.M. Doeff, T.J. Richardson, Nanoporous spherical $LiFePO_4$ for high performance cathodes, *Energy & Environmental Science*, **4** (2011) 885.

[154] F. Gao, Z. Tang, J. Xue, Preparation and characterization of nano-particle $LiFePO_4$ and LiFePO4/C by spray-drying and post-annealing method, *Electrochimica Acta*, **53** (2007) 1939.

[155] M. Konarova, I. Taniguchi, Physical and electrochemical properties of $LiFePO_4$ nanoparticles synthesized by a combination of spray pyrolysis with wet ball-milling, *Journal of Power Sources*, **194** (2009) 1029.

[156] M.-R. Yang, T.-H. Teng, S.-H. Wu, $LiFePO_4$/carbon cathode materials prepared by ultrasonic spray pyrolysis, *Journal of Power Sources*, **159** (2006) 307.

[157] S.L. Bewlay, K. Konstantinov, G.X. Wang, S.X. Dou, H.K. Liu, Conductivity improvements to spray-produced $LiFePO_4$ by addition of a carbon source, *Materials Letters*, **58** (2004) 1788.

[158] S. Ping Ong, L. Wang, B. Kang, G. Ceder, Li−Fe−P−O2 Phase Diagram from First Principles Calculations, *Chemistry of Materials*, **20** (2008) 1798.

[159] O. Waser, R. Büchel, A. Hintennach, P. Novák, S.E. Pratsinis, Continuous flame aerosol synthesis of carbon-coated nano-$LiFePO_4$ for Li-ion batteries, *Journal of Aerosol Science*, **42** (2011) 657.

[160] H. Liu, D. Tang, The low cost synthesis of nanoparticles $LiFePO_4$/C composite for lithium rechargeable batteries, *Solid State Ionics*, **179** (2008) 1897.

[161] L.N. Wang, X.C. Zhan, Z.G. Zhang, K.L. Zhang, A soft chemistry synthesis routine for $LiFePO_4$-C using a novel carbon source, *Journal of Alloys and Compounds*, **456** (2008) 461.

[162] H. Liu, Y. Feng, Z. Wang, K. Wang, J. Xie, A PVB-based rheological phase approach to nano-$LiFePO_4$/C composite cathodes, *Powder Technology*, **184** (2008) 313.

[163] Y. Huang, H. Ren, S. Yin, Y. Wang, Z. Peng, Y. Zhou, Synthesis of $LiFePO_4$/C composite with high-rate performance by starch sol assisted rheological phase method, *Journal of Power Sources*, **195** (2010) 610.

[164] H.-J. Kim, J.-M. Kim, W.-S. Kim, H.-J. Koo, D.-S. Bae, H.-S. Kim, Synthesis of $LiFePO_4$/C cathode materials through an ultrasonic-assisted rheological phase method, *Journal of Alloys and Compounds*, **509** (2011) 5662.

[165] M. Wang, Y. Xue, K. Zhang, Y. Zhang, Synthesis of $FePO_4 \cdot 2H_2O$ nanoplates and their usage for fabricating superior high-rate performance $LiFePO_4$, *Electrochimica Acta*, **56** (2011) 4294.

[166] J. Dou, X. Kang, T. Wumaier, N. Hua, Y. Han, G. Xu, Oxalic acid-assisted preparation of $LiFePO_4$/C cathode material for lithium-ion batteries, *Journal of Solid State Electrochemistry*, **16** (2011) 1925.

[167] V. Palomares, A. Goñi, I.G.d. Muro, I. de Meatza, M. Bengoechea, O. Miguel, T. Rojo, New freeze-drying method for $LiFePO_4$ synthesis, *Journal of Power Sources*, **171** (2007) 879.

[168] V. Palomares, A. Goñi, I.G.d. Muro, I. de Meatza, M. Bengoechea, I. Cantero, T. Rojo, Conductive additive content balance in Li-ion battery cathodes: Commercial carbon blacks vs. in situ carbon from $LiFePO_4$/C composites, *Journal of Power Sources*, **195** (2010) 7661.

[169] V. Palomares, A. Goñi, A. Iturrondobeitia, L. Lezama, I. De Meatza, M. Bengoechea, T. Rojo, Structural, magnetic and electrochemical study of a new active phase obtained by oxidation of a LiFePO $_4$/C composite, *Journal of Materials Chemistry*, **22** (2012) 4735.

[170] J. Orlenius, O. Lyckfeldt, K.A. Kasvayee, P. Johander, Water based processing of $LiFePO_4$/C cathode material for Li-ion batteries utilizing freeze granulation, *Journal of Power Sources*, **213** (2012) 119.

[171] X. Xi, G. Chen, Z. Nie, S. He, X. Pi, X. Zhu, J. Zhu, T. Zuo, Preparation and performance of LiFePO4 and $LiFePO_4$/C cathodes by freeze-drying, *Journal of Alloys and Compounds*, **497** (2010) 377.

[172] I. Boyano, J.A. Blazquez, I. de Meatza, M. Bengoechea, O. Miguel, H. Grande, Y. Huang, J.B. Goodenough, Preparation of C-$LiFePO_4$/polypyrrole lithium rechargeable cathode by consecutive potential steps electrodeposition, *Journal of Power Sources*, **195** (2010) 5351.

[173] T. Honma, K. Hirose, T. Komatsu, T. Sato, S. Marukane, Fabrication of $LiFePO_4$/carbon composites by glass powder crystallization processing and their battery performance, *Journal of Non-Crystalline Solids*, **356** (2010) 3032.

[174] L. Dimesso, C. Spanheimer, S. Jacke, W. Jaegermann, Synthesis and characterization of three-dimensional carbon foams-$LiFePO_4$ composites, *Journal of Power Sources*, **196** (2011) 6729.

[175] D.-H. Kim, J. Kim, Synthesis of $LiFePO_4$ Nanoparticles in Polyol Medium and Their Electrochemical Properties, *Electrochemical and Solid-State Letters*, **9** (2006) A439.

[176] B.-J. Hwang, K.-F. Hsu, S.-K. Hu, M.-Y. Cheng, T.-C. Chou, S.-Y. Tsay, R. Santhanam, Template-free reverse micelle process for the synthesis of a rod-like $LiFePO_4$/C composite cathode material for lithium batteries, *Journal of Power Sources*, **194** (2009) 515.

[177] Y. Wang, Y. Wang, E. Hosono, K. Wang, H. Zhou, The Design of a $LiFePO_4$/Carbon Nanocomposite With a Core–Shell Structure and Its Synthesis by an In Situ Polymerization Restriction Method, *Angewandte Chemie International Edition*, **47** (2008) 7461.

[178] S. Luo, Z. Tang, J. Lu, Z. Zhang, Electrochemical properties of carbon-mixed $LiFePO_4$ cathode material synthesized by the ceramic granulation method, *Ceramics International*, **34** (2008) 1349.

[179] M.S. Wooldridge, Gas-phase combustion synthesis of particles, *Progress in Energy and Combustion Science*, **24** (1998) 63.

[180] A. Gutsch, H. Mühlenweg, M. Krämer, Tailor-Made Nanoparticles via Gas-Phase Synthesis, *Small*, **1** (2005) 30.

[181] R. Strobel, S.E. Pratsinis, Flame aerosol synthesis of smart nanostructured materials, *Journal of Materials Chemistry*, **17** (2007) 4743.

[182] F.O. Ernst, H.K. Kammler, A. Roessler, S.E. Pratsinis, W.J. Stark, J. Ufheil, P. Novák, Electrochemically active flame-made nanosized spinels: $LiMn_2O_4$, $Li_4Ti_5O_{12}$ and $LiFe_5O_8$, *Materials Chemistry and Physics*, **101** (2007) 372.

[183] N.A. Hamid, S. Wennig, S. Hardt, A. Heinzel, C. Schulz, H. Wiggers, High-capacity cathodes for lithium-ion batteries from nanostructured $LiFePO_4$ synthesized by highly-flexible and scalable flame spray pyrolysis, *Journal of Power Sources*, **216** (2012) 76.

[184] Y. Wang, J. Wang, J. Yang, Y. Nuli, High-Rate LiFePO4 Electrode Material Synthesized by a Novel Route from $FePO_4 \cdot 4H_2O$, *Advanced Functional Materials*, **16** (2006) 2135.

[185] S.S. Zhang, J.L. Allen, K. Xu, T.R. Jow, Optimization of reaction condition for solid-state synthesis of $LiFePO_4$-C composite cathodes, *Journal of Power Sources*, **147** (2005) 234.

[186] S. Brunauer, P.H. Emmett, E. Teller, Adsorption of Gases in Multimolecular Layers, *Journal of the American Chemical Society*, **60** (1938) 309.

[187] B.E. Warren, X-Ray Diffraction, Dover Publications Inc., New York, 1969.

[188] S.M. L. Lutterotti, H. R. Wenk, in: ICUr: Newsletter of the CPD, 1999, pp. 14.

[189] B. Fultz, J. Howe, Transmission Electron Microscopy and Diffractometry of Materials, Third Edition ed., Springer-Verlag, 2008.

[190] Y. Leng, Materials characterization: Introduction to Microscopic and Spectroscopic Methods, John Wiley & Sons (Asia) Pte. Ltd, Singapore, 2008.

[191] H. Ishida, Materials characterization series, Momentum Press, New York, 2010.

[192] D.P.E. Dickson, F.J. Berry, Mössbauer Spectroscopy, Cambridge University Press, New York, 1986.

[193] J. Heinze, Cyclic Voltammetry—"Electrochemical Spectroscopy". New Analytical Methods (25), *Angewandte Chemie International Edition in English*, **23** (1984) 831.

[194] A. Vu, A. Stein, Multiconstituent Synthesis of $LiFePO_4$/C Composites with Hierarchical Porosity as Cathode Materials for Lithium Ion Batteries, *Chemistry of Materials*, **23** (2011) 3237.

[195] A. Liu, Z. Hu, Z. Wen, L. Lei, J. An, $LiFePO_4$/C with high capacity synthesized by carbothermal reduction method, *Ionics*, **16** (2010) 311.

[196] H. Liu, J. Xie, K. Wang, Synthesis and characterization of nano-$LiFePO_4$/carbon composite cathodes from 2-methoxyethanol-water system, *Journal of Alloys and Compounds*, **459** (2008) 521.

[197] C.H. Mi, X.B. Zhao, G.S. Cao, J.P. Tu In Situ Synthesis and Properties of Carbon-Coated $LiFePO_4$ as Li-Ion Battery Cathodes, *Journal of The Electrochemical Society*, **152** (2005) A483.

[198] L. Yu, Q. Liu, H. Wang, Synthesis of $LiFePO_4$-C cathode materials using a green and low-cost method, *Ionics*, **15** (2009) 689.

[199] Z. Xu, L. Xu, Q. Lai, X. Ji, Microemulsion synthesis of $LiFePO_4$/C and its electrochemical properties as cathode materials for lithium-ion cells, *Materials Chemistry and Physics*, **105** (2007) 80.

[200] K. Galoustov, M. Anthonisen, D.H. Ryan, D.D. MacNeil, Characterization of two lithiation reactions starting with an amorphous $FePO_4$ precursor, *Journal of Power Sources*, **196** (2011) 6893.

[201] S. Okada, T. Yamamoto, Y. Okazaki, J.-i. Yamaki, M. Tokunaga, T. Nishida, Cathode properties of amorphous and crystalline $FePO_4$, *Journal of Power Sources*, **146** (2005) 570.

[202] P. Reale, B. Scrosati, C. Delacourt, C. Wurm, M. Morcrette, C. Masquelier, Synthesis and Thermal Behavior of Crystalline Hydrated Iron(III) Phosphates of Interest as Positive Electrodes in Li Batteries, *Chemistry of Materials*, **15** (2003) 5051.

[203] Y. Wang, B. Sun, J. Park, W.-S. Kim, H.-S. Kim, G. Wang, Morphology control and electrochemical properties of nanosize $LiFePO_4$ cathode material synthesized by co-precipitation combined with in situ polymerization, *Journal of Alloys and Compounds*, **509** (2011) 1040.

[204] X. Zhi, G. Liang, L. Wang, X. Ou, L. Gao, X. Jie, Optimization of carbon coatings on $LiFePO_4$: Carbonization temperature and carbon content, *Journal of Alloys and Compounds*, **503** (2010) 370.

[205] K. Yang, Z. Lin, X. Hu, Z. Deng, J. Suo, Preparation and electrochemical properties of a $LiFePO_4$/C composite cathode material by a polymer-pyrolysis-reduction method, *Electrochimica Acta*.

[206] A.C. Ferrari, J. Robertson, Interpretation of Raman spectra of disordered and amorphous carbon, *Physical Review B*, **61** (2000) 14095.

[207] R. Dedryvère, M. Maccario, L. Croguennec, F. Le Cras, C. Delmas, D. Gonbeau, X-Ray Photoelectron Spectroscopy Investigations of Carbon-Coated LixFePO4 Materials, *Chemistry of Materials*, **20** (2008) 7164.

[208] S.-H. Wu, K.-M. Hsiao, W.-R. Liu, The preparation and characterization of olivine $LiFePO_4$ by a solution method, *Journal of Power Sources*, **146** (2005) 550.

[209] J. Liu, G. Yang, X. Zhang, J. Wang, R. Wang, Synthesis of the $LiFePO_4$/C core–shell nanocomposite using a nano-$FePO_4$/polythiophene as an iron source, *Journal of Power Sources*, **197** (2012) 253.

[210] N. Kalaiselvi, A. Manthiram, One-pot, glycine-assisted combustion synthesis and characterization of nanoporous $LiFePO_4$/C composite cathodes for lithium-ion batteries, *Journal of Power Sources*, **195** (2010) 2894.

[211] V. Drozd, G.Q. Liu, R.S. Liu, H.T. Kuo, C.H. Shen, D.S. Shy, X.K. Xing, Synthesis, electrochemical properties, and characterization of $LiFePO_4$/C composite by a two-source method, *Journal of Alloys and Compounds*, **487** (2009) 58.

[212] Y. Xu, Y. Lu, L. Yan, Z. Yang, R. Yang, Synthesis and effect of forming Fe2P phase on the physics and electrochemical properties of $LiFePO_4$/C materials, *Journal of Power Sources*, **160** (2006) 570.

[213] Y.-H. Rho, L.F. Nazar, L. Perry, D. Ryan, Surface Chemistry of $LiFePO_4$ Studied by Mössbauer and X-Ray Photoelectron Spectroscopy and Its Effect on Electrochemical Properties, *Journal of The Electrochemical Society*, **154** (2007) A283.

[214] A.S. Andersson, J.O. Thomas, B. Kalska, L. Häggström, Thermal Stability of $LiFePO_4$ - Based Cathodes, *Electrochemical and Solid-State Letters*, **3** (2000) 66.

[215] A.A.M. Prince, S. Mylswamy, T.S. Chan, R.S. Liu, B. Hannoyer, M. Jean, C.H. Shen, S.M. Huang, J.F. Lee, G.X. Wang, Investigation of Fe valence in $LiFePO_4$ by Mössbauer and XANES spectroscopic techniques, *Solid State Communications*, **132** (2004) 455.

[216] Z.H. Chen, J.R. Dahn, Reducing carbon in $LiFePO_4$/C composite electrodes to maximize specific energy, volumetric energy, and tap density, *Journal of the Electrochemical Society*, **149** (2002) A1184.

[217] T. Nakamura, Y. Shima, H. Matsui, Y. Yamada, S. Hashimoto, H. Miyauchi, N. Koshiba, Synthesis of $LiFePO_4$ / C Composite Particles by Gas–Solid Phase Reaction and Their Electrochemical Properties, *Journal of The Electrochemical Society*, **157** (2010) A544.

[218] G. Kobayashi, A. Yamada, S.-i. Nishimura, R. Kanno, Y. Kobayashi, S. Seki, Y. Ohno, H. Miyashiro, Shift of redox potential and kinetics in $Li_x(Mn_yFe_{1-y})PO_4$, *Journal of Power Sources*, **189** (2009) 397.

[219] X.-Y. Chang, Z.-X. Wang, X.-H. Li, L. Zhang, H.-J. Guo, W.-J. Peng, Synthesis and performance of $LiMn_{0.7}Fe_{0.3}PO_4$ cathode material for lithium ion batteries, *Materials Research Bulletin*, **40** (2005) 1513.

[220] J.M. Osorio-Guillén, B. Holm, R. Ahuja, B. Johansson, A theoretical study of olivine $LiMPO_4$ cathodes, *Solid State Ionics*, **167** (2004) 221.

[221] H.W.N.a.D. BanerJee, Interpretation of XPS Mn(2p) spectra of Mn oxyhydroxides and constraints on the mechanism of MnO_2 precipitation, *American Mineralogist*, **83** (1998) 305.

[222] C. Li, N. Hua, C. Wang, X. Kang, W. Tuerdi, Y. Han, Effect of Mn^{2+}-doping in $LiFePO_4$ and the low temperature electrochemical performances, *Journal of Alloys and Compounds*, **509** (2011) 1897.

7 Publications and presentations list

7.1 Publications

1. N.A. Hamid, S. Wennig, S. Hardt, A. Heinzel, C. Schulz, H. Wiggers," High-Capacity Cathodes for Lithium-Ion Batteries from Nanostructured $LiFePO_4$ Synthesized by Highly-Flexible and Scalable Flame Spray Pyrolysis", *Journal of Power Sources,* **216** (2012) 76-83. Win best paper award 2012 by Centre for NanoIntegration Duisburg-Essen (CENIDE).

2. N.A. Hamid, S. Wennig, A. Heinzel, C. Schulz, H. Wiggers," Synthesis and characterization of Nanocomposite $LiFePO_4$/C for Lithium-Ion Batteries", *Journal of Power Sources, to be submitted*

7.2 Presentations

1. High Surface Area $LiFePO_4$/Carbon Composite Materials for Lithium Ion Batteries using Gas Phase Flame Synthesis, *International Conference of Materials Advanced Technology* 2011 Singapore (oral presentation)

2. High Surface Area $LiFePO_4$/Carbon Composite Materials for Lithium Ion Batteries using Gas Phase Flame Synthesis, *International Research Universities Network* 2011 Nijmegen, Netherland (oral presentation)

3. Cathode materials for lithium ion batteries, *Institute for Combustion and Gasdynamics* 2011, Duisburg, Germany (oral presentation)

4. $LiFePO_4$ /Carbon Nanocomposites as High Performance Cathode Materials for Lithium Ion Batteries, *European Material Research Society* 2012, Warsaw, Poland (oral presentation)

5. Doping effects on the electrochemical behavior of $LiFePO_4$, *Material Science and Engineering* 2012, Darmstadt, Germany (oral presentation)

Curriculum Vitae

Der Lebenslauf ist in der Online-Version aus datenschutzrechtlichen Gründen nicht enthalten